

UCLA

UCLA Electronic Theses and Dissertations

Title

Observational constraints on dust size and shape: implications for global aerosol models and remote sensing retrievals

Permalink

<https://escholarship.org/uc/item/8q67c8pm>

Author

Huang, Yue

Publication Date

2021

Peer reviewed|Thesis/dissertation

UNIVERSITY OF CALIFORNIA
Los Angeles

Observational constraints on dust size and shape: implications for global aerosol models
and remote sensing retrievals

A dissertation submitted in partial satisfaction
of the requirements for the degree
Doctor of Philosophy in Atmospheric and Oceanic Sciences

by

Yue Huang

2021

© Copyright by
Yue Huang
2021

ABSTRACT OF THE DISSERTATION

Observational constraints on dust size and shape: implications for global aerosol models
and remote sensing retrievals

by

Yue Huang

Doctor of Philosophy in Atmospheric and Oceanic Sciences

University of California, Los Angeles, 2021

Professor Jasper F. Kok, Chair

Desert dust is the dominant aerosol type by mass in the atmosphere. Dust impacts on various aspects of the Earth system depend sensitively on its size and shape. However, global aerosol models and remote sensing retrievals struggle to correctly account for dust shape and size for a few reasons. These issues include that (i) models and retrieval algorithms lack a consistent and accurate quantification of dust shape, (ii) models and retrievals substantially underestimate the abundance of coarse dust in the atmosphere relative to measurements, (iii) measurements of size distributions are also problematic because they are based on different diameter types that do not account for realistic dust shapes, and (iv) measurements of emitted dust size distributions are not available for some major soil types (e.g., active sands), making the validation process for these regions difficult. The resulting biases in dust shape and size can propagate into dust optical properties used in models and retrieval algorithms, which further contributes to inaccurate estimates of dust effects on the Earth system.

This dissertation addresses the issues above. Specifically, I present the first (to my knowledge) *in situ* field measurements of the size distributions of dust aerosols emitted from active sands. I show that active sands emit substantially finer dust than non-sandy soils. Second, I compile dozens of *in situ* observations of dust shape across the globe and obtain a globally representative constraint on the probability distributions describing dust shape. I show that

models and retrieval algorithms substantially underestimate dust asphericity by a factor of ~ 3 to 5; as aspherical dust deposits less quickly from the atmosphere, this underestimated dust asphericity causes models to underestimate dust lifetime by $\sim 20\%$. Third, I use this shape constraint to correct a compilation of measurements of emitted dust size distributions that neglected this substantial dust asphericity. I find that accounting for asphericity yields a substantially coarser emitted dust size distribution and that, consequently, current parameterizations underestimate coarse dust emission by more than a factor of ~ 2 . Finally, I account for the observational constraints on dust shape and size in obtaining the single-scattering properties of dust aerosols. This newly-developed dataset is extensively resolved by a wide range of wavelength, dust size, and dust refractive index values, which enables wide applications on models and remote sensing products.

These findings have several key implications. First, active sands emit substantially finer dust, which could enhance its downwind impacts on human health, the hydrological cycle, and regional climate. Second, the findings that models and retrieval algorithms underestimate both dust asphericity and coarse dust emission help explain why models underestimate the abundance of coarse dust in the atmosphere. Third, the results highlight the importance of standardized diameter conversions. A lack of such standardization can generate substantial biases, for instance in the measurements of dust size distributions. Finally, the extensive single-scattering properties accounting for realistic dust shape and size are being implemented into several global aerosol models, including MONARCH, IMPACT, NCAR CESM, and NASA GISS ModelE. This work could ultimately help narrow the large uncertainties in dust impacts on the Earth system.

The dissertation of Yue Huang is approved.

Marcelo Chamecki

Pablo E. Saide

Gregory S. Okin

Jasper F. Kok, Committee Chair

University of California, Los Angeles

2021

To my dad

*The weather maps in his office ignited my very first
interest in meteorology*

To my mom

*The optimistic characteristics that I inherited from her
accompany all my ups and downs*

TABLE OF CONTENTS

1	Overview	1
2	Fine dust emissions from active sands at coastal Oceano Dunes, California	5
2.1	Introduction	6
2.2	Methods	8
2.3	Results	15
2.4	Discussions	17
2.4.1	Insights into processes producing dust from active sands at the Oceano Dunes State Vehicular Recreation Area	18
2.4.2	Insights into the representativeness of Oceano dust emissions for other active sands	21
2.4.3	Implications of dust emissions from the Oceano Dunes State Vehicular Recreation Area for downwind human health, park management, the hydrological cycle, and climate	23
2.4.4	Limitations of the methodology	25
2.5	Conclusions	26
2.6	Tables and figures	28
3	Climate models and remote sensing retrievals neglect substantial desert dust asphericity	38
3.1	Introduction	39
3.2	The shape descriptors of aspherical dust	40
3.2.1	Measurements of the aspect ratio and the height-to-width ratio	41

3.2.2	Addressing the systematic difference in particle width	42
3.3	Measurement compilation of dust shape descriptors	43
3.4	Lifetime enhancement due to dust asphericity	46
3.5	Limitations of methodology	48
3.6	Conclusions	49
3.7	Tables and figures	51
4	Linking the different diameter types of aspherical desert dust indicates that models underestimate coarse dust emission	62
4.1	Introduction	63
4.2	Linking the four diameters of aspherical dust	65
4.2.1	Quantifying dust asphericity	65
4.2.2	Linking the optical and geometric diameters	66
4.2.3	Linking the projected area-equivalent and geometric diameters	70
4.2.4	Linking the geometric and aerodynamic diameters	71
4.3	Harmonizing size distributions of emitted dust	72
4.4	Conclusions	76
4.5	Tables and figures	77
5	Single-scattering properties of ellipsoidal dust accounting for realistic shape distribution	84
5.1	Introduction	85
5.2	Methods	87
5.2.1	Dust shape and shape distribution	88
5.2.2	Single-scattering properties of ellipsoidal dust	89

5.3	Single-scattering properties in aerosol models	93
5.4	Single-scattering properties in remote sensing retrievals	96
5.4.1	Evaluating the scattering matrix	96
5.4.2	Evaluating the linear depolarization ratio and the lidar ratio	99
5.5	Discussions and Conclusions	102
5.6	Tables and figures	105
6	Final conclusions and future work	119
6.1	Final conclusions	119
6.2	Future work	122

LIST OF FIGURES

2.1	The experimental setup at Oceano Dunes. Instrumentation includes six sonic anemometers (S1–S6), nine Wenglor particle counters (W1–W9), eight Big Spring Number Eight sand samplers (A1–A4, B1–B4), four optical particle counters (D1–D4), and a weather station with temperature and humidity sensors (WS) (following <i>Martin and Kok (2017)</i>).	30
2.2	The vertical dust mass flux as a function of shear velocity within (a) the $PM_{10,g}$ geometric diameter range and (b) the $PM_{2.5,a}$ aerodynamic diameter range. Each of the two plots includes measurements at Oceano (black open circles) and previously published field studies of natural dust emissions from non-sandy soils (open triangles). These latter measurements were compiled in <i>Kok et al. (2014a)</i> , which corrected these measurements to the $PM_{10,g}$ geometric diameter range following the procedure described in that work. Furthermore, we corrected these measurements to the $PM_{2.5,a}$ aerodynamic diameter range assuming that their PSDs follow the prediction of the brittle fragmentation theory generated by aggregate fragmentation (<i>Kok, 2011a</i>). Error bars on the Oceano measurements were obtained through error propagation.	31

2.3	<p>Normalized volume particle size distribution (PSD) of dust at emission as a function of the dust aerosol geometric diameter averaged over all measurements at Oceano (black open circles). Plotted for comparison are measurements compiled by <i>Kok et al.</i> (2017) of (a) the emitted dust PSDs from non-sandy soils in the US (<i>Gillette et al.</i>, 1972, 1974; <i>Gillette</i>, 1974), China (<i>Fratini et al.</i>, 2007), North Africa (<i>Sow et al.</i>, 2009; <i>Rosenberg et al.</i>, 2014), and Australia (<i>Shao et al.</i>, 2011a) and (b) in situ aircraft measurements of dust-dominated PSDs close to the Saharan source regions. Note that these measurements are normalized using the procedure described in <i>Kok</i> (2011a) and <i>Kok et al.</i> (2017), which differs somewhat from the procedure used for the Oceano data (see Sect. 2.2). Also plotted for comparison is the brittle fragmentation theory (dashed–dotted blue lines) on the PSD of emitted dust generated by aggregate fragmentation (<i>Kok</i>, 2011a). Error bars on the Oceano measurements were obtained through error propagation.</p>	32
2.4	<p>Shear velocity dependence of the normalized volume particle size distribution of dust at emission at Oceano. We divided the measurements evenly into three shear velocity bins, with averaged values of 0.33, 0.37, and 0.41 ms^{-1}, respectively. Error bars on the measurements were obtained through error propagation.</p>	33

2.5	<p>The bulk sandblasting efficiency α (m^{-1}) at Oceano as a function of shear velocity. The linear-least-squares fit (black line) indicates that α increases as a power law in shear velocity with an exponent of 3.50 ± 0.89. Error bars were obtained by propagating errors from the sensor inter-calibration process, the regression used in the gradient method, and the subtraction of the sea-salt deposition flux. The two dotted black lines denote the 95% confidence range on the fit. The geometric and the aerodynamic diameter ranges of the vertical dust mass flux F_d are noted at the top, and Q is the total horizontal sand flux integrated over all sand grain sizes (<i>Martin et al., 2018</i>).</p>	34
2.6	<p>The sandblasting efficiency α_i (m^{-1}) of the six size bins at Oceano as a function of shear velocity. The linear-least-squares fit (black line) indicates that α_i varies as a power law in shear velocity with an exponent of 4.71 ± 0.97, 5.00 ± 1.37, 5.22 ± 1.63, 6.12 ± 2.11, 3.26 ± 1.90, and -2.89 ± 1.94 for the six respective size bins. The two dotted black lines denote the 95% confidence range of the fit. The geometric and aerodynamic diameter ranges of the vertical dust mass flux $F_{d,i}$ are noted at the top of each plot, and Q is the total horizontal sand flux integrated over all sand grain sizes (<i>Martin et al., 2018</i>).</p>	35
2.7	<p>Normalized volume particle size distribution (PSD) of sand samples collected from the Oceano field site. Statistical parameters of the PSD are reported in the table to the right. D10, D50, and D90 refer to cut-off diameters of the 10th, 50th, and 90th percentiles of sample grains by mass, respectively. Note that the values are averages of four samples with two collected from the tower location and two from 100 m upwind.</p>	36

2.8 (a) Scanning electron microscopy (SEM) image of an Oceano sand sample. (b) Energy dispersive X-ray spectroscopy (EDS) chemical composition (percentage by mass) of a quartz grain in (a) (the location of the analysis is marked by the black letter “B”). (c) EDS chemical composition of a K-rich feldspar in (a) marked by the black letter “C”. (d) Close-up image of a quartz sand grain with mineral coatings. (e) EDS chemical composition of the mineral coatings in (d) marked by the black letter “E”. 37

3.1 **(a) Top view of two-dimensional (2-D) projected area (within the black line) of a dust particle and (b) side view, along the length L (blue line) defined in (a), of the same particle collected on a plane surface by impactors.** Panel (a) demonstrates the systematic difference in the two common quantifications of dust width. The first definition records the maximum distance between two points on the outline that is perpendicular to the length L as the width W_{perp} (green line). The second definition records the width $W_{ellipse}$ (red dashed line) as the minor axis of an area-equivalent ellipse (blue dashed line) with L as its major axis. Because W_{perp} is systematically larger than $W_{ellipse}$ (Table 3.1), this systematic difference causes a systematic bias between experimental studies using different definitions of particle width. Panel (b) demonstrates the definition of dust height. The height H (orange line) is defined as the maximum distance between the outline of the particle to the collection surface that is perpendicular to the collection surface. . . . 55

3.2	<p>Measurement compilation of the medians of (a) the aspect ratio, (c) the height-to-width ratio, and (e) the length-to-height ratio as a function of projected area-equivalent diameter. The horizontal bars in (a), (c), and (e) show the bin ranges of the measurements, and the markers are plotted on the geometric means of the size ranges. The vertical bars in (a) and (c) denote errors from the uncertainty of the correction factor, and the vertical bars in (e) denote errors that propagate from (a) and (c). In the legend, the numbers in parentheses denote the numbers of analyzed individual dust particles. <i>Chou et al. (2008)</i> and <i>Woodward et al. (2015)</i> have two numbers with the first one denoting the number of analyzed dust particles for AR and the second one for HWR.</p>	56
3.3	<p>Changes during transport of the median aspect ratio of (a) North African dust and (c) Asian dust. The markers in (a) and (c) are defined in the legend of Figure 3.2. Results grouped by transport distance (see Figure 3.7) are shown in (b) and (d). In (d), median aspect ratios before ($\frac{L}{W_{perp}}$) and after ($\frac{L}{W_{ellipse}}$) the correction of the particle width are shown. This correction leads to a systematic change in all Asian dust studies and therefore does not affect the trend in shape during transport.</p>	57
3.4	<p>Probability distributions of (a) the reduction in gravitational settling velocity and (b) the enhancement of lifetime with respect to gravitational settling due to dust asphericity. Because deposition of dust with $D < 20\mu m$ occurs in the Stokes regime, the effect of asphericity on dust gravitational settling is independent of size.</p>	58

3.5	Three-dimensional view of a dust particle approximated as a (a) sphere, (b) prolate spheroid, (c) oblate spheroid, and (d) ellipsoid. In each plot, the three perpendicular axes are denoted. The largest, intermediate, and smallest axes are referred to as particle length L , width W , and height H , respectively. In shape (a) $L = W = H$, in shape (b) $L \geq W = H$, in shape (c) $L = W \geq H$, and in shape (d) $L \geq W \geq H$, such that shapes (a), (b) and (c) are simplified cases of shape (d).	59
3.6	The correction factor between the two common definitions of particle width (see Fig. 3.1), shown as a function of projected area-equivalent diameter for (A) 681 Asian dust particles, (B) 1261 Saharan dust particles, and (c) 1942 dust particles in total.	60
3.7	Locations of measurement sites for data used in this study. Measurements are grouped by source regions and transport distance, namely dust over Asian source regions and in short-range transport (in red markers), Asian long-range transported dust (in purple markers), dust over North African source regions (in blue markers), North African short-range transported dust (in green), and North African long-range transported dust (in orange markers). We determined whether dust was measured over Asian or North African source regions using the seasonally-resolved source regions obtained in <i>Ginoux et al.</i> (2012). We then distinguished long-range transported dust from short-range transported dust based on the attributions in publications that reported these measurements. The numbers in parentheses in the legend denote the number of analyzed individual dust particles. <i>Chou et al.</i> (2008) has two numbers with the first one denoting the number of analyzed dust particles for AR and the second one for HWR.	61

4.1	<p>Linking the four different diameter types of aspherical dust. Shown are (a) a schematic of four diameter types of an aspherical dust particle, and conversions between (b) the geometric and optical diameters, (c) the projected area-equivalent and geometric diameters, and (d) the aerodynamic and geometric diameters. Diameter conversions in (b-d) account for dust asphericity using the globally averaged shape distributions (Section 4.2.1). In (b), the optical particle counter (OPC) wavelength is taken as 780 nm, the scattering angle range is $90^\circ \pm 60^\circ$, and the real part of dust refractive index is 1.52. These results indicate that optical diameter underestimates geometric diameter at coarse sizes, that projected area-equivalent diameter overestimates geometric diameter by $56.3\% \pm 0.8\%$, and that aerodynamic diameter exceeds geometric diameter by $44.9\% \pm 0.3\%$ (standard errors are propagated from errors in globally averaged shape distributions).</p>	80
4.2	<p>Diagnosis of the factors causing optical particle counters (OPCs) to underestimate the size of coarse dust. Shown are (a) the sideward-scattered intensity SI, (b) the scattering efficiency Q_{sca}, and (c) the integrated phase function $IntP$, such that $SI \propto Q_{sca} \times IntP$. The scattering efficiency Q_{sca} is a product of (d) the extinction efficiency Q_{ext} and (e) the single-scattering albedo ω_0. The integrated phase function $IntP = \frac{1}{2} \int_{\theta_1}^{\theta_2} P(\theta) \sin(\theta) d\theta$ is the (f) phase function $P(\theta)$ integrated over the scattering angle range measured by OPCs (taken here as $90^\circ \pm 60^\circ$; range enveloped in black dotted lines in (f)).</p>	81

4.3 **Normalized size distributions of emitted dust (a) before and (b) after harmonizing the different diameter types.** Also shown are dust emission flux of individual size bins as percentages of (c) the size range within $0 \leq D_{geo} \leq 20\mu m$ ($PM_{20,geo}$) and (d) the size range within $0 \leq D_{aero} \leq 10\mu m$ ($PM_{10,aero}$). Vertical error bars in (a and b) denote the standard error of measurements under various wind events at a given soil. In (b), the blue dash-dotted line represents the maximum likelihood estimated (MLE) fit of brittle fragmentation theory (BFT; *Kok* (2011a)) to the 10 distinct data sets. Blue shading in (b) and vertical error bars in (c and d) denote 95% confidence interval. Compared to the MLE fit, the original BFT parameterization substantially underestimates the mass of emitted dust with $D_{geo} \geq 10\mu m$ 82

4.4 **Sensitivity tests of the diameter conversions to dust shape distributions.** Shown are diameter conversions between the geometric diameter and (a, b) the optical diameter, (c) the projected area-equivalent diameter, and (d) the aerodynamic diameter. Each panel contains diameter conversions under five different shape distributions representing different regions (their shape descriptors are given in Table 4.1). In panels (a) and (b), the wavelength is taken as 780 nm and the scattering angle range is $90^\circ \pm 60^\circ$, as for Fig. 4.1b in the main text. In panels (c) and (d), box plots present the statistics of the distribution of $\frac{D_{area}}{D_{geo}}$ and $\frac{D_{aero}}{D_{geo}}$, respectively. In each box plot, the central red line denotes the median, the black dot denotes the mean, the bottom and top edges of the blue box denote respectively the 25th- and 75th- percentiles, and the whiskers denote 95% confidence interval. These results indicate that regional differences in dust shape distributions produce only minor differences in diameter conversions. 83

- 5.1 **Single-scattering properties of spherical and ellipsoidal dust in the shortwave and longwave spectra.** Left column includes: (a) extinction efficiency, (b) mass extinction efficiency, (c) asymmetry factor, and (d) single-scattering albedo, at a wavelength of 550 nm. Right column includes these variables at 10 μm . The refractive index of dust aerosols is $1.53 \pm 0.03 - 10^{-2.75 \pm 0.25}i$ at 550 nm and $1.70 \pm 0.20 - 10^{-0.40 \pm 0.11}i$ at 10 μm . Values at geometric diameters of 0.2, 0.5, 1, 2, 5, 10, 20, and 50 μm are detailed in Table 5.2 at 550 nm and Table 5.3 at 10 μm 108
- 5.2 **Size distributions of the feldspar sample and two dust samples included in the Amsterdam-Granada Light Scattering Database (AGLSD).** The size distributions were measured using a laser particle sizer (model Mastersizer 2000) with water as dispersive medium (*Gómez Martín et al.*, 2021). The black dotted line denotes the upper limit (i.e., 67.8 μm in diameter) of dust size range in *Dubovik et al.* (2006)’s kernel, which is the most widely used database in remote sensing retrievals. In Section 5.4.1, we only use the size distributions at $D \leq 67.8 \mu\text{m}$ when using both *Dubovik et al.* (2006)’s kernel and the single-scattering database of ellipsoidal dust (*Meng et al.*, 2010) (see Section 5.2.2) for consistency. Among the three samples (i.e., feldspar, Gobi, and SaharaOSN), only feldspar is fully within the size range limit. 109

5.3 **A comparison between the cumulative probability distribution of dust length-to-height ratio used in the retrieval algorithms of AERONET and from a measurement compilation.** Both the retrieval algorithms (*Dubovik et al., 2006*) and the measurement compilation (*Huang et al., 2020*) (see Section 5.2.1) assume that dust shape is invariant with dust size. AERONET’s retrieval algorithms use this size-invariant cumulative probability distribution (red line with markers) by default for retrievals of dust properties. This default shape distribution is used not only in version 2 and version 3 retrieval algorithms of AERONET, but also in the new Deep Blue algorithm (*Hsu et al., 2019*) and a developing retrieval algorithm for lidar observations (*Tesche et al., 2019*). The cumulative probability distribution used in retrieval algorithms substantially underestimates dust asphericity relative to measurement of dust asphericity. 110

5.4	Comparisons between the six non-zero elements of the laboratory-measured scattering matrix of a sample of crushed feldspar rock with three types of simulations at two wavelengths (441.6 and 632.8 nm).	
	The three types of simulations include (1) “Ellipsoid optics” (red line) that combines AGLSD samples’ size distributions, <i>Meng et al.</i> (2010)’s database of ellipsoidal dust optics, and <i>Huang et al.</i> (2020)’s compiled log-normal distributions of AR and HWR; (2) “Spheroid optics” (blue line) that combines AGLSD samples’ size distributions, <i>Dubovik et al.</i> (2006)’s kernel of spheroidal dust optics, and <i>Dubovik et al.</i> (2006)’s averaged retrieved distribution of aspect ratio; and (3) ”Sphere optics” (green line) that combines AGLSD samples’ size distributions and spherical dust optics calculated by Lorenz-Mie theory. For all three types of simulations, the refractive index is taken as $1.53 \pm 0.03 - 10^{-2.75 \pm 0.25}i$ (same as Fig. 5.1 and Table 5.2) at both 441.6 and 632.8 nm. The shaded ranges denote uncertainties propagated from the refractive index.	111
5.5	Same as Fig. 5.4 but for dust sample Gobi.	112
5.6	Same as Figs. 5.4 and 5.5 but for dust sample SaharaOSN. Note that laboratory measurements of P_{33}/P_{11} , P_{34}/P_{11} , and P_{44}/P_{11} at the wavelength of 488 nm are not available due to sensor issues (see <i>Gómez Martín et al.</i> (2021)).	113
5.7	Error-quantity between the three types of simulations (ellipsoid, spheroid, and sphere optics) and the laboratory observations for sample feldspar at two wavelengths (441.6 and 632.8 nm). The error bars denote uncertainties propagated from the dust refractive index (see the caption of Fig. 5.4). Ellipsoid and spheroid optics show significantly improved agreement with observations than sphere optics. Ellipsoid optics show significantly improved agreement with observations than spheroid optics. . .	114

5.8	Same as Fig. 5.7 but for dust sample Gobi.	115
5.9	Same as Figs. 5.7 and 5.8 but for dust sample SaharaOSN. Note that laboratory measurements of P_{33}/P_{11} , P_{34}/P_{11} , and P_{44}/P_{11} at the wavelength of 488 nm are not available due to sensor issues (see <i>Gómez Martín et al.</i> (2021)).	116
5.10	Wavelength dependence of the linear depolarization ratio of dust aerosols. Shown are the results at 4 wavelengths where field and laboratory observations of the linear depolarization ratio were taken (i.e., 355, 532, 710, 1064 nm) and at the 4 wavelengths of AERONET retrievals (i.e., 440, 670, 870, 1020 nm). The data compilation is after Fig. 1 of <i>Tesche et al.</i> (2019). The measurement compilation shows that the linear depolarization ratio peaks at 0.3 around the wavelength of 600 nm. Spheroid optics used in AERONET and an independent study (<i>Wiegner et al.</i> , 2009) cannot reproduce the magnitude or the wavelength dependence of the linear depolarization ratio, whereas the ellipsoid optics can excellently reproduce that.	117
5.11	Wavelength dependence of the lidar ratio of dust aerosols. Shown are the results at four wavelengths where field observations of the lidar ratio were taken (i.e., 355, 532, 710, 1064 nm). The data compilation is taken after Fig. 4 of <i>Saito and Yang</i> (2021). The simulation "ellipsoid optics" combines the shape-resolved single-scattering properties of ellipsoidal dust (<i>Meng et al.</i> , 2010), the globally representative dust shape distributions (<i>Huang et al.</i> , 2020), and the globally representative size distribution of dust aerosols (<i>Adebisi and Kok</i> , 2020). Results show that the ellipsoid optics overestimate dust lidar ratio by a factor of ~ 2 to 3 at all four wavelengths.	118

LIST OF TABLES

2.1	The dust geometric and aerodynamic diameters of the seven bin boundaries. Determination of the geometric diameter ranges uses Lorenz–Mie theory such that they produce the same range of scattered light intensity as the seven manufacturer-provided polystyrene latex sphere (PSL) diameter sizes. The ranges in geometric diameters derive from the uncertainty in the dust refractive indices. We determined the aerodynamic diameter ranges by applying Eq. (2.6) to the geometric diameter ranges.	28
2.2	Averaged mineralogy of the Oceano Dunes sand samples in unit of percentage by mass, determined from X-ray powder diffraction (XRPD) analysis. Note that the values in the table are averages of mineralogy of four 1 g samples with two collected from the tower location and two from 100 m upwind. Each analyzed sample contains hundreds of grains.	29
3.1	The correction factor between the two common definitions of particle width of 15 dust particles.	51
3.2	List of measurements of the aspect ratio (AR) by individual particle analysis.	52
3.3	List of measurements of the height-to-width ratio (HWR) by individual particle analysis.	54
4.1	The median and the geometric standard deviation (GSD) of the two lognormally-distributed shape descriptors (the aspect ratio, AR, and the height-to-width ratio, HWR) of ellipsoidal dust for different regions. Values are taken after <i>Huang et al.</i> (2020), who compiled 25 datasets of AR and HWR across the world (6 for Asian dust, 16 for North African dust, and 3 for artificial dust).	78

4.2	Parameters of the five studies that used optical particle counters (OPCs) to measure the particle size distributions (PSDs) of emitted dust.	79
5.1	Dust shape approximations used in current global aerosol models. The 14 global aerosol models are used in the AeroCom phase III intercomparison project (Gliß et al., 2021). All of them approximate dust as spheres.	105
5.2	Comparisons between single-scattering properties of ellipsoidal dust (denoted as “ellipsoid”) and those of spherical dust (denoted as “sphere”) at the wavelength of 550 nm. The refractive index of dust aerosols is taken the same for both shape approximations as $1.53 \pm 0.03 - 10^{-2.75 \pm 0.25}i$, which covers the range of <i>Di Biagio et al. (2019)</i> . The values in parentheses denote the 95% confidence interval. The errors in single-scattering properties are propagated from errors in dust refractive index for spherical dust, and from errors in dust refractive index and the parameters of the log-normal distributions of the shape descriptors for ellipsoidal dust (see Section 5.2.1).	106
5.3	Comparisons between single-scattering properties of ellipsoidal dust (denoted as “ellipsoid”) and those of spherical dust (denoted as “sphere”) at the wavelength of 10 μm. The refractive index of dust aerosols is taken the same for both shape approximations as $1.70 \pm 0.20 - 10^{-0.40 \pm 0.11}i$, which covers the ranges of <i>Volz (1972, 1973)</i> ; <i>Hess et al. (1998)</i> ; <i>Di Biagio et al. (2017)</i> . The values in parentheses denote the 95% confidence interval. The errors in single-scattering properties are propagated from errors in dust refractive index for spherical dust, and from errors in dust refractive index and the parameters of the lognormal distributions of the shape descriptors for ellipsoidal dust (see Section 5.2.1).	107

ACKNOWLEDGMENTS

I am about to earn the highest degree one person can get! What a proud feeling. Although the path to a Ph.D. degree was not easy, I am lucky to have received support and help from countless people, including my family, advisor, colleagues, and friends.

My greatest thanks go to my family. My awesome parents have offered me everything they have from the moment I was born. My dad Yuchao Huang sets a role model for me as a passionate meteorologist. The beautiful weather maps in his office shaped the very first understanding of science in my mind. My mom Songhua Du passes down the key to sustainable happiness, the optimistic characteristics. Her joyful and cheerful personality influenced and shaped me into who I am today. My husband Matthew McKinney is a great listener, baker, and succulent grower. His accompany and the green friends light up my daily life during the pandemic.

My deepest gratitude goes to my amazing advisor, Professor Jasper F. Kok, for his tremendous support, guidance, encouragement, and countless discussions during my Ph.D. study. Over the past six years, I have learned so much from Jasper's mastery of details in academic writings, uncanny ability to see the connections between results, and passionate dedication to do and share good science. Indeed, Jasper sets an amazing role model for me as an outstanding scholar.

My sincere thanks also go to my doctoral committee members, Professors Marcelo Chamecki, Pablo E. Saide, Gregory S. Okin, and the late Kuo-Nan Liou, for their patient guidance, firm support, and constructive discussions. I am especially dedicated to Kuo-Nan Liou, who was a giant in the field of atmospheric optics and had offered great help and care to many Asian American scientists including me.

I also want to thank all my collaborators: Raleigh L. Martin, Adeyemi A. Adebisi, Jun Meng, Danny M. Leung, Alyson M. Fritzmann, Itzhak Kutra, Hezi Yizhaq, Nitzan Swet, Thomas E. Gill, Richard L. Reynolds, Livia S. Freire, Konrad Kandler, Hannakaisa

Lindqvist, Timo Nousiainen, Tetsu Sakai, Olli Jokinen, Akinori Ito, Carlos Pérez García-Pando, Martina Klose, Jeronimo Escribano, Paola Formenti, Claudia Di Biagio, Olga Muñoz, Shu-Hua Chen, Leo Zhuo Xuan Lin, Alana Doderer, Olga Kalashnikova, Michael J. Garay, Yingxiao Zhang, Yuheng Zhang, Ralph A. Kahn, Vincenzo Obiso, and Ron L. Miller. All these fantastic scientists have taught me that doing good research is such a joy.

My great thanks go to my friends, particularly my best friends, Ruru Ma and Jiayu Li, for our 12 year-long golden friendship. In addition: Cenlin He, Ken Zhao, Yi-Hung Kuo, Francis Turney, Weiming Ma, Pengfei Zhang, Donglai Ma, Katie Tuite, Huilin Huang, Junzhen Zhang, Jiaqi Shen, Clara Si, Jordyn Moscoso, Daniel Clements, Laura Thapa, Calvin Howes, Todd Emmenegger, Gavin Madakumbura, Zoe Pierrat, Zhaoxin Ban, Liyin He, and Yuan Wang all deserve credit. Furthermore, to Yidan Sun, Ning Wang, Xu Xie, and Yaqi Zhang for insightful discussions about dreams and careers.

Finally, I acknowledge Yu Gu, Bai Yang, and Feng Tian for their encouragement during my grad school application seven years ago. I still remember the life-changing email, saying that: [*I'd like to take this opportunity to encourage you to try your best to keep the fire in your heart on, for there could be too many things which can hurt it in the long way ahead of you. But as long as you work hard, and with a little bit good luck, you can do it! Les Brown said: It is better to aim high and miss than to aim low and hit. It's really true.*]. Without them, I would not have moved to UCLA and had such an incredible six-year journey.

Funding support for my graduate education was provided by the Future Investigators in NASA Earth and Space Science and Technology (FINESST) fellowship, the UCLA Atmospheric and Oceanic Sciences Departmental Fellowship, the Palevsky Fellowship, the Dorothy Radcliffe Dee Fellowship, and the UCLA Doctoral Student Travel Grant. Research costs were supported by the NSF AGS-1552519 (all chapters), NSF AGS-1358621 (Chapter 2), BSF-2014178 (Chapter 2), NASA 80NSSC19K1346 (Chapters 3, 4, and 5), NSF AGS-1856389 (Chapters 3, 4, and 5), and the Army Research Office under Cooperative Agreement Number W911NF-20-2-0150 (Chapters 4 and 5).

VITA

- 2017–2018 Ph.D. Candidate in Atmospheric Sciences, University of California Los Angeles, USA
- 2015–2017 M.S. in Atmospheric Sciences, University of California Los Angeles, USA
- 2011–2015 B.S. in Atmospheric Sciences, Sun Yat-Sen University, China

PUBLICATIONS

1. **Huang, Y.**, J. F. Kok, R. L. Martin, N. Swet, I. Katra, T. E. Gill, R. L. Reynolds, and L. S. Freire (2019), Fine dust emissions from active sands at coastal Oceano Dunes, California, *Atmospheric Chemistry and Physics*, 19(5), 2947-2964, <https://doi.org/10.5194/acp-19-2947-2019>.
2. **Huang, Y.**, J. F. Kok, K. Kandler, H. Lindqvist, T. Nousiainen, S. Tetsu, A. A. Adebiyi, and O. Jokinen (2020), Climate models and remote sensing retrievals neglect substantial desert dust asphericity, *Geophysical Research Letters*, 47(6), <https://doi.org/10.1029/2019GL086592>.
3. **Huang, Y.**, A. A. Adebiyi, P. Formenti, and J. F. Kok (2021), Linking the different diameter types of aspherical desert dust indicates that models underestimate coarse dust emission, *Geophysical Research Letters*, 48(6), <https://doi.org/10.1029/2020GL092054>.
4. Swet, N., J. F. Kok, **Y. Huang**, H. Yizhaq and I. Katra (2020), Low dust generation

potential from active sand grains by wind abrasion, *Journal of Geophysical Research - Earth Surface*, 125(7), <https://doi.org/10.1029/2020JF005545>.

5. Kok, J. F., Adebisi, A. A., Albani, S., Balkanski, Y., Checa-Garcia, R., Chin, M., Colarco, P. R., Hamilton, D. S., **Huang, Y.**, Ito, A., Klose, M., Li, L., Mahowald, N. M., Miller, R. L., Obiso, V., Pérez García-Pando, C., Rocha-Lima, A., and Wan, J. S. (2021), Contribution of the world's main dust source regions to the global cycle of desert dust, *Atmospheric Chemistry and Physics*, 21(10), 8169–8193, <https://doi.org/10.5194/acp-21-8169-2021>.

6. Kok, J. F., Adebisi, A. A., Albani, S., Balkanski, Y., Checa-Garcia, R., Chin, M., Colarco, P. R., Hamilton, D. S., **Huang, Y.**, Ito, A., Klose, M., Leung, D. M., Li, L., Mahowald, N. M., Miller, R. L., Obiso, V., Pérez García-Pando, C., Rocha-Lima, A., Wan, J. S., and Whicker, C. A. (2021), Improved representation of the global dust cycle using observational constraints on dust properties and abundance, *Atmospheric Chemistry and Physics*, 21(10), 8127–8167, <https://doi.org/10.5194/acp-21-8127-2021>.

7. Klose, M., Jorba, O., Gonçalves Ageitos, M., Escribano, J., Dawson, M. L., Obiso, V., Di Tomaso, E., Basart, S., Montané Pinto, G., Macchia, F., Ginoux, P., Guerschman, J., Prigent, C., **Huang, Y.**, Kok, J. F., Miller, R. L., and Pérez García-Pando, C. (2021), Mineral dust cycle in the Multiscale Online Nonhydrostatic Atmosphere Chemistry model (MONARCH) Version 2.0, *Geoscientific Model Development*, preprint, <https://doi.org/10.5194/gmd-2021-32>.

8. Ito, A., A. A. Adebisi, **Y. Huang**, and J. F. Kok (2021), Less atmospheric radiative heating due to aspherical dust with coarser size, *Atmospheric Chemistry and Physics*, preprint, <https://doi.org/10.5194/acp-2021-134>.

CHAPTER 1

Overview

Desert dust is the dominant aerosol type by mass in the atmosphere (*IPCC AR5*, 2013). Throughout the dust cycle (including dust emission, short- and long-range transport, and deposition; *Shao et al.* (2011b)), dust produces important effects on the Earth system. First, dust absorbs and scatters both shortwave and longwave radiations, thereby modulating the Earth’s energy budget directly (*Kok et al.*, 2017). Second, dust acts as nuclei for cloud droplets and ice crystals, thereby modifying cloud microphysical properties and affecting the energy budget indirectly (*DeMott et al.*, 2015). Third, dust carries key nutrients (i.e., iron and phosphorus), and its deposition to the downwind ocean and land boosts primary productivity and carbon sequestration (*Yu et al.*, 2015; *Ito et al.*, 2019). In this way, dust aerosols affect the carbon cycle and associated climate feedbacks. Furthermore, dust aerosols impact anthropogenic activities, including by depleting renewable energy generation (*Piedra and Moosmüller*, 2017), degrading regional air quality and visibility (*Mahowald et al.*, 2007), and producing hazards to human health (*Burnett et al.*, 2014).

These varied impacts above depend sensitively on dust microphysical properties, especially dust size and shape. The overall effect of the fine dust cools the Earth system by scattering shortwave radiation, whereas coarse dust net warms the system by also absorbing both shortwave and longwave radiation (*Kok et al.*, 2017). In addition, dust asphericity increases aerodynamic drag force at a given volume and mass, causing aspherical dust to have a longer lifetime in the atmosphere than volume-equivalent spherical dust (*Yang et al.*, 2013; *Huang et al.*, 2020). Aspherical dust also differs from volume-equivalent spherical dust in the angular and the wavelength dependencies of single-scattering properties (*Dubovik et al.*,

2006; *Nousiainen and Kandler, 2015*). As such, accurate knowledge of dust shape and size is key to, for instance, accurate estimates of dust deposition fluxes, spatial and temporal distributions, and direct radiative effects at both regional and global scales.

Although accurate quantifications of dust shape and size are thus important for calculating dust impacts, current representations of dust shape and size in global aerosol models and remote sensing retrievals conflict with in situ measurements. Specifically, models and retrieval algorithms lack a consistent quantification of dust shape (*Kalashnikova et al., 2005; Dubovik et al., 2006; Mahowald et al., 2014*); their quantifications are inaccurate relative to measurements of dust shape (*Huang et al., 2020*). In addition, models and retrieval algorithms substantially underestimate the abundance of coarse dust in the atmosphere relative to measurements (*Ryder et al., 2019; Adebisi and Kok, 2020*). During the validation process, measurements are treated as the "ground truth" in general; however, measurements of size distributions can be problematic because they are based on different diameter types that do not account for realistic dust shapes (*Huang et al., 2021*). Furthermore, measurements of emitted dust size distributions are not available for some major soil types (e.g., active sands), making the validation process for these regions difficult. The resulting biases in dust shape and size can propagate into dust optical properties used in models and retrieval algorithms, which further contributes to inaccurate estimates of dust effects on the Earth system. In this dissertation, I address the above issues in the following chapters.

In Chapter 2, I present the first (to my knowledge) in situ field measurements of the size distributions of emitted dust from active sands, which cover 20% of arid lands worldwide (*Huang et al., 2019*). I conducted field measurements of dust emission under natural aeolian saltation from coastal Oceano Dunes in California as well as laboratory analyses on the topsoil sand samples. I found that dust emission from active sands differs from dust emission from non-sandy soils not only in the size distribution of emitted dust, but also in the magnitude of dust emission flux, the magnitude and the shear velocity dependence of the sandblasting efficiency, and the mineralogical composition of the emitted dust. This work improves the

understanding on the physical processes that drive dust emission from active sands, and suggests important implications of dust emission from active sands for downwind human health, park management, the hydrological cycle, and climate.

In Chapter 3, I present a globally representative parameterization of dust shape from a measurement compilation (*Huang et al.*, 2020). I compiled dozens of measurements of dust shape descriptors across the globe. I found that at the regional scale, North African dust becomes more aspherical during transport, whereas Asian dust might become less aspherical. At the global scale, the longest dimension (dust length) is on average five times larger than the smallest dimension (dust height), and current climate models and remote sensing retrievals underestimate this dust asphericity (i.e., dust length divided by its height) by a factor of $\sim 3 - 5$. Accounting for realistic dust asphericity increases gravitational settling lifetime by $\sim 20\%$, which helps explain the underestimation of coarse dust transport by models. This work points out the direction for future improvements with regard to dust shape in global aerosol models and the retrieval algorithms of remote sensing products.

In Chapter 4, I harmonize the measurements of dust size distributions that are based on four different types of diameters (including the geometric, aerodynamic, optical, and projected area-equivalent diameters) (*Huang et al.*, 2021). I obtained conversions between these different diameter types that account for dust asphericity. Even for the same dust particle, these diameter types are highly different from each other, suggesting the importance of diameter standardization in the dust research community. I then used these diameter conversions to obtain a consistent observational constraint on the size distribution of emitted dust. This observational constraint is substantially coarser than parameterizations used in global aerosol models, which underestimate the mass of emitted dust with a diameter in between 10 to 20 μm by a factor of ~ 2 and usually do not account for the substantial dust emissions larger than 20 μm in diameter. This work suggests that models substantially underestimate coarse dust emission, which helps explain the underestimation of coarse dust transport by models (*Adebiji and Kok*, 2020).

In Chapter 5, I for the first time account for a realistic dust shape distribution in obtaining single-scattering properties of dust aerosols. I found that neglecting the asphericity of dust and approximating dust as spherical particles underestimates the extinction efficiency, the mass extinction efficiency, the asymmetry factor, and the single-scattering albedo for all dust sizes at both shortwave and longwave spectra, since global aerosol models approximate dust as spheres. In addition, I found that the inaccurate quantification of dust shape in retrieval algorithms causes them to generate an incorrect magnitude and wavelength dependence of the linear depolarization ratio relative to observations. The newly-developed ellipsoidal dust optics accounting for realistic shape distributions produce an excellent agreement with the measured linear depolarization ratio. Although the new ellipsoidal dust optics show potential to improve models and retrievals, it underestimates the magnitude of the backscattering intensity relative to laboratory and field observations. This finding indicates that a realistic quantification of dust body shape is not sufficient and that an accurate quantification of dust surface texture is also critical to accurately reproduce dust optical properties at backscattering angles.

CHAPTER 2

Fine dust emissions from active sands at coastal Oceano Dunes, California

[**Huang, Y.**, J. F. Kok, R. L. Martin, N. Swet, I. Katra, T. E. Gill, R. L. Reynolds, and L. S. Freire (2019), Fine dust emissions from active sands at coastal Oceano Dunes, California, *Atmospheric Chemistry and Physics*, 19(5), 2947-2964, <https://doi.org/10.5194/acp-19-2947-2019>.]

Abstract

Sand dunes and other active sands generally have a low content of fine grains and, therefore, are not considered to be major dust sources in current climate models. However, recent remote sensing studies have indicated that a surprisingly large fraction of dust storms are generated from regions covered by sand dunes, leading these studies to propose that sand dunes might be globally relevant sources of dust. To help understand dust emissions from sand dunes and other active sands, we present in situ field measurements of dust emission under natural saltation from a coastal sand sheet at Oceano Dunes in California. We find that saltation drives dust emissions from this setting that are on the low end of the range in emissions produced by non-sandy soils for similar wind speed. Laboratory analyses of sand samples suggest that these emissions are produced by aeolian abrasion of feldspars and

removal of clay-mineral coatings on sand grain surfaces. We further find that this emitted dust is substantially finer than dust emitted from non-sandy soils, which could enhance its downwind impacts on human health, the hydrological cycle, and climate.

2.1 Introduction

Dust emission by wind-blown (aeolian) processes produces important effects on the Earth system, including modulating the radiation budget (*Miller et al.*, 2006; *Kok et al.*, 2017), modifying cloud microphysics (*DeMott et al.*, 2015) and the hydrological cycle (*Ramanathan et al.*, 2001; *Miller et al.*, 2004), and producing risks to human health (*Burnett et al.*, 2014). Despite these critical impacts, simulations of dust emissions in current climate models have large uncertainties, particularly in predicted rates and spatial patterns of dust emissions (*Engelstaedter et al.*, 2006; *Huneus et al.*, 2011; *Kok et al.*, 2014b; *Evan et al.*, 2015). These uncertainties arise in part from a lack of understanding (i) of the physics of the emission process and (ii) of the dust emission productivity of different soil types.

Most parameterizations of dust emissions account only for emission through soil aggregate fragmentation, which dominates for non-sandy soils (defined as containing >10% by mass of clay- and silt-sized soil fines; *McKee* (1979)), and these parameterizations do not account for dust emission through removal of clay-mineral coatings or aeolian abrasion, which might dominate emissions from sandy soils (*Shao et al.*, 1993; *Alfaro and Gomes*, 2001; *Ginoux et al.*, 2001; *Zender et al.*, 2003; *Kok et al.*, 2014a). For both soil types, dust emission is facilitated by aeolian saltation (the ballistic motion of sand particles) and sandblasting (saltator-driven release of dust) (*Shao*, 2008). Sandblasting can emit dust in four primary ways:

1. fragmentation of aggregates of clay-sized ($< 2 \mu\text{m}$ in diameter) and silt-sized (2-63 μm in diameter) fine particles in the soil (*Kok*, 2011a);
2. release of single fine particles trapped between the sand particles (also referred to as

“resident fines”) (*Bullard et al.*, 2004);

3. rupturing of clay and oxide coatings attached to the surfaces of sand grains (*Bullard et al.*, 2004, 2007); and

4. chipping or spalling of sand grains, for instance of sharp corners, which is also known as aeolian abrasion (*Kuenen*, 1960; *Whalley et al.*, 1987; *Jerolmack and Brzinski*, 2010; *Sweeney et al.*, 2016).

The relative importance of the four physical processes depends largely on soil texture and composition: soil aggregate breakage is likely most important for soils with a large fraction of fine (clay- and silt-sized) grains (*Shao*, 2008; *Kok et al.*, 2012; *Swet and Kutra*, 2016), whereas removal of mineral coatings and aeolian abrasion might be more important for sandy soils (*Kuenen*, 1960; *Bullard et al.*, 2004, 2007; *Jerolmack et al.*, 2011; *Crouvi et al.*, 2012). Many dust models use preferential source functions to identify emissions in regions with a large content of fine grains held in soil aggregates, which are implicitly used as a proxy for dust emissions through aggregate fragmentation (*Ginoux et al.*, 2001; *Tegen et al.*, 2002; *Zender et al.*, 2003). As a consequence, dust models weigh emissions heavily towards non-sandy soils, and sandy soils are not treated as important dust sources in most current models (*Shao et al.*, 1993; *Ginoux et al.*, 2001; *Tegen et al.*, 2002; *Zender et al.*, 2003; *Ito and Kok*, 2017).

Although current models do not treat active sands (i.e., sands with active saltation transport; *Swet et al.* (2019)) as major dust sources, recent remote sensing observations found a higher correlation between dust emission events and wind strength over dune-covered surfaces than over many other geomorphic units of the Sahara Desert, the Chihuahuan Desert, the Lake Eyre basin, and the Taklamakan Desert (*Baddock et al.*, 2011; *Bullard et al.*, 2011; *Crouvi et al.*, 2012). Specifically, *Crouvi et al.* (2012) found that more than 40% of Saharan dust storms originated from sand dunes and that sand dunes had a higher land erodibility (regression of number of dust storms against surface wind) than other soil types. Based on these observations, *Crouvi et al.* (2012) proposed aeolian abrasion on active sand

dunes as an important dust emission mechanism. Although remote sensing observations are informative for regional dust emission patterns (*Prospero et al.*, 2002; *Crouvi et al.*, 2012), uncertainties in backtracking satellite images to locate exact dust sources, combined with the lack of information on dust concentration or composition, small-scale land–surface dynamics, and magnitude of wind stress (*Bullard et al.*, 2011), impede the resolution of the productivity of active sands.

Considering these limitations of satellite observations, field measurements of dust emission from active sands are needed to inform whether active sands are indeed important contributors to the global dust cycle and, if so, what the physics of the emission process and the dust emission productivity of active sands are. Unfortunately, there are few measurements of dust emissions from active sands, especially under natural field conditions (*Bullard et al.*, 2004; *Sweeney et al.*, 2016; *Swet et al.*, 2019). To improve our understanding of dust emission from active sands, we present the first (to our knowledge) in situ field measurements of dust emission under natural aeolian saltation from active sands at the coastal Oceano Dunes in California. Sect. 2.2 details the field campaign setup, in situ data processing methods, and laboratory techniques used to analyze sand samples. Section Sect. 2.3 presents results of the vertical dust mass flux, the particle size distribution of emitted dust, the size-resolved sand-blasting efficiencies, and the properties of sand samples. Section 2.4 discusses dust emission processes at the study site and their representativeness for dust emissions from other active sands, as well as the implications of our results for downwind human health, the hydrological cycle, and climate. Conclusions follow in Sect. 2.5.

2.2 Methods

We conducted a field campaign from 15 May to 7 June 2015 on the southern edge of the Oceano Dunes State Vehicular Recreation Area (35.03°N, 120.63°W) where off-highway motor vehicles were prohibited (Oceano Dunes State Vehicular Recreation Area, SVRA, map:

http://ohv.parks.ca.gov/?page_id=1208, last access: 27 February 2019). At the time of measurements, the site was not downwind of any vehicle activity and was completely non-vegetated and topographically mostly flat. This active coastal sand sheet is followed inland by low transverse dunes. These dunes are part of the broader late Quaternary Guadalupe-Nipomo Dunes Complex, which extends north–south along roughly 25 km of California’s Central Coast and is shaped by strong onshore (westerly) sea breezes transporting sand primarily derived from fluvial deposits of the Santa Maria River estuary at the south end of the dune field (*Cooper*, 1967; *Orme*, 1992; *Pye and Tsoar*, 2009). Currently, active aeolian transport occurs only within 1-2 km of the beach, but inactive, vegetation-stabilized transverse dune surfaces extend up to 18 km inland.

We erected a 10 m tower (Fig. 2.1) at a distance of ~ 650 m from the shoreline to measure wind speed and direction, sand flux, and dust concentration from 15 May to 4 June 2015. We mounted six Campbell Scientific CSAT3 sonic anemometers (*Liu et al.*, 2001) on the tower, of which we used the three-dimensional winds measured by the lowest sonic anemometer (about 0.5 m above the surface) to determine shear stress and shear velocity (details in *Martin and Kok* (2017)). In addition, we obtained the vertical profile of horizontal sand saltation flux $q(z)$ from nine Wenglor YH03PCT8 electric laser gate sensors (*Barchyn et al.*, 2014), mounted at heights z spanning from 0.02 to 0.47 m above the surface. We converted the measured particle count to sand flux by calibrating to eight concurrently sampling Big Spring Number Eight (BSNE) samplers (*Fryrear*, 1986; *Goossens et al.*, 2000). We then obtained the total sand flux by integrating the flux through the depth of the saltation layer (see *Martin and Kok* (2017); *Martin et al.* (2018)). Furthermore, we obtained the dust concentration profile using six identical optical particle counters (OPCs) (the 212 ambient particulate profiler, manufactured by Met One Instruments, Inc.), of which we mounted four on the tower at four different heights at any given time within 0.74-6.44 m above the surface. Each OPC measured size-resolved aerosol concentrations using seven size bins with equivalent light scattering diameter ranges within 0.49-10 μm , calibrated using polystyrene

latex spheres (PSLs) (Table 2.1, column 1). Of the seven size bins, we only used the smallest six bins. Past studies have found that the sampling efficiency (i.e., the ratio of particle concentration measured by the sensor to the particle concentration in the ambient air; *Von der Weiden et al.* (2009)) can decrease strongly with wind speed for coarse particles; for instance, the loss rate can approach 100% for particles larger than 10 μm in diameter under strong wind events (*Von der Weiden et al.*, 2009). As the dependence of sampling efficiency on wind speed and particle size was not provided by the instrument’s manufacturer, we did not use the largest size bin (bin 7) and only used the smallest six bins (with PSL diameter ranging from 0.49 to 7 μm ; see Table 2.1). The optical sizing of aerosols is sensitive to differences in the refractive index between the measured aerosols and the particles used to calibrate the instrument (*Hinds*, 1999). The manufacturer calibrated the OPCs against PSLs, following the international standard ISO 21501-1:2009 (*ISO*, 2009). We corrected the manufacturer-provided bin size limits to dust size limits using Lorenz–Mie theory (*Bohren and Huffman*, 1983; *Mätzler*, 2002; *Rosenberg et al.*, 2012), thereby approximating dust as spherical particles. Specifically, we calculated the light scattered by PSLs (refractive index: $m = 1.59 - 0i$) at the instrument’s laser wavelength (589 nm) and scattering angle range ($90 \pm 60^\circ$; information provided by the Met One engineering department), using the manufacturer-provided size boundaries of each of the six OPC bins. For each bin, we then determined the size range of dust particles that would produce an equal range of scattered light, using globally representative dust refractive indices (real part $n = 1.53 \pm 0.03$ and imaginary part $k = -10^{-2.5 \pm 0.3}$, following *Kok et al.* (2017)). This operation yielded the corrected bin size boundaries for dust and their uncertainties (Table 2.1, column 2).

Using the instrumentation and procedure mentioned above, we obtained shear stress, total sand flux, and size-resolved dust concentration, which we averaged over 30 min periods. We chose a 30 min averaging time interval because this interval is shorter than the typical timescale of a mesoscale weather system but sufficient to capture most of the turbulent energy spectrum (*Stull*, 1988; *Sterk et al.*, 1998). Furthermore, we inter-calibrated the six OPCs to

reduce systematic errors in the measured dust concentration and to quantify the instrument uncertainty. To obtain measurements for this inter-calibration, we mounted five OPCs (the sixth one malfunctioned after 25 May 2015) at the same height and in a line perpendicular to the wind for 3 days (5, 6, and 7 June 2015) immediately following the field campaign. Specifically, for each of the six size bins, we applied linear-least-squares regression on the aerosol concentration of each of the five OPCs against the mean of the five OPCs. This procedure yielded a concentration-dependent correction factor with uncertainty for each size bin of each OPC, which we propagated throughout our analysis. For all of our subsequent analysis, we did not use dust concentrations measured by the malfunctioning OPC, because they did not satisfy our data-quality control criteria.

We used the calibrated dust concentration to obtain the size-resolved mass flux of emitted dust using the gradient method, which is analogous to the methods for determining vertical scalar fluxes from turbulent and molecular diffusion in the atmospheric surface layer (*Gillette et al., 1972; Shao, 2008*). The gradient method assumes constant dust flux within the surface layer, neutral atmospheric stability (see Fig. S2 of *Martin and Kok (2017)*), and negligible dust deposition from upwind sources, and it is expressed as

$$F_{d,i} = -K_d \frac{\partial c_i}{\partial z} \quad (2.1)$$

$$K_d = \eta \kappa u_* z \quad (2.2)$$

where $F_{d,i}$ is the vertical mass flux ($kgm^{-2}s^{-1}$) of the i th size class of the six bins; c_i denotes the mass concentration (kgm^{-3}) of the i th size class at height z (m); K_d is the turbulent diffusivity ($m^{-2}s^{-1}$) obtained by the mixing length theory (*Stull, 1988*); η is the ratio between the turbulent diffusivity of a passive tracer and that of momentum, which we take as unity based on previous studies (*Gillette et al., 1972; Stull, 1988*); κ is the von Kármán constant, which we take as 0.387 (*Andreas et al., 2006*); and u_* is the shear velocity (ms^{-1}). Combining Eqs. (2.1) and (2.2), and integrating from a reference height z_r (m), we

obtain

$$c_i(z) = c_i(z_r) - \frac{F_{d,i}}{\kappa u_* \eta} \ln\left(\frac{z}{z_r}\right) \quad (2.3)$$

where $c_i(z_r)$ is the reference concentration of the i th size class at z_r . For calculation purposes, we set z_r as the height of the ‘‘D1’’ OPC (Fig. 2.1). Applying Eq. (2.3) to each of the six bin classes yields the size-resolved vertical dust mass flux $F_{d,i}$ for each bin. We then obtained the bulk vertical mass flux as the sum of the size-resolved fluxes $F_d = \sum_{i=1}^6 F_{d,i}$. Note that for each bin, we only used measurements that showed a negative gradient (concentration decreases with height) and thus a positive dust flux, as discussed further below.

We used the size-resolved vertical dust flux obtained above to calculate the particle size distribution (PSD) of emitted dust and the sandblasting efficiency, which together give insights into the physical processes governing dust emission from active sands (*Kok et al.*, 2014b; *Mahowald et al.*, 2014). We computed the normalized volume PSD of dust at emission as

$$\frac{dV_i}{d\ln D_i} = \frac{F_{d,i}}{F_d \times \ln(D_{i+1}/D_i)} \quad (2.4)$$

where D_i (μm) and D_{i+1} (μm) are the lower and upper boundary geometric diameter sizes, respectively, of the i th size class (Table 2.1, column 2). The integral of $\frac{dV_i}{d\ln D_i}$ over particle size thus yields unity. For each size bin we then obtained the sandblasting efficiency, which is the vertical dust flux produced by a unit horizontal sand saltation flux (*Marticorena and Bergametti*, 1995),

$$\alpha_i = \frac{F_{d,i}}{Q} \quad (2.5)$$

where Q ($kgm^{-1}s^{-1}$) is the total horizontal sand flux integrated over all sand grain sizes (see *Martin and Kok* (2017)). We then obtained the bulk sandblasting efficiency α (m^{-1}) by summing over the six α_i (m^{-1}), $\alpha = \sum_{i=1}^6 \alpha_{d,i}$.

We used the size-resolved vertical mass flux calculated above to obtain the vertical flux for particulate matter with geometric diameter $D_g \leq 10 \mu m$ ($PM_{10,g}$) and with aerodynamic diameter $D_a \leq 2.5 \mu m$ ($PM_{2.5,a}$). Dust in atmospheric circulation models is usually represented in terms of geometric diameter (*Mahowald et al.*, 2014), and the $PM_{10,g}$ size range

is considered most relevant to dust impacts on weather and climate (*Kok et al.*, 2017). In contrast, aerodynamic diameter is more relevant to aerosol impacts on human health, which corresponds with the $PM_{2.5,a}$ concentration (*Burnett et al.*, 2014). To obtain the $PM_{10,g}$ flux, we summed the mass flux of the smallest six size bins and part of the seventh size bin that is within the $PM_{10,g}$ size range (see Table 2.1, column 2), for which we integrated over the sub-bin size distribution obtained by linear-least-squares regression on the PSD of the emitted dust of the sixth and seventh size bin. To obtain the $PM_{2.5,a}$ flux, we first converted the geometric diameter bin sizes to aerodynamic diameter bin sizes through (*Hinds*, 1999)

$$D_g = \sqrt{\frac{\chi\rho_0}{\rho_P}} D_a \quad (2.6)$$

where D_a and D_g are the aerodynamic and geometric diameter, respectively; $\rho_0 = 1000\text{kgm}^{-3}$ is the density of water; $\rho_P \approx (2.5 \pm 0.2) \times 10^3\text{kgm}^{-3}$ is the typical density of dust aerosols (*Kok et al.*, 2017); and χ is the dynamic shape factor, which is defined as the ratio of the drag force experienced by the irregular particle to the drag force experienced by a spherical particle with diameter D_g (*Hinds*, 1999). We used $\chi \approx 1.4 \pm 0.1$ (*Kok et al.*, 2014a), which yielded $D_g \approx (0.75 \pm 0.04) \times D_a$ (values of geometric and aerodynamic bin diameters are listed in Table 2.1). Second, we summed the mass flux of the smallest two size bins and part of the third size bin that is within the $PM_{2.5,a}$ size range (see Table 2.1, column 3), for which we integrated over the sub-bin size distribution obtained by linear-least-squares regression on the PSD of the emitted dust of the second and third size bin.

We found that aerosol concentration, vertical mass flux, and the PSD calculated with the procedure above were affected by both dust emission and sea-salt aerosol deposition. Specifically, we found deviations in the measured aerosol concentration profiles from the logarithmic profile expected to occur from an active dust emission source (*Stull*, 1988; *Kind*, 1992; *Gillies and Berkofsky*, 2004), a result that we inferred as the influence of sea-salt aerosol. Because we measured dust concentrations ~ 650 m from the shoreline, we expect increasing sea-salt aerosol concentration with height due to the upwind deposition of near-surface sea-salt aerosol (*Dueker et al.*, 2011; *Liang et al.*, 2016). We generally observed an

increasing concentration with height for the lowest two or three OPCs when saltation was inactive (horizontal saltation flux $Q = 0$), consistent with sea-salt aerosol deposition, but found a decrease in concentration with height when saltation was active ($Q > 0$), consistent with dust emission. Furthermore, the measured PSD was coarser when saltation was inactive than when it was active. This observation is consistent with sea-salt aerosol being coarser than dust aerosol (*O’Dowd and de Leeuw, 2007*) and dominating when dust emission is not occurring. We thus mitigated the problem of the influence of sea-salt aerosol on our results by using only the lowest two sensors (D1 and D2 in Fig. 2.1), which were most affected by dust emission and least affected by the upwind sea-salt aerosol emission. Indeed, using only the lowest two sensors caused the aerosol flux to be small and negative (deposition) when saltation was inactive and large and positive (emission) when saltation was active. Because using the lowest two sensors did not eliminate the deposition flux of sea-salt aerosol from our results, we in addition subtracted mass flux measured by D1 and D2 when saltation was inactive from the flux by D1 and D2 when saltation was active. We found the sea-salt deposition flux at Oceano was of the order of $0.1 \mu\text{gm}^{-2}\text{s}^{-1}$, which was roughly an order of magnitude smaller than measurements 50 m away from the shoreline in coastal Maine, USA (*Dueker et al., 2011*). Due to a lack of precise sea-salt deposition data in our measurements, we assumed the sea-salt aerosol deposition flux to be invariant to shear velocity. However, accounting for the possible dependence of sea-salt deposition flux on shear velocity does not qualitatively affect the PSD of dust at emission.

In order to characterize the sand grains at the experimental site, we collected four sand samples (each ~ 220 g) on 14 October 2016 from the upper 2 cm of the surface, with two samples at the tower location and two at 100 m upwind. We analyzed the properties of each sand sample using a series of physical and chemical techniques. First, we analyzed the particle size distribution (PSD) using the laser diffraction technique with the ANALYSETTE 22 MicroTec Plus, Fritsch (*Katra and Yizhaq, 2017*), which measured particles within 0.08-2000 μm in optical diameter. We calculated the PSD of soil samples with a Fraunhofer

diffraction model with a size resolution of $1 \mu\text{m}$ using MasControl software (*Katra and Yizhaq, 2017*). Note that we did not convert this soil PSD in terms of optical diameter into geometric or aerodynamic diameter due to a lack of information on particle shape, refractive index, scattering angle range, and laser wavelength. Second, we analyzed the mineralogical composition of the sand grains using the X-ray powder diffraction (XRPD) method (*Klute, 1986*). The XRPD method allows the crystal structure data to retrieve the minerals of a bulk sample. Each analyzed sample of 1 g contains hundreds of grains at the sand size of the Oceano site. Specifically, we used the Panalytical Empyrean powder diffractometer equipped with the position-sensitive detector X'Celerator (Philips 1050/70). Data were collected in the $\theta/2\theta$ geometry using $\text{CuK}\alpha$ radiation ($\lambda = 1.54178 \text{ \AA}$) at 40 kV and 30 mA. Scans were run over ~ 15 min intervals in a 2θ range of $4 - 60^\circ$ with a step equal to $\sim 0.033^\circ$ (*Sommariva et al., 2014*). The reference intensity ratio (RIR) method was used to determine the concentrations of the crystalline components. The integral intensities of main peaks were taken for computation (*Gualtieri, 1996, 2000*). Third, we performed a qualitative examination of the grain surfaces using scanning electron microscopy (SEM) (Quanta 200, FEI) and the energy dispersive X-ray spectroscopy (EDS) chemical analysis technique integrated within SEM. The SEM-EDS stimulates each sample using electrons and detects the spectrum of outgoing photons to retrieve the elemental analysis of the grain surfaces, which provided us with information on the mineralogy of grain coatings. In our case, each sample replica was composed of some dozens of particles, including sand-sized and dust-sized particles. It additionally provided images at extremely high magnification (6x to 1,000,000x) that enable a close analysis of the smallest dust particles ($< 2\mu\text{m}$).

2.3 Results

We find that dust emitted from the sand sheet at Oceano differs from dust emitted from non-sandy soils in two key ways. First, the vertical $PM_{10,g}$ and $PM_{2.5,a}$ dust fluxes at Oceano are both smaller than those fluxes from most non-sandy soils at the same shear velocity

(Fig. 2.2). The vertical $PM_{10,g}$ and $PM_{2.5,a}$ fluxes at Oceano range from 1 to 100 $\mu gm^{-2}s^{-1}$ and 0.1 to 30 $\mu gm^{-2}s^{-1}$, respectively. They both increase non-linearly with increasing shear velocity in the measured range of 0.29-0.43 ms^{-1} . For similar shear velocities, the $PM_{10,g}$ and $PM_{2.5,a}$ dust fluxes from most non-sandy soils exceed those at Oceano, differing by a factor of ~ 1 -100 and ~ 0.1 -10, respectively. The second key difference is that dust emitted from the Oceano site is substantially finer than size-resolved dust emitted from non-sandy soils under natural saltation (Fig. 2.3a), and it is also significantly finer than dust measured in situ over North Africa (Fig. 2.3b), which likely accounts for a majority of the world's dust emissions (*Prospero et al.*, 2002; *Engelstaedter et al.*, 2006).

Our measurement of the bulk sandblasting efficiency provides further insight into the differences between dust emissions from the Oceano sand sheet and from non-sandy soils. First, the bulk sandblasting efficiency at Oceano is around $10^{-6} m^{-1}$ (Fig. 2.5), which is substantially smaller than the range within 10^{-5} to $10^{-2} m^{-1}$ typical for non-sandy soils (*Kok et al.*, 2012). Second, the bulk sandblasting efficiency increases non-linearly as a power law in shear velocity (Fig. 2.5), a result consistent with some previous studies (*Shao et al.*, 1993; *Marticorena and Bergametti*, 1995; *Kok et al.*, 2012).

We find that the dependence of the sandblasting efficiency on shear velocity changes with dust size (Fig. 2.6), which explains the shift in the PSD of emitted dust to finer size with increasing shear velocity (Fig. 2.4). Specifically, the power law exponents of the dependence of the sandblasting efficiency on shear velocity are large and positive for the smallest five bins, whereas the exponent substantially drops to a negative value for bin 6 (Fig. 2.6). This explains the fining of the PSD of emitted dust with increasing shear velocity, which is almost entirely due to a decreased contribution of bin 6 (Fig. 2.4). We consider it likely that this decreased contribution from bin 6 (with D_g ranging from 6.21 to 9.14 μm ; see Table 2.1) with increasing shear velocity is caused by a decrease in sampling efficiency of coarse particles with wind speed (*Von der Weiden et al.*, 2009). Therefore, it is possible that the PSD of emitted dust remains approximately invariant with shear velocity.

Our analyses of sand grains sampled from the field site show that the Oceano sand is characterized by a uni-modal size distribution (mode at $461 \mu m$ and median at $491 \mu m$) with 0.95% (by mass) of loose clay- and silt-sized fine particles ($\sim 63 \mu m$) between the sand grains and 0.41% of particulate matter smaller than $10 \mu m$ (Fig. 2.7). The sand consists of a mixture of quartz (51% by mass), feldspars (K-rich feldspar 23% and plagioclase 23%), and clay minerals (3%) analyzed by the XRPD technique (Table 2.2). We further find the presence of mineral coatings on the top of quartz sand grains through the SEM-EDS technique (Fig. 2.8d and e). Note that the mass content of clay minerals detected in the XRPD analysis can be in the form of loose fine dust in the pore spaces between the sand grains and/or clay-mineral coatings attached to the sand grains. In addition, we find that the surface of the feldspars appears more abraded than the solid surface of the quartz sand grains (compare location “B” and location “C” in Fig. 2.8a), which are representative of a large number of SEM-EDS observations made for these samples.

2.4 Discussions

We reported in situ field measurements of natural dust emission from an undisturbed coastal sand sheet at Oceano Dunes in California (Fig. 2.1). We found that dust emission from these active sands differs in several key ways from dust emission from non-sandy soils, namely in the magnitude of vertical $PM_{10,g}$ and $PM_{2.5,a}$ dust fluxes (Fig. 2.2), the particle size distribution (PSD) of dust at emission (Fig. 2.3), and the magnitude and the shear velocity dependence of the sandblasting efficiency (Fig. 2.5). Furthermore, we found that sand grains at the study site are coarse with a mode larger than $460 \mu m$ (Fig. 2.7), that many sand grains contain clay-mineral coatings, and that about half of the sand grains are feldspars (K-rich feldspar and plagioclase) (Table 2.2). These results provide insights into several fundamental questions.

1. What physical processes drive dust emission from active Oceano sands?

2. How representative are dust emissions from the sand sheet at Oceano of active sands elsewhere?

3. What are the implications of dust emission from Oceano for downwind human health, park management, the hydrological cycle, and climate?

After addressing these questions, we end the discussion section with several limitations of our methodology.

2.4.1 Insights into processes producing dust from active sands at the Oceano Dunes State Vehicular Recreation Area

Our results indicate that aeolian abrasion of feldspars is one possible dust emission process at Oceano. XRPD analysis confirms the existence of feldspars ($\sim 46\%$ by mass) (Table 2.2). Although the content of feldspars is of the same magnitude as that of quartz ($\sim 51\%$ by mass) (Table 2.2), the surfaces of the feldspars commonly appear more abraded than the surfaces of the quartz sand grains (Fig. 2.8a), suggesting a higher potential to generate dust through aeolian abrasion of feldspars than of quartz grains. We list four supporting findings from other experimental studies. First, both laboratory (*Dutta et al.*, 1993; *Jari*, 1995) and wind tunnel (*Kuenen*, 1960, 1969) experiments have found that feldspars are more fragile than quartz grains to aeolian abrasion, possibly owing to the cleavage structures of feldspars (*Kuenen*, 1969) and the greater propensity of feldspars to weather than quartz (*Nesbitt et al.*, 1997). Second, the feldspar content of dust is higher than that of the parent top soils in dust-producing regions, including northern Ghana (*Tiessen et al.*, 1991), China (*Feng et al.*, 2008), and the UK (*Moreno et al.*, 2003), implying the preferential generation of dust from feldspars. Third, laboratory experiments have found that aeolian abrasion of feldspars can generate a larger fraction of the PM_{10} and the $PM_{2.5}$ size ranges than that generated from abrasion of quartz (*Domingo et al.*, 2010). Indeed, laboratory experiments on washed and clean quartz grains (for which grain surface minerals have been removed) (*Whalley et al.*, 1987; *Bullard et al.*, 2007) and on freshly crushed quartz grains (*Wright et al.*, 1998; *Wright*,

2001) imply that the dust produced by aeolian abrasion of quartz grains has a small portion (less than 1% by mass) within the PM_{10} size range. Fourth, *Pye and Sperling* (1983) found that when coastal dune sands are exposed to salt solutions under desert diurnal temperature and humidity cycles, feldspars are more susceptible to breakage into fine grains than quartz. Because the Oceano measurement site is exposed to high levels of sea-salt aerosols deposition (see Sect. 2.2), this finding further supports our hypothesis that aeolian abrasion of feldspars is one possible dust emission process at Oceano.

Our results further suggest that the removal of clay-mineral coatings by saltator impact is another possible contributor to dust emissions at Oceano, which is supported by the following two findings. First, XRPD analysis found the content of clay minerals to be around 3% by mass (Table 2.2) for Oceano sand samples, although the fraction of this contributed by clay-mineral coatings is uncertain because XRPD analysis cannot distinguish between clay-mineral coatings and loose clay-sized fines trapped in the pore spaces between sand grains (*Swet et al.*, 2019). However, the PSD of dust emitted from the Oceano site is generally consistent with the PSD of emitted dust of laboratory experiments on sand samples taken from Australian active sand dunes (*Bullard et al.*, 2004, 2007). Specifically, Bullard and co-workers simulated aeolian abrasion within an air chamber on the Australian sand grains with the content of clay-mineral coatings as $\sim 1\%$ - 2% by mass. They concluded that the removal of clay-mineral coatings was likely the main process for PM_{10} dust emissions, implying that the removal of clay-mineral coatings is a key emission process at Oceano as well. Second, a companion paper reports results of wind tunnel experiments on sand grains collected from our Oceano field site, as well as from two active desert dune fields in Israel (*Swet et al.*, 2019). They reported that all three sands produced substantial dust emissions, and their measured sandblasting efficiency of Oceano sands was consistent with our field measurements. After Swet and co-workers washed the sand grains from the two Israeli dune fields to remove most of the loose resident fines, leaving the clay-mineral coatings largely unchanged, they found that the washed sand grains still produced PM_{10} dust emissions that were comparable to

those before the sand was washed. Although (*Swet et al.*, 2019) did not perform this last experiment on Oceano sand, these results support the interpretation that removal of clay-mineral coatings is a key process driving dust emissions from active sands, including at Oceano.

Our results imply that sandblasting of resident fines by saltators is a third possible dust emission process at Oceano. The resident fines exist as single particles trapped in between the sand grains, as was observed when we washed sand samples in the lab. Although XRPD analysis cannot distinguish between clay-mineral coatings and clay-sized resident fines in the pore spaces between sand grains (*Swet et al.*, 2019), the content of these resident fines is less than 3% by mass (Table 2.2). Because we observed a net dust emission flux only when saltation was occurring, it is unlikely that the direct aerodynamic entrainment of resident fines (*Klose and Shao*, 2012) contributed substantially to dust emissions at Oceano. The occurrence of dust emission by removal of resident fines is supported by the measurements of *Swet et al.* (2019), which reported that unwashed sands produced more dust than washed ones.

Our results provide two insights into the energetics of dust emission from Oceano. First, the lower bulk sandblasting efficiency at Oceano, compared to that of non-sandy soils, supports the common hypothesis that sandblasting efficiency increases sharply with clay-sized grain content (*Marticorena and Bergametti*, 1995; *Kok et al.*, 2014a). Second, we find that the bulk sandblasting efficiency of Oceano sand increases as a power law with shear velocity (Fig. 2.5). Because such enhancement of the sandblasting efficiency occurs despite invariance of mean saltator velocity with shear velocity (*Martin and Kok*, 2017), such changes in sandblasting efficiency must be driven instead by changes in the probability distribution of the saltator impact energies. The recent dust emission model of *Kok et al.* (2014a) predicts a power law increase in the sandblasting efficiency with shear velocity for soils for which the typical saltator impact energy is substantially less than the threshold impact energy needed to overcome particle bonds. This power law increase occurs because, for such

erosion-resistant soils, only particularly energetic saltator impacts are capable of emitting dust, and the fraction of saltator impacts that are particularly energetic increases nonlinearly with wind shear velocity (see Fig. 16 in *Kok et al. (2012)* and Fig. 1 in *Kok et al. (2014a)*). As such, our results both tentatively support the *Kok et al. (2014a)* dust emission model and suggest that dust emission from Oceano sands are predominantly produced by saltators with an impact energy much greater than the mean impact energy (i.e., with impact energy in the high-energy tail of the saltator-impact-energy distribution). This dependence of dust emission on the very energetic saltator impacts likely occurs because both removal of clay-mineral coatings and aeolian abrasion of feldspars are energetic processes and thus require particularly energetic saltator impacts.

2.4.2 Insights into the representativeness of Oceano dust emissions for other active sands

It is unclear how representative our measurements on the active coastal sand sheet at Oceano are of dust emission from other active sands, including active sand dunes, in particular in relation to the sand size distribution, the content of feldspars, and the extensiveness of clay-mineral coatings.

Our results indicate that sand at our study site, with a mode around $461 \mu\text{m}$ (Fig. 2.7), is coarser than the sand of most active sand dunes (*Bullard et al., 2004; Pye and Tsoar, 2009; Webb et al., 2013; Swet et al., 2019*). Because the threshold shear velocity required to sustain saltation increases with the grain particle size (*Shao, 2008; Kok et al., 2012*), the value of 0.28 ms^{-1} we found at Oceano (*Martin and Kok, 2017; Martin et al., 2018*) is likely somewhat higher than that at typical active sand dunes, as also confirmed in the laboratory measurements of *Swet et al. (2019)*. As such, the horizontal saltation flux at Oceano could be somewhat lower compared with typical active sand dunes.

Our results further indicate that Oceano sand differs from the sand of typical active sand dunes in its mineralogy, specifically in the content of feldspars. Oceano sands contain as much

as $\sim 46\%$ feldspar by mass (Table 2.2). This content is approximately twice the proportion of feldspar found in coastal dunes along Monterey Bay to the north (*Combellick and Osborne, 1977*) and more than 3 times as much as in coastal dunes in Baja California to the south (*Kasper-Zubillaga et al., 2007*). This mineralogically immature sand suggests rapid erosion of a feldspar-rich source rock, potentially derived from the Santa Maria River drainage. More mineralogically mature terrestrial dune fields, including most old and continentally based (as opposed to coastal) terrestrial desert sand seas and some older coastal dunes, are quartz-dominated and feldspar-depleted (*Pye and Tsoar, 2009; Swet et al., 2019*). The removal of feldspars by ballistic-impact-derived breakdown into dust during aeolian recycling over long periods of time contributes to the mineralogical maturation (into quartz-dominated deposits) of aeolian dune sands (*Muhs et al., 1997; Muhs, 2004*).

Furthermore, weathering of feldspars to clay minerals might produce some of the clay-mineral coatings on sand grains (*O'Hara-Dhand et al., 2010*) at the study site. Feldspars in the Oceano sand, especially plagioclase, are vulnerable to chemical weathering under the humid and salt-bearing coastal conditions (*James et al., 1981; Pye and Tsoar, 2009*) and mechanical breakdown (aeolian abrasion) into dust from saltator impacts in wind events (*Muhs et al., 1997*). Additionally, *Compton (1991)* described how the Santa Maria basin source sediments, both onshore and off-shore, contained very fine clays derived from the alteration of volcanic glass mediated by and enhanced by weathering of feldspars. As a result, the combination of abundant feldspars in the Oceano sand and clay minerals from an additional source could help explain the observed clay-mineral coatings on Oceano sand and the fine-grained characteristics of Oceano dust emissions.

Our results also imply that the dust emission processes at Oceano are not main contributors to dust emissions from North Africa. In situ measurements of the PSDs of atmospheric dust over North Africa are significantly coarser than the PSD of dust emitted from our Oceano site (Fig. 2.3b) and the PSD of dust generated in laboratory experiments on the removal of clay-mineral coatings (*Bullard et al., 2004, 2007*). As such, although the processes

responsible for dust emission from the Oceano sand sheet - removal of clay-mineral coatings and aeolian abrasion of feldspars - could be important for specific North African dust sources, they are likely not primary dust emission processes on a regional scale in North Africa.

2.4.3 Implications of dust emissions from the Oceano Dunes State Vehicular Recreation Area for downwind human health, park management, the hydrological cycle, and climate

Dust emitted from our Oceano site is significantly finer than dust emitted from non-sandy soils (Fig. 2.3a), which can amplify its impacts on downwind human health, the hydrological cycle, and climate. Fine dust has a longer lifetime and therefore is usually transported over longer distances than coarse dust (*Mahowald et al.*, 2014). Furthermore, fine dust, especially within the $PM_{2.5,a}$ size range, is associated with cardiopulmonary diseases, lung cancer, and ischemic heart disease (*Burnett et al.*, 2014). On a per mass basis, dust emitted from Oceano, and from other source regions with similar emission processes, can thus be expected to have greater risks to downwind human health than dust emitted from non-sandy soils.

Our measurements of dust emission from the Oceano Dunes State Vehicular Recreation Area (SVRA) could help inform decisions on the management of this California state park. Our measurements were performed in the part of the park where public off-highway-vehicle (OHV) use is prohibited, and we found that substantial dust emissions occur in the absence of OHV use. Because OHV use can enhance dust emissions (*Goossens and Buck*, 2011; *Goossens et al.*, 2012), reconfiguring motorized access to the park could modify dust emissions and associated downwind dust impacts on human health, vegetation, and water quality (*Ouren et al.*, 2007). Measurements by *Gillies et al.* (2017) (see their Fig. 10) indicated a positive relationship between airborne PM_{10} and wind speed in a section of the Oceano Dunes SVRA with vehicular activity; however, their measurements of riding area dust concentrations are not directly comparable to our calculated non-riding area dust emission fluxes. Disentangling the relative contributions of natural and OHV-influenced

dust emissions will be essential as the Oceano Dunes SVRA responds to a dust emission abatement order recently approved by the local air pollution control district hearing board (Vaughan, 2018).

Dust emitted from Oceano sands possibly contains a large proportion of feldspars and thus might modify downwind cloud microphysics and hydrology. Oceano sand has $\sim 46\%$ feldspars by mass (Table 2.2), which is on the high end for dust-source regions (Murray *et al.*, 2012; Atkinson *et al.*, 2013). Consequently, the content of feldspars in dust emitted from Oceano is likely on the high end as well, especially considering that aeolian abrasion of feldspars (Muhs *et al.*, 1997) could be one of the emission processes. Feldspars, especially K-rich feldspars, are considered the most important ice nuclei for mixed-phase clouds, based on both laboratory (Atkinson *et al.*, 2013) and in situ measurements (Price *et al.*, 2018). Recent observations suggest that cloud glaciation mediated by dust aerosols contributes to more than half of the ice-phase precipitation in the Sierra Nevada mountain range (Creamean *et al.*, 2013), which is a major source of water for California residents (Dettinger *et al.*, 2004). Because Oceano sands are rich in feldspars, we speculate that dust emitted from Oceano could potentially contribute to glaciating downwind clouds, thereby affecting precipitation in the Sierra Nevada region. Future measurements to determine the broader occurrence of dust production by feldspar abrasion for active sands with high feldspar content are thus clearly needed.

Our findings that dust emitted from Oceano sands is relatively fine, and that the dust flux is on the low end of that emitted from non-sandy soils, indicate the need for substantial further study to understand the role of dust emissions from active sands in past, current, and future climates. Partially because fine dust has a longer lifetime and larger surface area per unit mass than coarse dust (Mahowald *et al.*, 2014), it produces a substantial cooling radiative effect (Kok *et al.*, 2017). Therefore, it is important to include size-resolved dust emission in climate studies. However, the parameterization of dust emissions from active sands in climate models is difficult because of a scarcity of measurements of dust emissions

from active sands. Although our measurements help to fill this gap, it remains unclear how representative our measured fine dust emissions from coastal Oceano sands are for typical active sands. Therefore, there is a clear need for future investigations of dust emissions from active sands for a range of geomorphological and sand properties, including grain size distribution, mineralogy (such as extents of clay-mineral coatings and feldspars), chemical and physical weathering rates, dune type, and palaeoenvironmental history.

A further complication in representing the role of dust emissions from active sands in climate models is that sand dunes can transition between stable and active states in past, current, and future climates. Many stable dunes have accumulated extensive clay-mineral coatings (*Bowler, 1973; Gardner and Pye, 1981; Muhs et al., 1997*), and, if activated, these dunes could possibly produce substantial fine dust emissions through sandblasting-induced removal of clay-mineral coatings (*Bullard et al., 2007; Swet et al., 2019*). The transition from stable to active sand dunes can be triggered by increases in wind speed or decreases in vegetation coverage, which in turn can be caused by decreased precipitation or by human activities, such as grazing and land-use change (*Ashkenazy et al., 2012*). Areas with coexisting active and stable sand dunes, such as coastal zones, are especially vulnerable to the reactivation of stable sand dunes (*Yizhaq et al., 2009*) and could thus become potent dust emission sources, especially if the dunes experienced some weathering in the humid, salt-rich coastal environment (*Muhs et al., 1997*). Because active sands are generally not represented as dust emission sources in climate models, reactivation of sand dunes might thus enhance future dust effects on climate beyond what current models simulate (*Kok et al., 2018*).

2.4.4 Limitations of the methodology

Our methodology has important limitations. First, our XRPD analysis could not distinguish the concentrations of clay-mineral coatings from loose individual fine particles contained in the pore spaces between sand grains. This uncertainty limits our interpretation of the relative contributions of removal of clay-mineral coatings and saltation-driven release of loose fines

to our measured dust fluxes. Second, we did not collect aeolian dust samples simultaneously with the field measurements. Instead, we collected soil samples on 14 October 2016, more than a year after the field measurements in the summer of 2015, such that it is possible that these samples are not representative of the sand surfaces at the time of our field campaign. However, sand-surface properties over a large area are unlikely to change substantially within a timescale of 1 year (*Hillel*, 1998). Third, we approximated dust as spherical particles when correcting the OPC bin sizes, although dust is highly aspherical (*Okada et al.*, 2001; *Kandler et al.*, 2007). Because OPC measurements use side-scattered light to determine dust size, which remains poorly understood (*Nousiainen and Kandler*, 2015), we followed past work (*Sow et al.*, 2009; *Rosenberg et al.*, 2014; *Ryder et al.*, 2018) in approximating dust as spheres. Fourth, we did not quantify the effect on the measured PSD due to the dependence of the sampling efficiency on particle size and wind speed (*Von der Weiden et al.*, 2009), which might be important especially for the largest particle bin (bin 6), as suggested by the decrease in sandblasting efficiency with shear velocity for this bin, which contrasts with the increase with shear velocity for the smaller particle bins. Therefore, it is possible that the PSD of emitted dust (Fig. 2.4) remains invariant with shear velocity.

2.5 Conclusions

We presented the first (to our knowledge) in situ field measurements of dust emissions under natural saltation from an active sand sheet at the coastal Oceano Dunes in California (Fig. 2.1). We found that although the $PM_{10,g}$ dust emitted from Oceano is on the low end of the range in emissions produced by non-sandy soils for similar wind speed (Fig. 2.2a), it is also substantially finer (Fig. 2.3a) such that the $PM_{2.5,a}$ flux is comparable in magnitude to dust emitted from non-sandy soils (Fig. 2.2b). As fine dust has a longer atmospheric lifetime, is associated with adverse impacts on human health, and produces a cooling radiative effect, dust emissions from Oceano could impact downwind climate and human health.

Our results provide insights into the physical processes that drive dust emissions from the sand sheet at Oceano Dunes. We found that Oceano sand has substantial clay-mineral coatings and feldspars (Table 2.2), suggesting that dust is emitted through a combination of removal of clay-mineral coatings, release of resident fines, and ballistic breakdown of feldspars by saltation impacts. As feldspars are the most efficient ice nuclei for mixed-phase clouds, we speculate that dust emitted from Oceano could potentially contribute to glaciating downwind clouds, thereby affecting precipitation in the Sierra Nevada region.

Our measurements provide limited insights into the contribution of active sands to the global dust cycle. We found that the PSD of dust emitted from Oceano is much finer than that observed in situ over North Africa (Fig. 2.3b). Therefore, although the processes responsible for dust emission at our Oceano site - removal of clay-mineral coatings and aeolian abrasion of feldspars - could be important for specific North African dust sources, they are likely not primary dust emission processes on a regional scale in North Africa. However, because it is unclear how representative the dust emission processes at our Oceano site are for emission processes occurring at typical active sands, the contributions of active sands to dust emission from North Africa and other globally important source regions remain uncertain. Further work on dust emissions from active sands with various properties (sand size distribution, mineralogy, chemical and physical weathering rates, dune type, and palaeoenvironmental history) is thus needed to evaluate the contribution of active sands to the global dust cycle.

Acknowledgements. We acknowledge support from the National Science Foundation (NSF) grants AGS-1358621 and AGS-1552519 to Jasper F. Kok, NSF Postdoctoral Fellowship EAR-1249918 to Raleigh L. Martin, United States-Israel Binational Science Foundation (BSF) grant 2014178 to Jasper F. Kok and Itzhak Katra, National Oceanic and Atmospheric Administration (NOAA, US Department of Commerce) Educational Partnership Program

agreement no. NA16SEC4810006 to Thomas E. Gill, and Brazilian National Council for Scientific and Technological Development (CNPq) fellowship to Livia S. Freire. We thank Hezi Yizhaq, Marcelo Chamecki, Francis A. Turney, Jack A. Gillies, Richard P. Langford, and Cenlin He for helpful comments and discussions. We thank Peter Rowland and Tim Pesce at the Oceano Dunes State Vehicular Recreation Area for access and transportation support to the Oceano field site. We also thank Vicken Etyemezian and an anonymous reviewer for constructive comments and suggestions that improved the quality and clarity of our paper.

2.6 Tables and figures

Table 2.1: The dust geometric and aerodynamic diameters of the seven bin boundaries. Determination of the geometric diameter ranges uses Lorenz–Mie theory such that they produce the same range of scattered light intensity as the seven manufacturer-provided polystyrene latex sphere (PSL) diameter sizes. The ranges in geometric diameters derive from the uncertainty in the dust refractive indices. We determined the aerodynamic diameter ranges by applying Eq. (2.6) to the geometric diameter ranges.

Polystyrene latex sphere (PSL) diameter (μm)	Dust geometric diameter (μm)	Dust aerodynamic diameter (μm)
0.49	0.51 – 0.54	0.68 – 0.72
0.7	0.73 – 0.77	0.97 – 1.03
1	1.01 – 1.03	1.35 – 1.37
2	2.18 – 2.32	2.91 – 3.09
2.5	2.67 – 2.90	3.56 – 3.87
5	6.11 – 6.31	8.15 – 8.41
7	8.89 – 9.40	11.85 – 12.53

Table 2.2: Averaged mineralogy of the Oceano Dunes sand samples in unit of percentage by mass, determined from X-ray powder diffraction (XRPD) analysis. Note that the values in the table are averages of mineralogy of four 1 g samples with two collected from the tower location and two from 100 m upwind. Each analyzed sample contains hundreds of grains.

	Quartz	Potassium feldspar (Microcline and Orthoclase)	Sodium-rich plagioclase feldspar (Albite)	Clay minerals (Illite)
Oceano Dunes	51	23	23	3



Figure 2.1: The experimental setup at Oceano Dunes. Instrumentation includes six sonic anemometers (S1–S6), nine Wenglor particle counters (W1–W9), eight Big Spring Number Eight sand samplers (A1–A4, B1–B4), four optical particle counters (D1–D4), and a weather station with temperature and humidity sensors (WS) (following *Martin and Kok* (2017)).

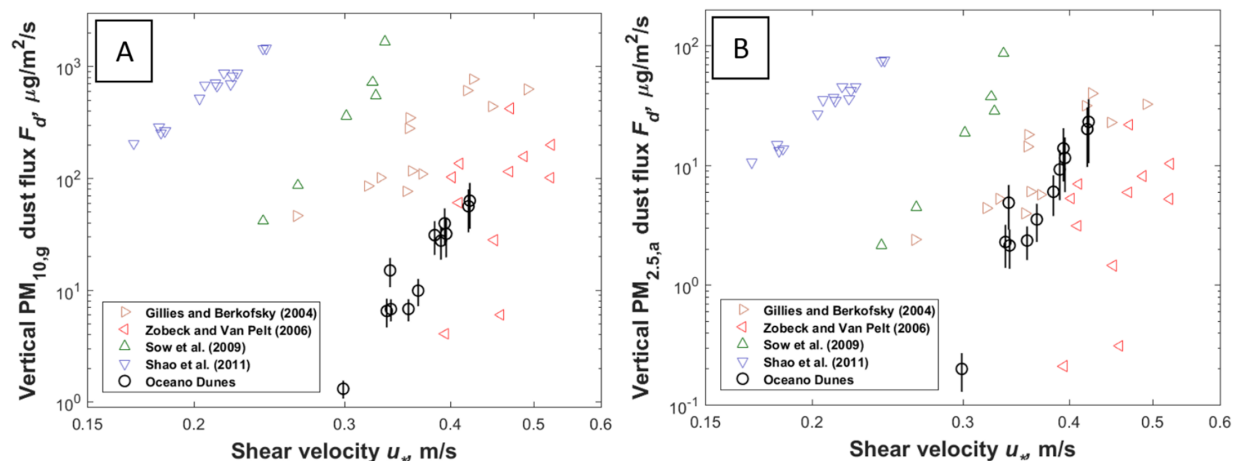


Figure 2.2: The vertical dust mass flux as a function of shear velocity within (a) the $PM_{10,g}$ geometric diameter range and (b) the $PM_{2.5,a}$ aerodynamic diameter range. Each of the two plots includes measurements at Oceano (black open circles) and previously published field studies of natural dust emissions from non-sandy soils (open triangles). These latter measurements were compiled in *Kok et al. (2014a)*, which corrected these measurements to the $PM_{10,g}$ geometric diameter range following the procedure described in that work. Furthermore, we corrected these measurements to the $PM_{2.5,a}$ aerodynamic diameter range assuming that their PSDs follow the prediction of the brittle fragmentation theory generated by aggregate fragmentation (*Kok, 2011a*). Error bars on the Oceano measurements were obtained through error propagation.

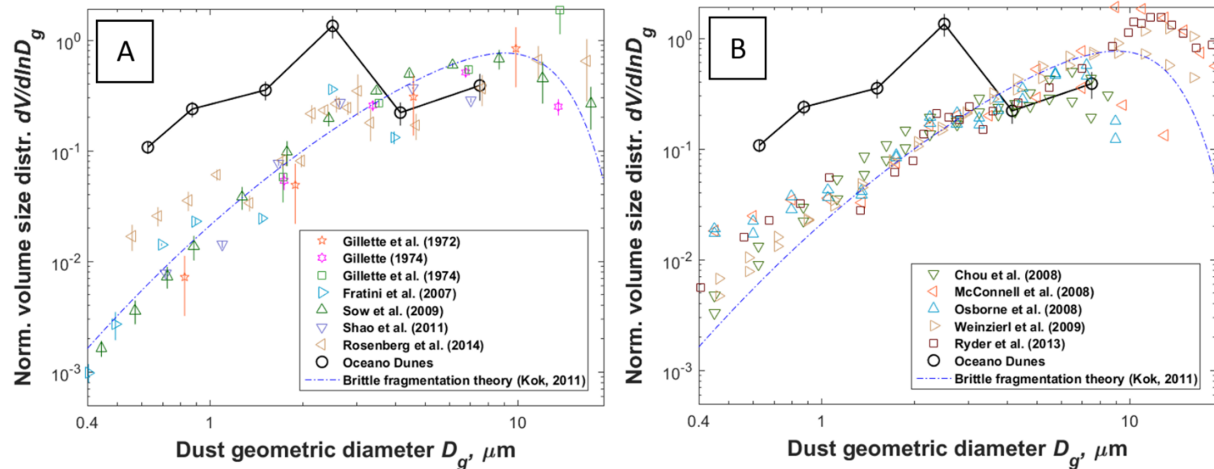


Figure 2.3: Normalized volume particle size distribution (PSD) of dust at emission as a function of the dust aerosol geometric diameter averaged over all measurements at Oceano (black open circles). Plotted for comparison are measurements compiled by *Kok et al.* (2017) of (a) the emitted dust PSDs from non-sandy soils in the US (*Gillette et al.*, 1972, 1974; *Gillette*, 1974), China (*Fratini et al.*, 2007), North Africa (*Sow et al.*, 2009; *Rosenberg et al.*, 2014), and Australia (*Shao et al.*, 2011a) and (b) in situ aircraft measurements of dust-dominated PSDs close to the Saharan source regions. Note that these measurements are normalized using the procedure described in *Kok* (2011a) and *Kok et al.* (2017), which differs somewhat from the procedure used for the Oceano data (see Sect. 2.2). Also plotted for comparison is the brittle fragmentation theory (dashed-dotted blue lines) on the PSD of emitted dust generated by aggregate fragmentation (*Kok*, 2011a). Error bars on the Oceano measurements were obtained through error propagation.

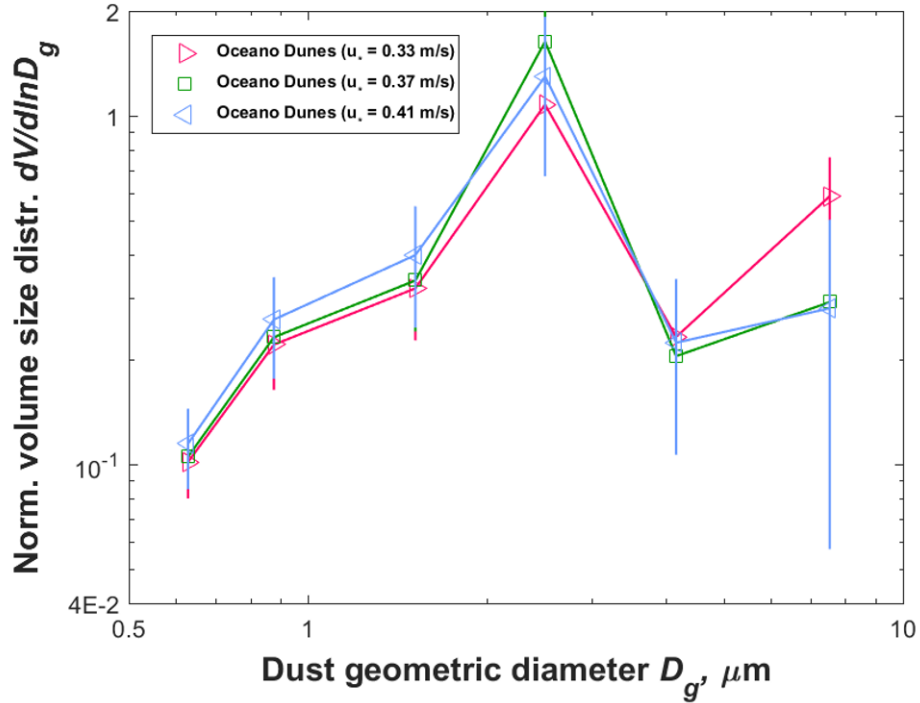


Figure 2.4: Shear velocity dependence of the normalized volume particle size distribution of dust at emission at Oceano. We divided the measurements evenly into three shear velocity bins, with averaged values of 0.33, 0.37, and 0.41 $m s^{-1}$, respectively. Error bars on the measurements were obtained through error propagation.

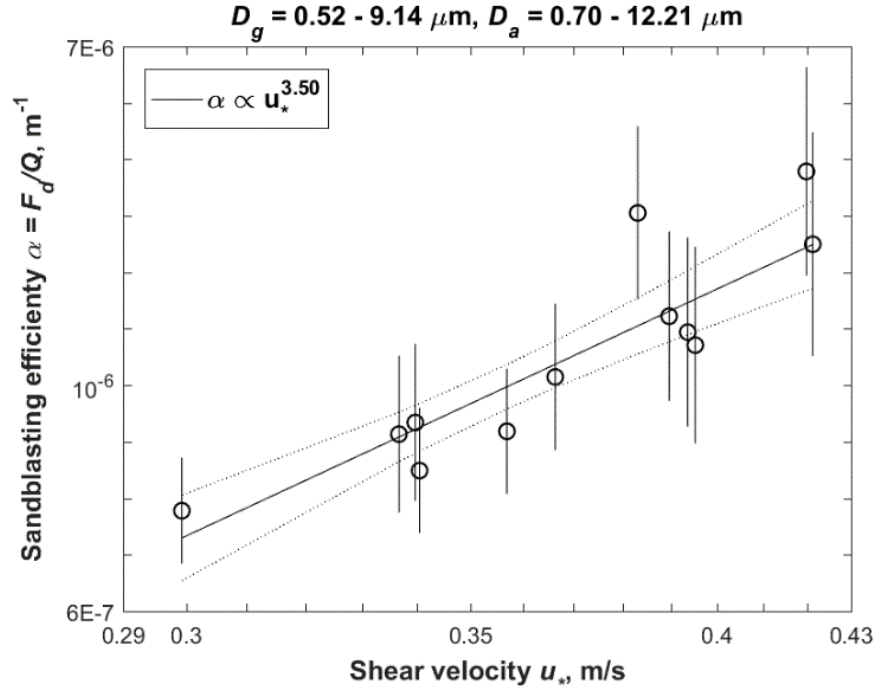


Figure 2.5: The bulk sandblasting efficiency α (m^{-1}) at Oceano as a function of shear velocity. The linear-least-squares fit (black line) indicates that α increases as a power law in shear velocity with an exponent of 3.50 ± 0.89 . Error bars were obtained by propagating errors from the sensor inter-calibration process, the regression used in the gradient method, and the subtraction of the sea-salt deposition flux. The two dotted black lines denote the 95% confidence range on the fit. The geometric and the aerodynamic diameter ranges of the vertical dust mass flux F_d are noted at the top, and Q is the total horizontal sand flux integrated over all sand grain sizes (*Martin et al., 2018*).

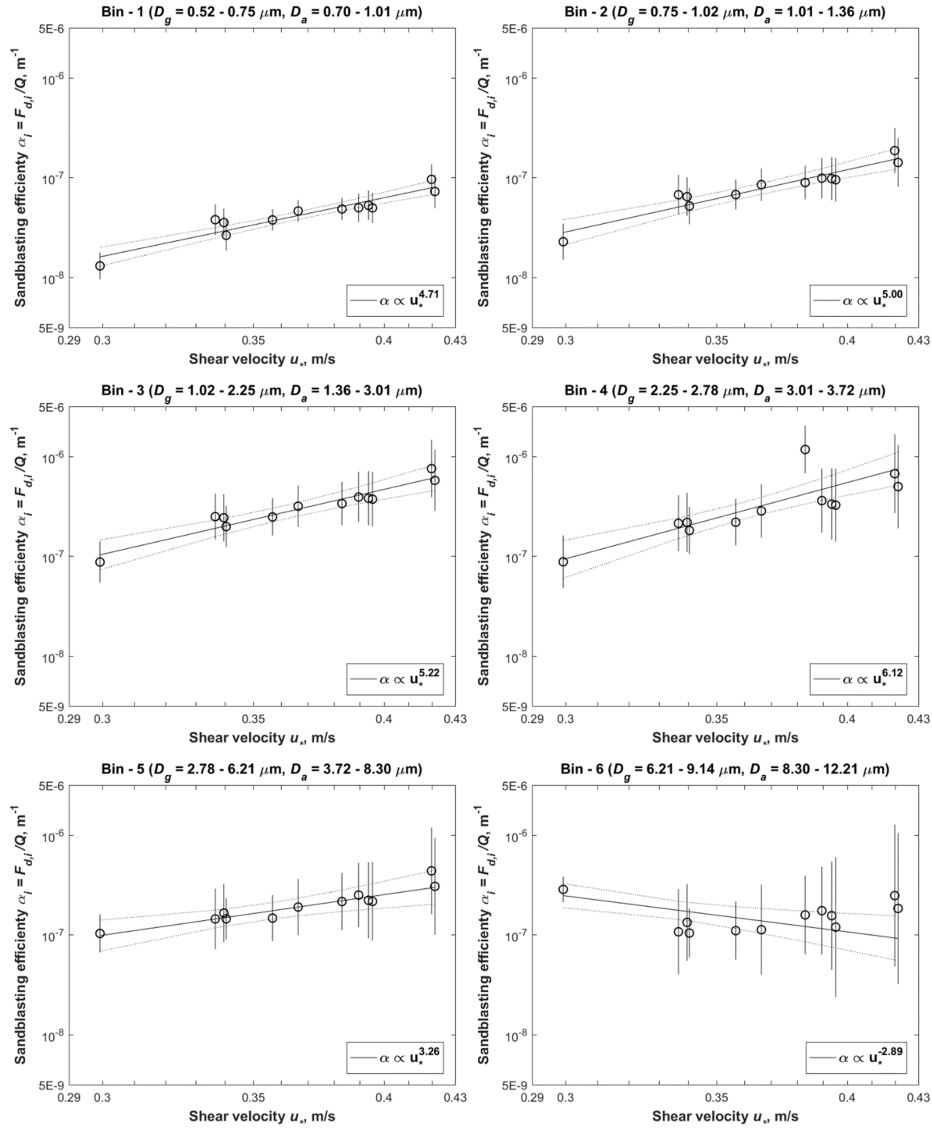
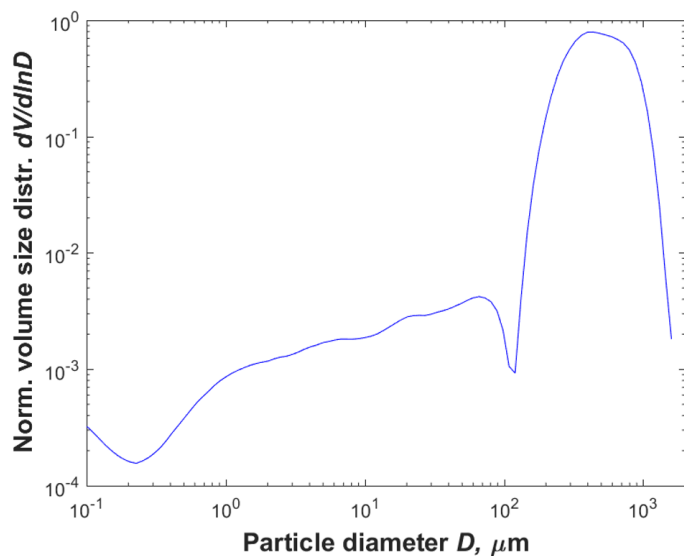


Figure 2.6: The sandblasting efficiency α_i (m^{-1}) of the six size bins at Oceano as a function of shear velocity. The linear-least-squares fit (black line) indicates that α_i varies as a power law in shear velocity with an exponent of 4.71 ± 0.97 , 5.00 ± 1.37 , 5.22 ± 1.63 , 6.12 ± 2.11 , 3.26 ± 1.90 , and -2.89 ± 1.94 for the six respective size bins. The two dotted black lines denote the 95% confidence range of the fit. The geometric and aerodynamic diameter ranges of the vertical dust mass flux $F_{d,i}$ are noted at the top of each plot, and Q is the total horizontal sand flux integrated over all sand grain sizes (Martin *et al.*, 2018).



	Oceano
Statistical parameters (μm)	
Mean	538.28
Mode	461.48
D10	270.61
D50	490.95
D90	879.67
Weight fraction (%)	
Clay-sized ($< 2 \mu\text{m}$)	0.16
Clay- and Silt-sized ($< 63 \mu\text{m}$)	0.95
Fine sand ($63\text{-}250 \mu\text{m}$)	7.93
Medium sand ($250\text{-}500 \mu\text{m}$)	54.35
Coarse sand ($> 500 \mu\text{m}$)	44.69
PM ₁ ($< 1 \mu\text{m}$)	0.09
PM _{2.5} ($< 2.5 \mu\text{m}$)	0.19
PM ₁₀ ($< 10 \mu\text{m}$)	0.41

Figure 2.7: Normalized volume particle size distribution (PSD) of sand samples collected from the Oceano field site. Statistical parameters of the PSD are reported in the table to the right. D10, D50, and D90 refer to cut-off diameters of the 10th, 50th, and 90th percentiles of sample grains by mass, respectively. Note that the values are averages of four samples with two collected from the tower location and two from 100 m upwind.

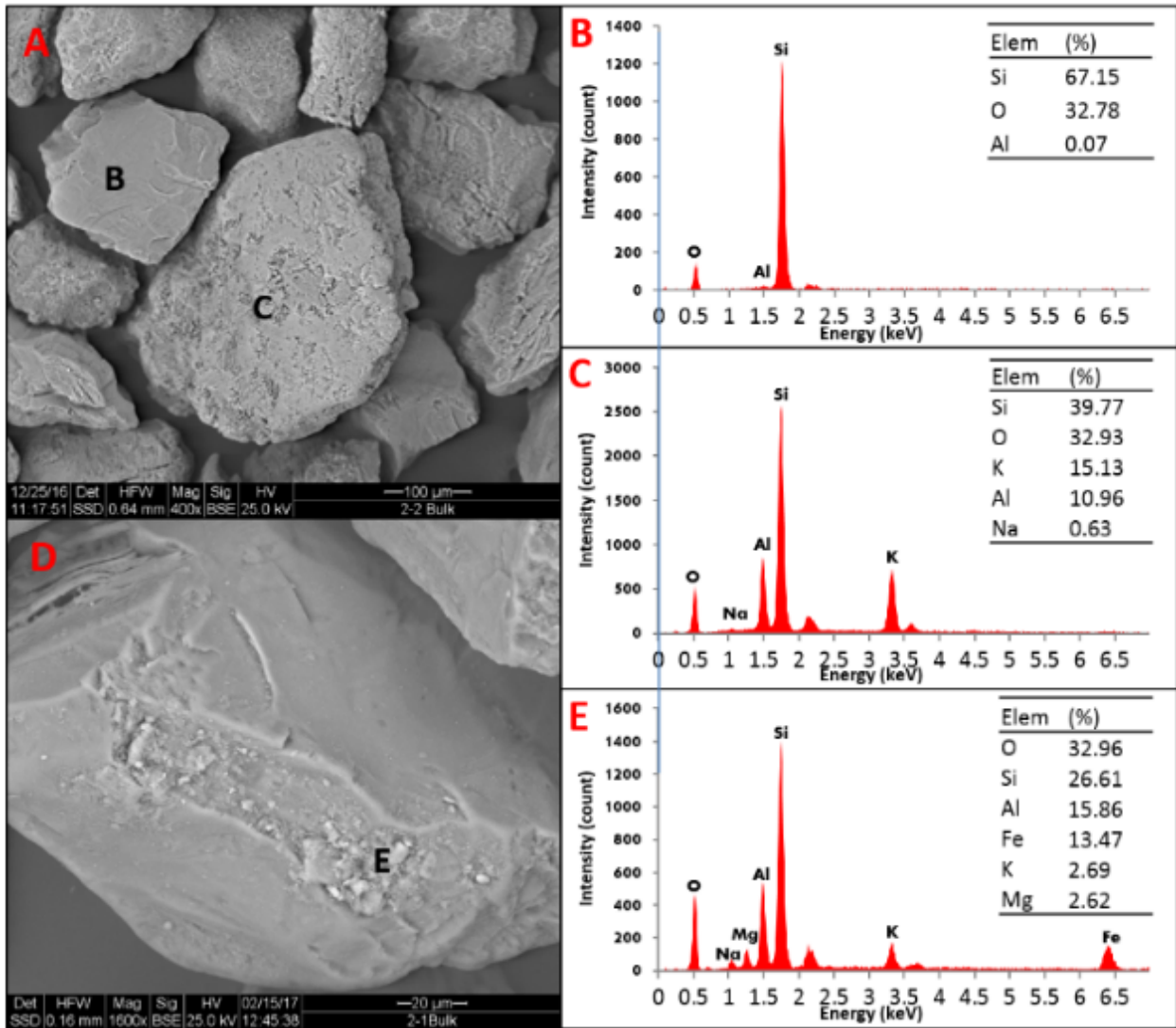


Figure 2.8: (a) Scanning electron microscopy (SEM) image of an Oceano sand sample. (b) Energy dispersive X-ray spectroscopy (EDS) chemical composition (percentage by mass) of a quartz grain in (a) (the location of the analysis is marked by the black letter “B”). (c) EDS chemical composition of a K-rich feldspar in (a) marked by the black letter “C”. (d) Close-up image of a quartz sand grain with mineral coatings. (e) EDS chemical composition of the mineral coatings in (d) marked by the black letter “E”.

CHAPTER 3

Climate models and remote sensing retrievals neglect substantial desert dust asphericity

[**Huang, Y.**, J. F. Kok, K. Kandler, H. Lindqvist, T. Nousiainen, S. Tetsu, A. A. Adebiyi, and O. Jokinen (2020), Climate models and remote sensing retrievals neglect substantial desert dust asphericity, *Geophysical Research Letters*, 47(6), <https://doi.org/10.1029/2019GL086592>.]

Abstract

Climate models and remote sensing retrievals generally assume that dust aerosols are spherical or spheroidal. However, measurements show that dust aerosols deviate substantially from spherical and spheroidal shapes, as ratios of particle length to width (the aspect ratio) and height to width (height-to-width ratio) deviate substantially from unity. Here, we quantify dust asphericity by compiling dozens of measurements of aspect ratio and height-to-width ratio across the globe. We find that the length is on average 5 times larger than the height and that climate models and remote sensing retrievals underestimate this asphericity by a factor of ~ 3 -5. Compiled measurements further suggest that North African dust becomes more aspherical during transport, whereas Asian dust might become less aspherical. We obtain globally-averaged shape distributions, from which we find that accounting for

dust asphericity increases gravitational settling lifetime by $\sim 20\%$. This increased lifetime helps explain the underestimation of coarse dust transport by models.

3.1 Introduction

Desert dust is the dominant aerosol type by mass in the atmosphere (*IPCC AR5*, 2013). It produces important effects on the Earth system, including by directly modulating the radiation budget (*Kok et al.*, 2017; *Pérez et al.*, 2006), modifying cloud microphysics (*DeMott et al.*, 2003), catalyzing heterogeneous chemistry (*Usher et al.*, 2002), and fertilizing ecosystems (*Jickells et al.*, 2005). Furthermore, dust aerosols affect regional air quality (*Huang et al.*, 2019; *Mahowald et al.*, 2007), producing hazards to human health (*Burnett et al.*, 2014). These varied impacts depend on the optical and aerodynamic properties of desert dust. Because the optical and aerodynamic properties of aspherical dust differ significantly from volume-equivalent spherical dust (*Nousiainen and Kandler*, 2015; *Yang et al.*, 2013), dust impacts are sensitive to the shape of dust aerosols.

Although an accurate quantification of dust shape is thus important for calculating dust impacts, current representations of dust shape in climate models and remote sensing retrievals conflict with in situ measurements. Most current climate models approximate dust aerosols as spherical particles (Figure 3.5a) (*Mahowald et al.*, 2014), while retrieval algorithms of passive remote sensing instruments approximate dust as spherical or spheroidal particles (Figures 3.5b and 3.5c). For example, the Version 2 and Version 3 inversion algorithms of the ground-based Aerosol Robotic Network (AERONET) use precomputed lookup tables of the single-scattering properties of spheroidal dust to retrieve dust properties (*Dubovik et al.*, 2006). A second example is the Version 23 operational retrieval algorithm of the satellite-borne Multiangle Imaging Spectroradiometer (MISR), which approximates coarse-mode dust as spheroids, medium-mode dust as cubic blocks, and fine-mode dust as spheres (*Kalashnikova et al.*, 2005). That is, climate models and remote sensing retrievals assume that either

all three or two of the three dimensions of dust aerosols are equal (Figure 3.5). However, several in situ measurements have shown that the ratios of dust length to its width and dust height to its width deviate substantially from unity (e.g., *Okada et al.* (2001)). As such, both climate models and remote sensing retrievals likely underestimate dust asphericity by assuming that at least two of the three dimensions are equal. This possible bias in climate models and remote sensing retrievals can propagate into calculations of dust impacts. For instance, as dust asphericity slows gravitational settling by increasing aerodynamic drag at a given volume and mass (*Yang et al.*, 2013), this bias toward spherical dust might have caused an underestimation of dust dry lifetime.

To facilitate accounting for dust asphericity in climate models and remote sensing retrievals, here we compile dozens of measurements of dust shape across the globe. To do so, we first introduce the shape descriptors that we use to quantify dust asphericity in section 3.2. In section 3.3, we then present the compiled results of the shape descriptors, globally and regionally. In section 3.4, we use our compiled shape distributions to quantify the enhancement of gravitational settling lifetime due to dust asphericity. Our results show that dust asphericity has been substantially underestimated by climate models and remote sensing retrievals, which helps explain the underestimation of coarse dust transport by climate models.

3.2 The shape descriptors of aspherical dust

The most widely used descriptors to quantify dust asphericity are the aspect ratio (AR) and the height-to-width ratio (HWR), which are less sensitive to microscopic image resolution and artifacts than other shape descriptors (*Almeida-Prieto et al.*, 2007; *Kandler et al.*, 2011). In remote sensing retrievals, AR is the ratio of a particle’s length to its height (e.g., *Dubovik et al.* (2006)), whereas HWR is normally not used as dust particles are normally approximated as spheroids (Figure 3.5). However, in in-situ measurements, the AR is usually taken as the ratio

of the largest dimension of a particle’s projected area (the length) to the perpendicular dimension of the projected area (the width; see Figure 3.1a). Further, the height is usually taken as the dimension perpendicular to the collection surface (the height; see Figure 3.1b). Because most impactor-collected dust particles deposit with their smallest dimension perpendicular to the collection surface, the HWR usually equals a particle’s smallest dimension (the height) divided by the smaller dimension on the projected area (the width) (*Okada et al.*, 2001; *Sakai et al.*, 2010).

3.2.1 Measurements of the aspect ratio and the height-to-width ratio

To quantify AR, many studies have measured the particle length and width of two dimensional (2-D) scanning electron microscopic (SEM) images of individual dust particles (e.g., *Reid et al.* (2003)). Specifically, individual dust aerosols are usually collected on filters by ground-based or aircraft-carried impactors (e.g., *Kandler et al.* (2007)), after which 2-D top view SEM images of the collected particles were obtained. These 2-D images were then analyzed to obtain the length and width of individual dust particles (e.g., *Kandler et al.* (2007)). The length L is usually taken as the longest distance between two points on the outline of the projected area (Figure 3.1a). Although the length is usually defined consistently between measurements (e.g., *Okada et al.* (2001); *Sakai et al.* (2010)), a systematic difference exists between the two common definitions of the width. Some studies obtained the width W_{perp} as the maximum distance that is perpendicular to L (Figure 3.1a) (e.g., *Okada et al.* (2001)). In contrast, other studies obtained the width $W_{ellipse}$ as the minor axis of an ellipse with an area equal to that of the particle’s projected area and with L as its major axis (Figure 3.1a) (e.g., *Kandler et al.* (2007)). In this latter case, studies have found that the ratio of the two dimensions of the projected area (i.e., AR) follows a modified lognormal distribution (e.g., *Kandler et al.* (2007)),

$$f(AR) = \frac{1}{\sqrt{2\pi} \times (AR - 1) \times \sigma_a} \exp\left(-\frac{1}{2} \times \left(\frac{\ln(AR - 1) - \ln(\bar{\varepsilon}_a - 1)}{\sigma_a}\right)^2\right) \quad (3.1)$$

where σ_a is the geometric standard deviation of the deviation of AR from unity (AR-1) and $\bar{\varepsilon}_a$ is the median of AR.

A subset of studies that measured AR also measured the dust height, the dimension of the particle perpendicular to the collection plane surface (see Figure 3.1b). After impactors collected individual dust particles onto filter planes, five different microscopic methods were used to measure dust height. First, *Okada et al.* (2001) and *Sakai et al.* (2010) used a shadow technique to determine the heights of thousands of dust particles. Second, *Chou et al.* (2008) and *Woodward et al.* (2015) used atomic force microscopy to record the height profiles of tens of dust particles. Third, *Osada* (2013) used scanning laser microscopy to measure the particle volume, used SEM to measure the 2D projected area of the same particle, and then combined data of the volume and projected area to determine the heights of hundreds of dust particles. Fourth, *Jeong et al.* (2016) used SEM to measure the 2D projected area and then cut the particles vertically by a focused ion beam to measure the cross-section height of tens of dust particles. Finally, *Lindqvist et al.* (2014) used two 2D SEM images of the same particle recorded at different viewing angles and then used stereography to retrieve the heights of tens of dust particles. In the present study, we assume that there is no systematic difference between the five different types of measurements, because any systematic errors are unknown (to our knowledge). Those studies that obtained extensive data sets (*Okada et al.*, 2001; *Osada*, 2013; *Sakai et al.*, 2010) have found that the ratio of the height to the width (i.e., HWR) follows a lognormal distribution

$$f(HWR) = \frac{1}{\sqrt{2\pi} \times HWR \times \sigma_h} \exp\left(-\frac{1}{2} \times \left(\frac{\ln(HWR) - \ln(\bar{\varepsilon}_h)}{\sigma_h}\right)^2\right) \quad (3.2)$$

where σ_h and $\bar{\varepsilon}_h$ are, respectively, the geometric standard deviation and median of HWR.

3.2.2 Addressing the systematic difference in particle width

Measurements of AR and HWR are affected by the systematic difference in the two common definitions of the particle width. We address this systematic difference between measure-

ments of W_{perp} and $W_{ellipse}$ using shape measurements of 13 dust particles collected from the Saharan Mineral Dust Experiment campaign (SAMUM; *Lindqvist et al. (2014)*) and two dust particles collected from the African Monsoon Multidisciplinary Analyses campaign (AMMA; *Chou et al. (2008)*). For each of the 15 particles, we computed W_{perp} and $W_{ellipse}$ and found that the average correction factor ($c = \frac{W_{perp} - W_{ellipse}}{W_{ellipse}}$) is $13.7\% \pm 2.7\%$ (Table 3.1). Because of the small number of dust particles, we further calculated the correction factors of 1261 African and 681 Asian laboratory-generated dust particles (*Sakai et al., 2010*), for which the average correction factor is $27.2\% \pm 0.4\%$ for all 1941 dust particles (Figure 3.6). This correction factor is larger than that of the 15 SAMUM and AMMA dust particles, due to unknown dependence of the correction factor on the physical and chemical properties (such as particle size, mineralogy, and morphology). Although the representativeness of laboratory-generated dust particles is unclear, because of its extensive number of sampled dust particles, we took $c = 20\% \pm 6\%$ as the approximate average of the two data sets with a large uncertainty range that covers both data sets. We thus linked W_{perp} and $W_{ellipse}$ by

$$W_{ellipse} = \frac{W_{perp}}{1 + c} \quad (3.3)$$

3.3 Measurement compilation of dust shape descriptors

We compiled dozens of measurements of AR and HWR of dust aerosols across the globe (see the map of measurement sites in Figure 3.7). Specifically, for each measurement, we first found the published medians of AR and HWR (Column 8 of Tables 3.2 and 3.3) and applied equation (3.3) to correct all medians that used W_{perp} instead of $W_{ellipse}$ (Column 10 of Tables 3.2 and 3.3). We correct W_{perp} to $W_{ellipse}$ because $W_{ellipse}$ quantifies the particle's projected area, which is strongly linked to its aerodynamic and optical properties (*Mahowald et al., 2014*). Second, we obtained the geometric standard deviations of AR-1 and HWR by fitting lognormal distributions (equations (3.1) and (3.2)) to data of the probability functions of AR ($= \frac{L}{W_{ellipse}}$) and HWR ($= \frac{H}{W_{ellipse}}$), corrected to $W_{ellipse}$ if needed. These lognormal

fits used the median AR and HWR obtained from Step 1. Third, we grouped the medians and geometric standard deviations by source regions (Asian or North African sources) and transport distance (source, short-range transport, or long-range transport). Finally, we averaged all medians and geometric standard deviations to obtain the globally-averaged shape distributions of AR and HWR of dust aerosols. Although our methodology is subject to a few limitations (see section 3.5), our compilation yields a number of key findings.

First, dust shape shows little dependence on particle diameter in the range of $0.1 - 20\mu\text{m}$ (Figure 3.2). Although some individual measurements find a dependence of AR on dust diameter (e.g., *Kandler et al. (2007)*; *Reid et al. (2003)*), a regression with all available data shows that AR is proportional to dust diameter with a small exponent of 0.011 ± 0.010 , which is statistically not different from zero. Although the HWR decreases more substantially with dust size, with a power law exponent of -0.06 ± 0.35 , this dependence is not statistically significant. The ratio of dust length to its height (LHR; Figure 3.2e), obtained by combining AR and HWR, increases somewhat with dust diameter, but this increase is also not statistically significant, with a power law exponent of 0.04 ± 0.36 .

Second, the dependence of AR on source region is less than thought. We find that the averaged median AR of North African dust is 1.72 ± 0.02 and that of Asian dust is 1.60 ± 0.08 . Although the AR of North African dust might thus be larger than that of Asian dust (p value = 0.001 from Student's t test), this regional difference is much less than concluded in previous studies (e.g., *Formenti et al. (2011)*; *Li and Osada (2007)*) due to the systematic difference in the definition of particle width (Figure 3.1a). Specifically, measurements of Asian dust have quantified AR and HWR in terms of W_{perp} (e.g., *Li and Osada (2007)*), whereas measurements of North African dust have generally used W_{ellipse} (e.g., *Reid et al. (2003)*) (see Tables 3.2 and 3.3). Since W_{perp} is systematically larger than W_{ellipse} (Table 3.1 and Figure 3.6), this has caused measurements of Asian dust to report a smaller AR than measurements of North African dust. Furthermore, the averaged median HWR of North African dust is 0.60 and that of Asian dust is 0.35 ± 0.07 . Although this

difference is statistically significant (p value = 0.04), it is uncertain due to a scarcity of measurements of HWR, especially for North African dust, for which only one measurement has been published (*Jeong et al.*, 2016).

Third, North African dust becomes more aspherical during transport, whereas Asian dust may become less aspherical (Figure 3.3). For North African dust, the median of AR increases from 1.60 ± 0.07 in source regions to 1.66 ± 0.03 for short-range transported dust and 1.90 ± 0.04 for long-range transported dust. The differences between source regions and long-range transported dust (p value = 0.001) and between short- and long-range transported dust (p value = 0.002) are statistically significant. Our finding that the median of North African AR increases substantially during transport agrees with previous studies (e.g., *Coz et al.* (2009); *Formenti et al.* (2011)). This increase in particle asphericity during transport is likely due to the preferential settling of spherical particles, which have a greater terminal fall speed than aspherical particles of the same volume (*Yang et al.*, 2013). In contrast to this increase in dust asphericity during transport of North African dust, we find that the median AR of Asian dust decreases during transport from 1.64 ± 0.07 in source regions and short-range transported dust to 1.58 ± 0.05 for long-range transported dust. Although this difference is not significant at the 5% level (p value = 0.25), this finding indicates that, for Asian dust, a second mechanism offsets the increase in asphericity due to preferential settling of spherical particles during transport. In particular, chemical processing with sea salts and humic acids can form a uniform coating around the mineral core and therefore decrease particle asphericity during transport (*Alexander et al.*, 2015; *Laskina et al.*, 2013; *Zhang*, 2008). This process seems substantially more important for Asian than for North African dust (*Denjean et al.*, 2015). Furthermore, the medians of AR close to source region are statistically not distinguishable between North African and Asian dust (Figures 3.3b and 3.3d). This enables a simple shape distribution of dust in source regions.

Finally, both climate models and remote sensing retrievals substantially underestimate dust asphericity by overestimating the ratio of dust height to its length. The globally-

averaged medians of AR and HWR are 1.70 ± 0.03 and 0.40 ± 0.07 (Figure 3.2), such that a dust aerosol’s length is on average 5 times greater than its height (Figure 3.2f). In contrast, climate models and remote sensing retrievals assume that dust is spherical or spheroidal, thereby equating at least two of the three dimensions. As a consequence, climate models and remote sensing retrievals underestimate dust asphericity by a factor of ~ 3 -5 (Figure 3.2e).

3.4 Lifetime enhancement due to dust asphericity

The substantial underestimation of dust asphericity by climate models and remote sensing retrievals could produce important errors in determining the impacts of dust on the Earth system. The compiled globally-averaged shape distributions of AR and HWR in Figures 3.2 and 3.3 can thus be used to more accurately calculate dust impacts, such as through improved estimates of dust lifetime, optics, and effects on clouds and heterogeneous chemistry. Here, we quantify the effect of dust asphericity on the gravitational settling lifetime of dust, which is neglected in most current climate models (*Mahowald et al.*, 2014).

Gravitational settling of dust aerosols occurs in the Stokes regime as the Reynolds number is far less than 1 (*Kok et al.*, 2012). In the Stokes regime, the terminal velocity of a spherical particle is (e.g., *Hinds* (1999))

$$v_{sph} = \frac{g \times \rho_p}{18 \times \mu} \times D^2 \quad (3.4)$$

where g is the gravitational acceleration, $\rho_p \approx 2.5 \times 10^3 \text{ kgm}^{-3}$ is the typical density of dust aerosols (*Kok et al.*, 2017), $\mu \approx 1.81 \times 10^{-5} \text{ Pa} \times \text{s}$ is the dynamic viscosity of air, and D is the diameter of the spherical particle. In analogy to equation (3.4), we express the terminal velocity of an aspherical particle as follows:

$$v_{asp} = \gamma \times \frac{g \times \rho_p}{18 \times \mu} \times D_g^2 \quad (3.5)$$

where D_g is the volume-equivalent (geometric) diameter and $\gamma = \frac{v_{asp}}{v_{sph}}$ is the asphericity factor, which equals unity for spherical particles and decreases with increasing particle asphericity

at a given volume. To obtain γ , we use a recent study (*Bagheri and Bonadonna, 2016*) to quantify γ as a function of the three dimensions of triaxial ellipsoidal particles (L , W , and H ; Figure 3.5d). This study uses extensive measurements and numerical simulations in the Stokes regime and finds (see their equations (13), (24), and (25))

$$\frac{v_{sph}}{v_{asp}} \equiv k_s = \frac{1}{2} \left(F_s^{\frac{1}{3}} + \frac{1}{F_s^{\frac{1}{3}}} \right) \quad (3.6)$$

$$F_s = \frac{D_g^3}{L^{2.3} \times W^{0.7}} \quad (3.7)$$

where $D_g = \sqrt[3]{L \times W \times H}$. The parameter F_s can be expressed as $HWR \times (\frac{1}{AR})^{1.3}$; $F_s = 1$ for spherical particles and decreases as dust asphericity increases (i.e., an increase of AR and/or decrease of HWR). By combining equations (3.5, 3.6, and 3.7), we obtained the terminal velocity of ellipsoidal particles as a function of its three dimensions.

We used the globally-averaged shape distributions of AR and HWR of dust aerosols to obtain the enhancement of gravitational settling lifetime due to dust asphericity (Figure 3.4). Specifically, we first used Monte Carlo sampling to randomly generate a large number (10^8) of dust particles from the two lognormal distributions of AR and HWR. Second, for each of these generated particles, we used equations (3.5, 3.6, and 3.7) and equation (3.4), respectively, to obtain its terminal velocity and that of its volume-equivalent spherical particle. Finally, for each dust particle, we calculated the reduction in terminal velocity (as $1 - \frac{v_{asp}}{v_{sph}}$) and the enhancement of the gravitational settling lifetime (as $\frac{T_{asp} - T_{sph}}{T_{sph}} = \frac{v_{sph}}{v_{asp}} - 1$). Note that $T_{asp} \propto \frac{1}{v_{asp}}$ and $T_{sph} \propto \frac{1}{v_{sph}}$ are the gravitational settling lifetimes of aspherical dust and its volume-equivalent spherical dust, respectively.

We find that accounting for dust asphericity decreases gravitational settling speed by $\sim 15\%$ (Figure 3.4a). This value is larger than the $< 5\%$ reduction in gravitational settling speed reported by *Ginoux (2003)* for dust $< 20\mu m$ in diameter. Because *Ginoux (2003)* approximated dust as prolate spheroids (Figure 3.5b) with a median AR of 1.5, this study underestimated dust asphericity by overestimating dust height. As a result, *Ginoux (2003)* underestimated the reduction in gravitational settling speed due to particle asphericity.

We further find that the reduction in gravitational settling speed due to dust asphericity increases the lifetime with respect to gravitational settling by $\sim 20\%$ (Figure 3.4b). Because coarse dust is primarily removed from the atmosphere by gravitational settling (*Mahowald et al.*, 2014), this finding helps explain why climate models generally underestimate the amount of coarse dust ($D > 5\mu\text{m}$) in the atmosphere (*Adebisi et al.*, 2020). Specifically, measurements of dust size distributions have found that more coarse dust particles are present in the atmosphere than simulated in climate models (e.g., *Ansmann et al.* (2017); *Ryder et al.* (2018); *van der Does et al.* (2018)). Several mechanisms have been proposed that could contribute to this modeled underestimation of coarse dust, including turbulent vertical mixing in dust layers (*Gasteiger et al.*, 2017), electrostatic charging of dust (*Harrison et al.*, 2018), and numerical diffusion (*Ginoux*, 2003). Although future work is needed to test whether accounting for dust asphericity indeed improves dust simulations in global models, our finding that dust asphericity results in a $\sim 20\%$ increase in dust lifetime indicates that dust asphericity also contributes to the underestimation of coarse dust in climate models.

3.5 Limitations of methodology

Our methodology is subject to a few important limitations. First, we assume that AR and HWR are not correlated. This simplification is supported by *Sakai et al.* (2010), whose data show only a small correlation of 0.17 between AR and HWR for 1941 dust particles. Second, our methodology is unable to account for several smaller systematic differences that exist between studies, due to, for instance, different software algorithms used in measuring particle dimensions. Third, we assume that dust aerosols are randomly oriented in the atmosphere in section 3.4, following *Ginoux* (2003) and *Bagheri and Bonadonna* (2016). However, especially larger dust particles could assume a preferential orientation that increases their drag (*Ulanowski et al.*, 2007; *Westbrook*, 2008). This would reduce the terminal velocity of coarse dust more than we estimated and strengthen our conclusion that dust asphericity contributes to the underestimation of coarse dust by climate models. Fourth, we approx-

imate dust as tri-axial ellipsoidal particles and do not consider the effect of dust surface roughness (*Kalashnikova et al.*, 2005). As surface roughness leads to a greater surface area and therefore a larger drag force, this could also cause an underestimation of the reduction in terminal velocity. Finally, we use size-invariant globally-averaged medians and geometric standard deviations of AR and HWR and therefore neglect any dependence of the enhancement of gravitational settling lifetime on dust size and source region. As HWR may decrease with dust size (Figure 3.2c), we may overestimate the reduction in terminal velocity for fine dust and underestimate it for coarse dust.

3.6 Conclusions

Current climate models and remote sensing retrievals approximate dust aerosols as spherical or spheroidal particles and therefore assume that either all three or two of the three dimensions of dust aerosols are equal. Here, we showed that this assumption causes climate models and remote sensing retrievals to substantially underestimate dust asphericity. We showed this by compiling dozens of measurements of the AR and the HWR of dust aerosols across the globe. These compiled measurements indicate that North African dust becomes more aspherical during transport, most likely because of preferential settling of spherical particles. In contrast, Asian dust may become less aspherical during transport, possibly because of chemical processing. When combining all available measurements, our compilation shows that the largest dimension of dust aerosols is on average 5 times larger than the smallest dimension. Consequently, the assumption in climate models and remote sensing retrievals that at least two dimensions are equal causes an underestimation of dust asphericity by a factor of $\sim 3 - 5$.

This underestimation of dust asphericity could produce important errors in calculations of dust impacts on the Earth system. For instance, using the compiled globally-averaged shape distributions of AR and HWR, we find that accounting for dust asphericity increases

dust lifetime with respect to gravitational settling by $\sim 20\%$. This increased lifetime helps explain the underestimation of coarse dust transport by models (*Ansmann et al.*, 2017; *Huneus et al.*, 2011).

The globally-averaged shape distributions of dust aerosols obtained in this paper can be used to inform more accurate calculations of dust impacts on the Earth system. This includes better estimates of dust lifetime, dust optics, and dust impacts on cloud and heterogeneous chemistry.

Acknowledgements. The authors thank the two anonymous reviewers for their constructive comments that helped to improve the manuscript. Y. H. acknowledges the support from the National Aeronautics and Space Administration (NASA) Grant 80NSSC19K1346, awarded under the Future Investigators in NASA Earth and Space Science and Technology (FINESST) program. J. F. K is funded by the National Science Foundation (NSF) Grants 1552519 and 1856389. K. K. is funded by Deutsche Forschungsgemeinschaft (DFG, German Research Foundation)- 416816480. H. L. is funded by the Academy of Finland Grant 285421. A. A. is funded by the University of California President’s Postdoctoral Fellowship. The authors further thank Kazuo Osada, Gholamhossein Bagheri, Gi Young Jeong, Paula Formenti, and Adriana Rocha-Lima for providing experimental data and thank Evan Variano, Ralph Kahn, Olga Kalashnikova, Aliaksandr Sinyuk, Marcelo Chamecki, and Robert Green for insightful discussions. Compiled dust shape data are listed in the supporting information Tables 3.2 and 3.3. Code scripts used in section 3.4 are available in a publicly accessible repository (<https://doi.org/10.5281/zenodo.3633351>).

3.7 Tables and figures

Table 3.1: The correction factor between the two common definitions of particle width of 15 dust particles.

		Length L (μm)	Width W_{perp} (μm)	Width W_{ellipse} (μm)	Correction factor $\frac{W_{\text{perp}} - W_{\text{ellipse}}}{W_{\text{ellipse}}}$	Mean (standard error)	Mean (standard error)
Dust from SAMUM campaign	Cal 01	5.6	3.7	3.6	2.2%	13.5% (3.0%)	13.7% (2.7%)
	Cal 02	14.4	8.6	7.4	15.8%		
	Dol 01	6.7	5.9	5.3	10.4%		
	Mix 02	7.7	6.1	4.8	28.3%		
	Mix 03	12.0	8.5	7.0	21.4%		
	Sil 04	7.5	7.1	5.5	28.9%		
	Sil 05	18.5	5.4	5.4	0.3%		
	Sil 06	5.0	2.6	2.6	0.7%		
	Sil 07	2.4	1.2	0.9	27.9%		
	Sil 08	6.9	3.6	3.6	0.3%		
	Qtz 01	3.1	2.0	1.8	15.7%		
	Agg 07	22.3	20.6	18.6	10.9%		
	Agg 10	18.5	16.5	14.7	12.8%		
Dust from AMMA campaign	Particle 1	1.1	0.9	0.8	6.0%	15.0% (9.0%)	
	Particle 2	3.4	2.1	1.7	24.0%		

Table 3.2: List of measurements of the aspect ratio (AR) by individual particle analysis.

Study	Data source from the study in the first column	Published formula of AR	Location (measurement techniques, date)	Attribution	Number of dust particles analyzed	Bin size range in terms of projected area-equivalent diameter	Values of AR using formula in the second column		Corrected AR, if formula in the third column is not $L/W_{ellipse}$		
							Median	Geo std (95% CI)	Median (SE)	Geo std (95% CI)	
Okada et al. (1987)	Fig. 4	$\frac{L}{W_{perp}}$	Nagoya Japan (Ground-based, 14 Apr. 1979)	Long-range transported Asian dust	35	1 – 6 μm	1.35	0.82 (0.66, 1.07)	1.62 (0.08)	0.49 (0.39, 0.64)	
Okada et al. (2001) – Qira	Fig. 2	$\frac{L}{W_{perp}}$	Qira China (Ground-based, 21 Feb. 1991)	Dust over Asian source region	1900	0.2 – 12.2 μm	1.36	1.09 (1.05, 1.12)	1.63 (0.08)	0.57 (0.55, 0.59)	
Okada et al. (2001) – Zhangye	Fig. 2	$\frac{L}{W_{perp}}$	Zhangye China (Ground-based, 27 Apr. to 7 May 1991)	Dust over Asian source region	3355	0.2 – 6.6 μm	1.40	1.01 (0.99, 1.04)	1.68 (0.08)	0.57 (0.56, 0.58)	
Okada et al. (2001) – Hohhot	Fig. 2	$\frac{L}{W_{perp}}$	Hohhot China (Ground-based, 23 Apr. to 29 Apr. 1991)	Short-range transported Asian dust	1743	0.2 – 6.6 μm	1.35	1.03 (1.00, 1.07)	1.62 (0.08)	0.55 (0.53, 0.56)	
Reid EA et al. (2003)	Fig. 9	$\frac{L}{W_{ellipse}}$	Puerto Rico (Aircraft, 5 to 24 Jul. 2000)	Long-range transported African dust	59120	0.1 – 0.3 μm	1.86	0.60 (0.59, 0.60)			
						0.3 – 0.75 μm	1.88	0.72 (0.71, 0.72)			
						0.75 – 2 μm	1.81	0.73 (0.72, 0.74)			
						2 – 5 μm	1.86	0.69 (0.68, 0.70)			
						5 – 10 μm	1.96	0.68 (0.68, 0.69)			
					1829	10 – 20 μm	2.27	0.66 (0.64, 0.68)			
Reid JS et al. (2003)	Fig. 4	$\frac{L}{W_{ellipse}}$	Puerto Rico (Aircraft, 16 Jul. 2000)	Long-range transported African dust	17000	1 – 25 μm	1.95	0.63 (0.63, 0.64)			
Kandler et al. (2007)	Table 7	$\frac{L}{W_{ellipse}}$	Izaña Tenerife (Ground-based, 13-23 Jul. 2005, 6-8 Aug. 2005)	Short-range transported African dust		1034	0.25 – 0.5 μm	1.99	0.65		
						2681	0.5 – 1 μm	1.75	0.63		
						5690	1 – 2.5 μm	1.62	0.66		
						9027	2.5 – 5 μm	1.57	0.65		
						2853	5 – 10 μm	1.68	0.63		
					391	10 – 20 μm	1.76	0.61			
Li and Osada (2007)	Fig. 3	$\frac{L}{W_{perp}}$	Mt. Tateyama Japan (insoluble dust in snow due to wet deposition, inferred Asian dust event on 11 Feb. 2001)	Long-range transported Asian dust	1706	2 – 40 μm	1.35	0.84 (0.81, 0.87)	1.62 (0.08)	0.48 (0.46, 0.49)	
			Mt. Tateyama Japan (insoluble dust in snow due to dry deposition, inferred Asian dust event on 3 Feb. 2001)	Long-range transported Asian dust	1400	2 – 18 μm	1.25	0.79 (0.76, 0.82)	1.50 (0.08)	0.45 (0.44, 0.47)	
			Mt. Tateyama Japan (insoluble dust in snow due to wet deposition, inferred Saharan dust event on 3 Jan. 2001)	Long-range transported Asian dust	5797	2 – 18 μm	1.25	0.80 (0.79, 0.81)	1.50 (0.08)	0.42 (0.41, 0.42)	
Chou et al. (2008)	Fig. 7	$\frac{L}{W_{ellipse}}$	Niger (Aircraft, 10 Jan. 2006 – 3 Feb. 2006)	Dust over African source region	31000	0.1 – 0.3 μm	1.61	1.01 (0.99, 1.02)			
						0.3 – 0.75 μm	1.61	0.96 (0.95, 0.98)			
						0.75 – 2 μm	1.68	0.97 (0.95, 0.98)			
						2 – 5 μm	1.63	0.99 (0.97, 1.01)			
						5 – 10 μm	1.68	0.98 (0.96, 0.99)			

Coz et al. (2009)	Table 7	$\frac{L}{W_{ellipse}}$	Madrid Spain (Ground-based, 2004-2005)	Long-range transported African dust	16904	2.4 – 4 μm	1.83	0.81	
					10874	4 – 10 μm	1.80	0.79	
Kandler et al. (2009)	Table 5	$\frac{L}{W_{ellipse}}$	Tinfou Morocco (Ground-based, 22 May and 3 Jun. 2006)	Short-range transported African dust	74000	0.5 – 50 μm	1.58	0.65	
Sakai et al. (2010) - Asia	Data from Tetsu Sakai	$\frac{L}{W_{ellipse}}$	Huining China (Sand samples from Nishikawa et al., 2000)	Artificial dust	681	0.06 – 2 μm	1.94	0.63 (0.60, 0.67)	
Sakai et al. (2010) - Africa	Data from Tetsu Sakai	$\frac{L}{W_{ellipse}}$	Tessalit Mali (Sand samples, from Schutz and Sebert, 1987)	Artificial dust	1261	0.06 – 0.9 μm	1.62	0.71 (0.68, 0.74)	
Matsuki et al. (2010)	Fig. 3	$\frac{L}{W_{ellipse}}$	Niamey Niger (Aircraft, 2- 19 Aug. 2006), dust particles in stratocumulus clouds	Ice Nuclei in stratocumulus clouds	334	1 – 5 μm	1.36	0.92 (0.86, 1.00)	
Kandler et al. (2011)	Table 5	$\frac{L}{W_{ellipse}}$	Cape Verde (Ground-based, 13 Jan. 2008 – 11 Feb. 2008)	Short-range transported African dust	3582	0.15 – 0.5 μm	1.45	0.67	
					13046	0.5 – 50 μm	1.68	0.60	
Scheuvens et al. (2011)	Data from Konrad Kandler	$\frac{L}{W_{ellipse}}$	Ouarzazate Morocco (Aircraft, 19 May 2006 – 5 Jun. 2006)	Short-range transported African dust	1769	1 – 2 μm	1.69	0.64 (0.61, 0.66)	
					6104	2 – 5 μm	1.55	0.67 (0.66, 0.68)	
					3747	5 – 10 μm	1.58	0.67 (0.66, 0.69)	
					654	10 – 32 μm	1.65	0.65 (0.62, 0.69)	
Lieke et al. (2011)	Data from Konrad Kandler	$\frac{L}{W_{ellipse}}$	Praia, south of Praia, and Dakar (Aircraft, 25 Jan., 4-5 Feb. 2008)	Short-range transported African dust	1579	0.4 – 1 μm	1.73	0.58 (0.56, 0.60)	
					6519	1 – 2 μm	1.70	0.54 (0.53, 0.55)	
					10064	2 – 5 μm	1.70	0.55 (0.54, 0.56)	
					2127	5 – 10 μm	1.76	0.56 (0.54, 0.57)	
					167	10 – 26 μm	1.84	0.67 (0.60, 0.75)	
Klaver et al. (2011) – Niger	Data from Paola Formenti	$\frac{L}{W_{ellipse}}$	Niger (Aircraft, 28 Jun. 2007)	Dust over African source region	1350	0.5 – 1 μm	1.63	0.80 (0.77, 0.84)	
						1 – 2 μm	1.88	0.82 (0.79, 0.86)	
						2 – 4 μm	1.88	0.89 (0.85, 0.92)	
						4 – 10 μm	1.88	0.87 (0.84, 0.90)	
Klaver et al. (2011) - Mali	Data from Paola Formenti	$\frac{L}{W_{ellipse}}$	Mali (Aircraft, 28 Jun. 2007)	Dust over African source region	1370	0.5 – 1 μm	1.63	0.86 (0.83, 0.90)	
						1 – 2 μm	1.63	0.86 (0.83, 0.90)	
						2 – 4 μm	1.63	0.81 (0.78, 0.84)	
						4 – 10 μm	1.63	0.87 (0.84, 0.90)	
Wagner et al. (2012) – Burkina Faso	Fig. 6	$\frac{L}{W_{ellipse}}$	Dano Burkina Faso (Sand samples)	Short-range transported African dust	257	0.1 – 1 μm	1.67	0.49	
Wagner et al. (2012) – Morocco	Fig. 6	$\frac{L}{W_{ellipse}}$	Draa valley and Lake Iriqui Morocco (Sand samples)	Short-range transported African dust	1927	0.1 – 1 μm	1.79	0.58	
Woodward et al. (2015) - ATD	Fig. 5	$\frac{L}{W_{ellipse}}$	Arizona Test Dust (Powder Technology, Inc.)	Artificial dust	269	0.2 – 7 μm	1.78	0.56 (0.52, 0.62)	
Woodward et al. (2015) - Kaolinite	Fig. 5	$\frac{L}{W_{ellipse}}$	Fluka (Powder Technology, Inc.)	Artificial dust	244	0.2 – 12 μm	1.78	0.67 (0.62, 0.74)	
Jeong et al. (2016)	Supplementary S1	$\frac{L}{W_{perp}}$	Izaña Tenerife (Ground-based, 15 Jul. 2005)	Short-range transported African dust	48	1.4 – 8.4 μm	1.30	1.65 (1.37, 2.07)	1.56 (0.08) 0.47 (0.39, 0.59)
Rocha-Lima et al. (2018) – Algeria	Fig. 9	$\frac{L}{W_{ellipse}}$	Bordj Badji Mokhtar, Algeria (Ground-based, 6-30 Jun. 2011)	Dust over African source region	2300	0.1 – 5 μm	1.43	0.96 (0.93, 0.99)	
Rocha-Lima et al. (2018) - Mauritania	Fig. 9	$\frac{L}{W_{ellipse}}$	Bir Moghrein, Mauritania (Ground-based, 23 May 2011 – 26 Jun. 2011)	Dust over African source region	2700	0.1 – 5 μm	1.48	0.92 (0.90, 0.95)	

Table 3.3: List of measurements of the height-to-width ratio (HWR) by individual particle analysis.

Study	Data source from the study in the first column	Published formula of HWR	Location (measurement techniques, time)	Attribution	Number of dust particles analyzed	Bin size range in terms of projected area-equivalent diameter	Values of HWR using formula in the second column		Corrected HWR, if formula in the third column is not $H/W_{ellipse}$	
							Median	Geo std (95% CI)	Median (SE)	Geo std (95% CI)
Okada et al. (2001) – Qira	Fig. 2	$\frac{H}{W_{perp}}$	Qira China (Ground-based, 21 Feb. 1991)	Dust over Asian source region	1900	0.2 – 12.2 μm	0.21	0.87 (0.84, 0.90)	0.25 (0.01)	0.87 (0.84, 0.90)
Okada et al. (2001) – Zhangye	Fig. 2	$\frac{H}{W_{perp}}$	Zhangye China (Ground-based, 27 Apr. to 7 May 1991)	Dust over Asian source region	3355	0.2 – 6.6 μm	0.26	0.96 (0.93, 0.98)	0.32 (0.02)	0.96 (0.93, 0.98)
Okada et al. (2001) - Hohhot	Fig. 2	$\frac{H}{W_{perp}}$	Hohhot China (Ground-based, 23 Apr. to 29 Apr. 1991)	Short-range transported Asian dust	1743	0.2 – 6.6 μm	0.46	0.78 (0.75, 0.80)	0.55 (0.03)	0.78 (0.75, 0.80)
Chou et al. (2008)	Fig. 8	$\frac{H}{W_{ellipse}}$	Niger (Aircraft, 10 Jan. 2006 – 3 Feb. 2006)	Dust over African source region	1	0.94 μm	0.34			
							1			
Sakai et al. (2010) - Asia	Data from Tetsu Sakai	$\frac{H}{W_{ellipse}}$	Huining China (Sand samples from Nishikawa et al., 2000)	Artificial dust	681	0.06 – 2 μm	0.40	0.63 (0.60, 0.67)		
Sakai et al. (2010) - Africa	Data from Tetsu Sakai	$\frac{H}{W_{ellipse}}$	Tessalit Mali (Sand samples, from Schutz and Seibert, 1987)	Artificial dust	1261	0.06 – 0.9 μm	0.45	0.61 (0.59, 0.64)		
Osada (2013)	Data from Kazuo Osada	$\frac{H}{\sqrt{L * W_{ellipse}}}$	Nagoya Japan (5 and 22 May 2010 and 2, 3, and 13 May 2011)	Long-range transported Asian dust	270	2 – 13.5 μm	0.21	0.43 (0.39, 0.47)	0.26 (0.01)	0.43 (0.39, 0.47)
Woodward et al. (2015) - ATD	Fig. 6	$\frac{H}{\sqrt{L * W_{ellipse}}}$	Arizona Test Dust (Powder Technology, Inc.)	Artificial dust	23	0.2 – 7 μm	0.16	0.76 (0.59, 1.08)	0.22	0.76 (0.59, 1.08)
Woodward et al. (2015) - Kaolinite	Fig. 6	$\frac{H}{\sqrt{L * W_{ellipse}}}$	Fluka (Powder Technology, Inc.)	Artificial dust	29	0.2 – 12 μm	0.17	0.75 (0.59, 1.01)	0.22	0.75 (0.59, 1.01)
Jeong et al. (2016)	Supplementary Table S1	$\frac{H}{W_{perp}}$	Izaña Tenerife (Ground-based, 15 Jul. 2005)	Short-range transported African dust	48	1.4 – 8.4 μm	0.50	0.63 (0.53, 0.79)	0.60 (0.03)	0.63 (0.53, 0.79)

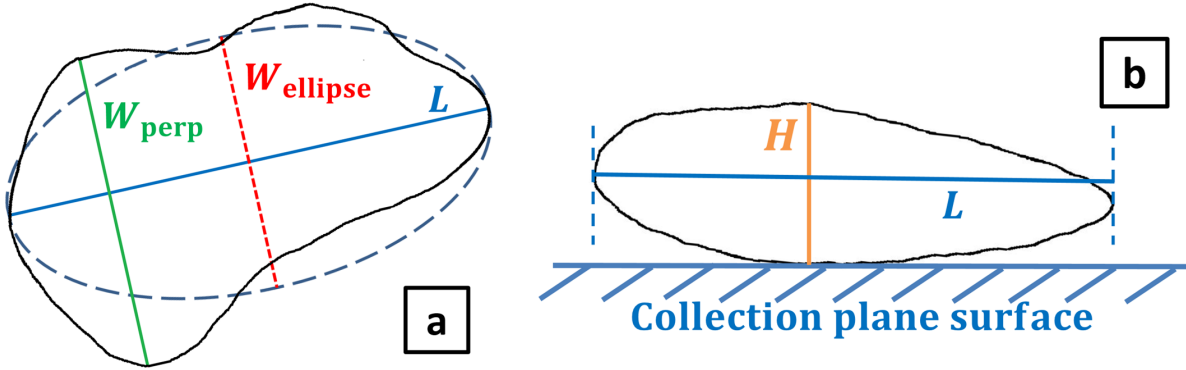


Figure 3.1: (a) Top view of two-dimensional (2-D) projected area (within the black line) of a dust particle and (b) side view, along the length L (blue line) defined in (a), of the same particle collected on a plane surface by impactors. Panel (a) demonstrates the systematic difference in the two common quantifications of dust width. The first definition records the maximum distance between two points on the outline that is perpendicular to the length L as the width W_{perp} (green line). The second definition records the width $W_{ellipse}$ (red dashed line) as the minor axis of an area-equivalent ellipse (blue dashed line) with L as its major axis. Because W_{perp} is systematically larger than $W_{ellipse}$ (Table 3.1), this systematic difference causes a systematic bias between experimental studies using different definitions of particle width. Panel (b) demonstrates the definition of dust height. The height H (orange line) is defined as the maximum distance between the outline of the particle to the collection surface that is perpendicular to the collection surface.

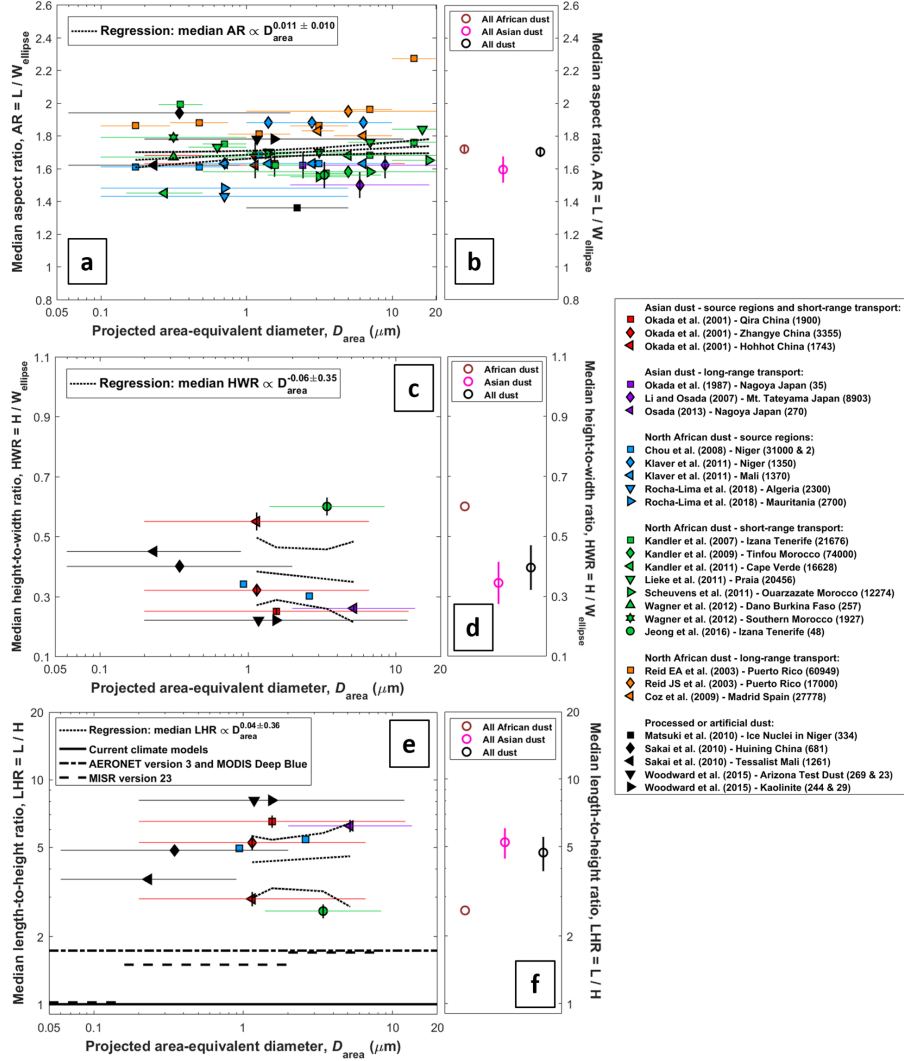


Figure 3.2: Measurement compilation of the medians of (a) the aspect ratio, (c) the height-to-width ratio, and (e) the length-to-height ratio as a function of projected area-equivalent diameter. The horizontal bars in (a), (c), and (e) show the bin ranges of the measurements, and the markers are plotted on the geometric means of the size ranges. The vertical bars in (a) and (c) denote errors from the uncertainty of the correction factor, and the vertical bars in (e) denote errors that propagate from (a) and (c). In the legend, the numbers in parentheses denote the numbers of analyzed individual dust particles. *Chou et al. (2008)* and *Woodward et al. (2015)* have two numbers with the first one denoting the number of analyzed dust particles for AR and the second one for HWR.

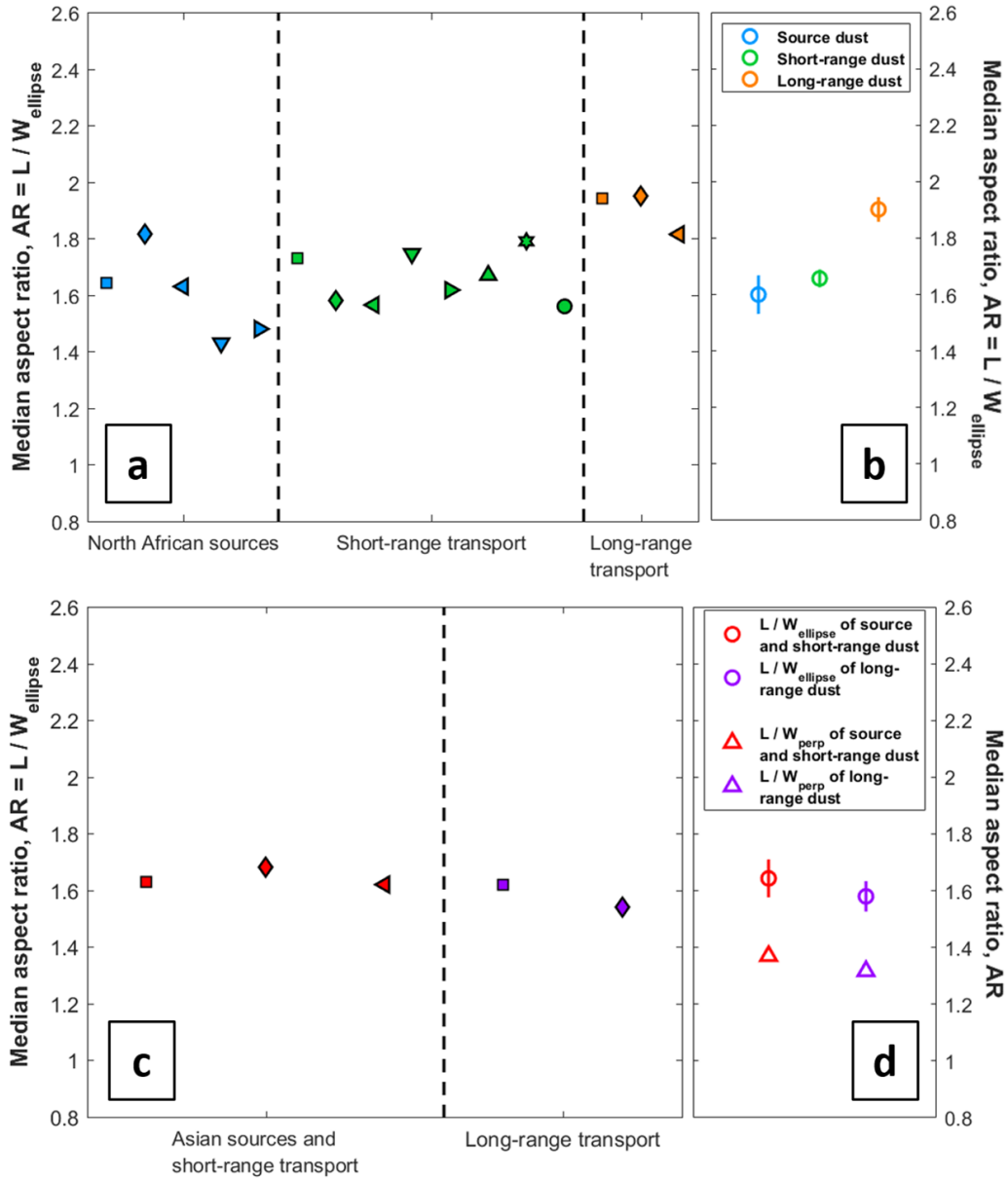


Figure 3.3: Changes during transport of the median aspect ratio of (a) North African dust and (c) Asian dust. The markers in (a) and (c) are defined in the legend of Figure 3.2. Results grouped by transport distance (see Figure 3.7) are shown in (b) and (d). In (d), median aspect ratios before ($\frac{L}{W_{perp}}$) and after ($\frac{L}{W_{ellipse}}$) the correction of the particle width are shown. This correction leads to a systematic change in all Asian dust studies and therefore does not affect the trend in shape during transport.

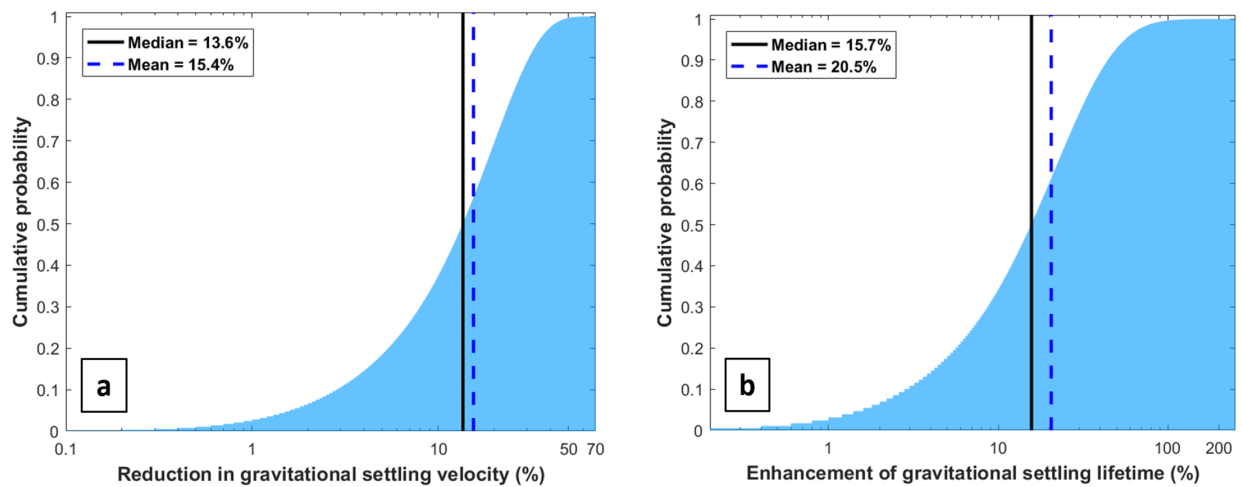


Figure 3.4: Probability distributions of (a) the reduction in gravitational settling velocity and (b) the enhancement of lifetime with respect to gravitational settling due to dust asphericity. Because deposition of dust with $D < 20\mu m$ occurs in the Stokes regime, the effect of asphericity on dust gravitational settling is independent of size.

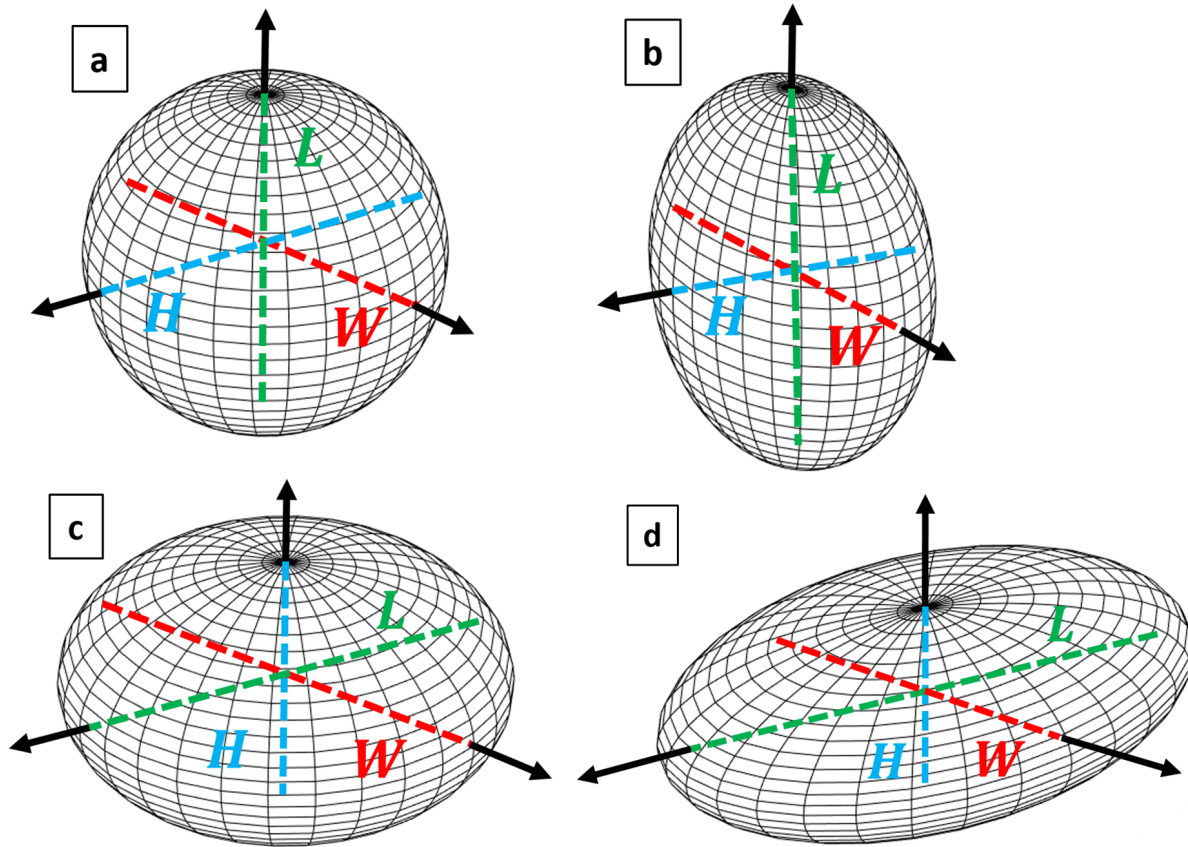


Figure 3.5: Three-dimensional view of a dust particle approximated as a (a) sphere, (b) prolate spheroid, (c) oblate spheroid, and (d) ellipsoid. In each plot, the three perpendicular axes are denoted. The largest, intermediate, and smallest axes are referred to as particle length L , width W , and height H , respectively. In shape (a) $L = W = H$, in shape (b) $L \geq W = H$, in shape (c) $L = W \geq H$, and in shape (d) $L \geq W \geq H$, such that shapes (a), (b) and (c) are simplified cases of shape (d).

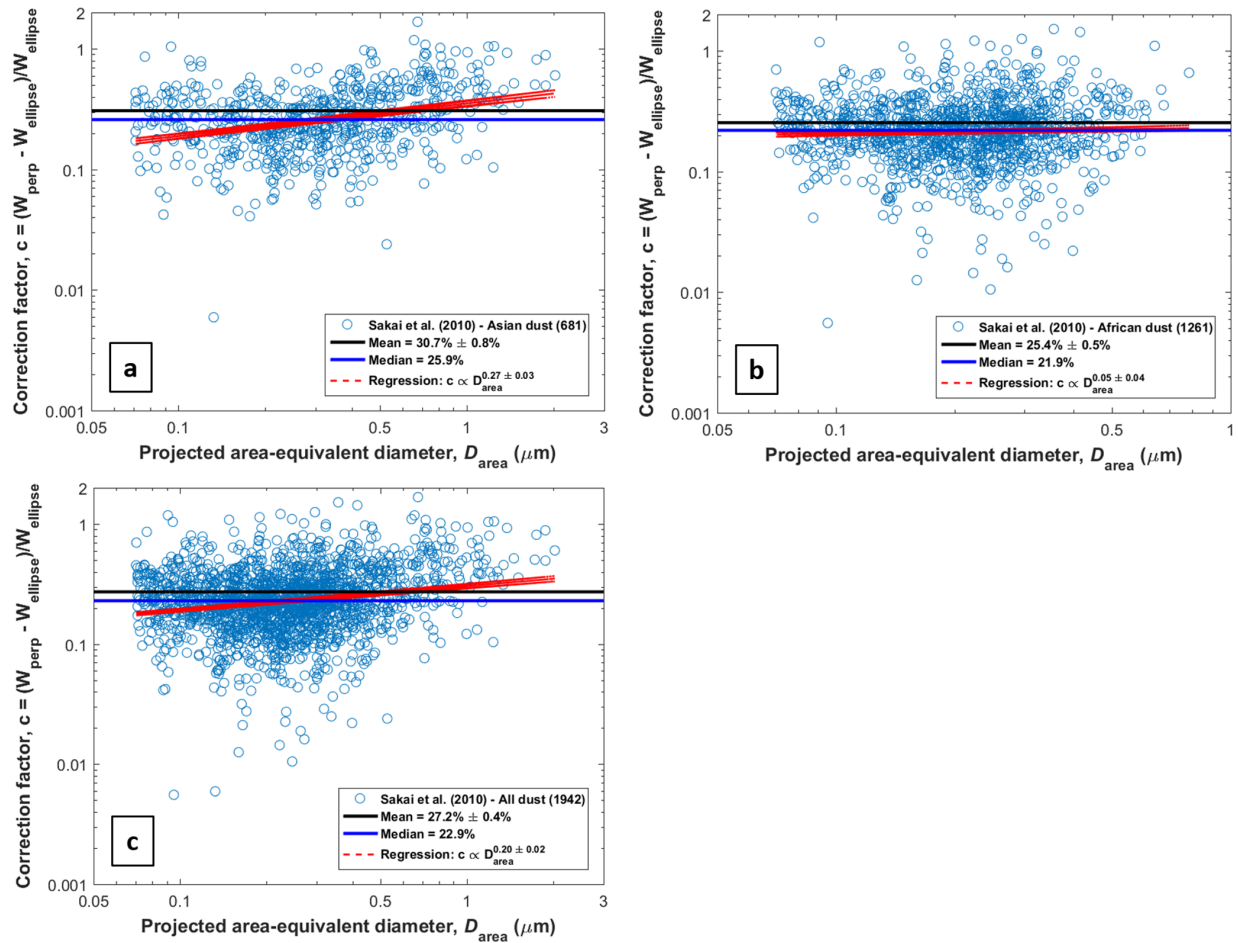


Figure 3.6: The correction factor between the two common definitions of particle width (see Fig. 3.1), shown as a function of projected area-equivalent diameter for (A) 681 Asian dust particles, (B) 1261 Saharan dust particles, and (c) 1942 dust particles in total.

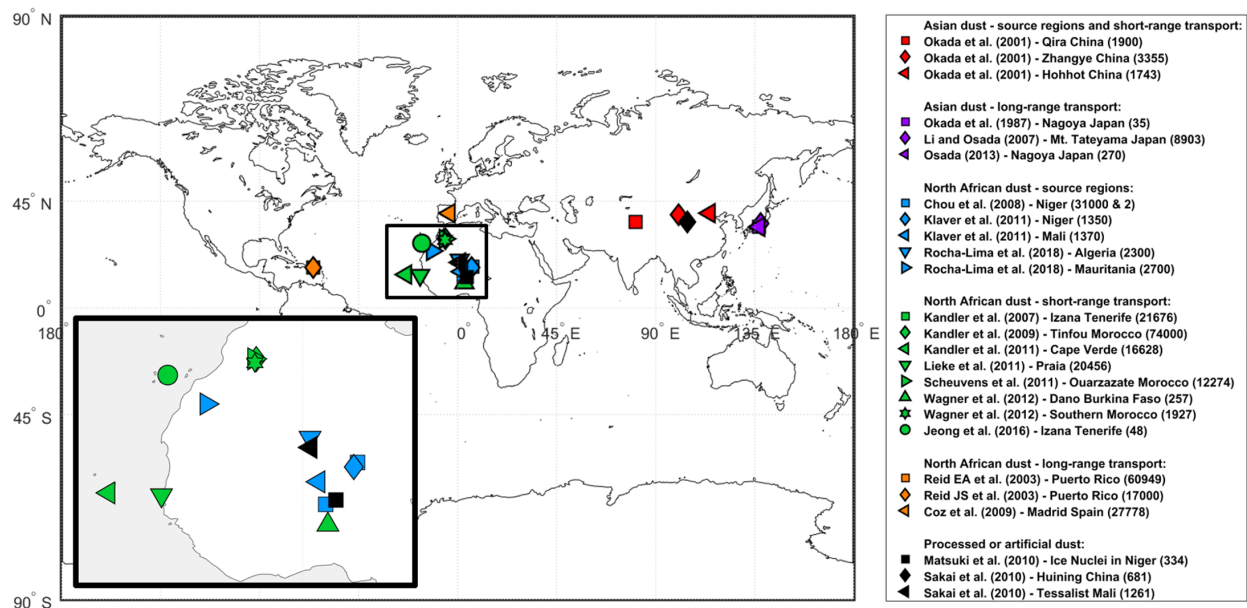


Figure 3.7: Locations of measurement sites for data used in this study. Measurements are grouped by source regions and transport distance, namely dust over Asian source regions and in short-range transport (in red markers), Asian long-range transported dust (in purple markers), dust over North African source regions (in blue markers), North African short-range transported dust (in green), and North African long-range transported dust (in orange markers). We determined whether dust was measured over Asian or North African source regions using the seasonally-resolved source regions obtained in *Ginoux et al.* (2012). We then distinguished long-range transported dust from short-range transported dust based on the attributions in publications that reported these measurements. The numbers in parentheses in the legend denote the number of analyzed individual dust particles. *Chou et al.* (2008) has two numbers with the first one denoting the number of analyzed dust particles for AR and the second one for HWR.

CHAPTER 4

Linking the different diameter types of aspherical desert dust indicates that models underestimate coarse dust emission

[**Huang, Y.**, A. A. Adebiyi, P. Formenti, and J. F. Kok (2021), Linking the different diameter types of aspherical desert dust indicates that models underestimate coarse dust emission, *Geophysical Research Letters*, 48(6), <https://doi.org/10.1029/2020GL092054>.]

Abstract

Measurements of dust aerosol size usually obtain the optical or projected area-equivalent diameters, whereas model calculations of dust impacts use the geometric or aerodynamic diameters. Accurate conversions between the four diameter types are thus critical. However, most current conversions assume dust is spherical, even though numerous studies show that dust is highly aspherical. Here, we obtain conversions between different diameter types that account for dust asphericity. Our conversions indicate that optical particle counters have underestimated dust geometric diameter (D_{geo}) at coarse sizes. We further use the diameter conversions to obtain a consistent observational constraint on the size distribution of emitted

dust. This observational constraint is coarser than parameterizations used in global aerosol models, which underestimate the mass of emitted dust within $10 \leq D_{geo} \leq 20\mu m$ by a factor of ~ 2 and usually do not account for the substantial dust emissions with $D_{geo} \geq 20\mu m$. Our findings suggest that models substantially underestimate coarse dust emission.

4.1 Introduction

Desert dust is a key atmospheric component that produces important effects on the Earth system, including by affecting the radiation budget (*Kok et al., 2021a,b; Pérez et al., 2006*), cloud microphysics (*DeMott et al., 2015*), atmospheric chemistry (*Tang et al., 2016*), and biogeochemical cycles (*Ito et al., 2019*). Furthermore, dust aerosols produce risks to human health (*Giannadaki et al., 2014; Huang et al., 2019*). These different dust effects are quantified using different types of diameters (*Mahowald et al., 2014*), but clear links between these different diameter types have not been established. This limits our ability to calculate and understand these various dust impacts, because these impacts depend sensitively on the size of dust aerosols. For example, the radiative effects of fine dust cool the Earth system, whereas coarse dust net warms the planet (*Kok et al., 2017*).

Four different types of diameters are used in studies of dust and its various impacts (Figure 4.1a). First, the volume-equivalent diameter (also called the geometric diameter), D_{geo} , is the diameter of a sphere that has the same volume and density as an irregularly shaped dust particle (*Hinds, 1999*). The geometric diameter can for instance be measured using a Coulter counter, which is a common technique for measuring dust size in ice and marine sediment cores (*Delmonte et al., 2002*). The geometric diameter is used in global aerosol models to quantify dust size (*Mahowald et al., 2014*). The size range with $D_{geo} \leq 20\mu m$ is considered most relevant to dust impacts on weather and climate (*Adebisi and Kok, 2020*), although coarser dust can also produce important impacts (*Ryder et al., 2013, 2019*). Second, the aerodynamic diameter, D_{aero} , is the diameter of a sphere with a density

close to water and with the same aerodynamic resistance as a dust particle (*Hinds*, 1999). The aerodynamic diameter is used in assessing aerosol impacts on human health and in setting air pollution standards (*Mahowald et al.*, 2014). The size ranges with $D_{aero} \leq 2.5\mu m$ and $D_{aero} \leq 10\mu m$ (often called $PM_{2.5}$ and PM_{10}) are most relevant to the respiratory risk of dust aerosols and are regulated worldwide. Third, the optical diameter, D_{opt} , is the diameter of a calibration particle, generally a polystyrene latex sphere or equivalent non-absorbing material, that produces the same scattered light intensity as the dust particle. The optical diameter is used in optical sizing instruments, such as the optical particle counters (OPCs), the sensors most widely used to measure the particle size distributions (PSDs) of dust aerosols in field campaigns (*Formenti et al.*, 2011). The fourth diameter type is the projected area-equivalent diameter, D_{area} , which is the diameter of a circle having the same area as the dust particle projected in a two-dimensional image, usually from scanning electron microscopy (*Kandler et al.*, 2007). The projected area-equivalent diameter is used to quantify size-resolved dust mineralogy and morphology (*Huang et al.*, 2020; *Kandler et al.*, 2011; *Swet et al.*, 2020) and occasionally dust PSDs (*Chou et al.*, 2008; *Ryder et al.*, 2018). These four types of diameters are used for different purposes. In particular, measurements usually determine dust aerosol size in terms of either the optical or projected area-equivalent diameters, whereas model calculations of dust impacts use the geometric or aerodynamic diameters. This makes it critical to reliably link the optical and projected area-equivalent diameters to the geometric and aerodynamic diameters.

Conversions between the four types of diameters generally assume dust is spherical. Specifically, the optical diameter is converted to the geometric diameter using Lorenz-Mie theory (*Rosenberg et al.*, 2012), the projected area-equivalent diameter is assumed equal to the geometric diameter (*Kandler et al.*, 2011), and the geometric diameter is converted to the aerodynamic diameter by using the aerodynamic drag law for spherical particles (*Hinds*, 1999). However, numerous in situ measurements show that dust is highly aspherical (e.g., *Kandler et al.* (2007)). Indeed, a recent study that compiled measurements of dust shape

worldwide concluded that the ratio of dust’s longest to shortest dimensions is ~ 5 on average (Huang *et al.*, 2020). Because aspherical dust has substantially different optical, geometric, and aerodynamic properties from spherical dust (Lindqvist *et al.*, 2014; Nousiainen and Kandler, 2015; Yang *et al.*, 2013), diameter conversions that assume a spherical shape are problematic. The resulting biases in size-resolved dust properties can propagate into the calculations of dust impacts on radiative transfer, biogeochemistry, and human health.

To address these problems in converting between different diameter types, here we obtain conversions between four common diameter types that account for dust asphericity (Section 4.2). In Section 4.3, we use these diameter conversions to harmonize observational studies that used different types of dust diameters; specifically, we obtain a consistent observational constraint on the size distribution of emitted dust in terms of geometric and aerodynamic diameters. This observational constraint is substantially coarser than parameterizations used in global aerosol models. This finding suggests an underestimation of coarse dust emission by models.

4.2 Linking the four diameters of aspherical dust

We first introduce the two shape descriptors that we use to quantify dust asphericity in Section 4.2.1. By using the two shape descriptors, we approximate dust as tri-axial ellipsoidal particles. We then use the shape-resolved optical, geometric, and aerodynamic properties of ellipsoidal dust to link the four types of diameters in Sections 4.2.2, 4.2.3, and 4.2.4, respectively.

4.2.1 Quantifying dust asphericity

We approximate dust as tri-axial ellipsoids whose asphericity is quantified by the ratio of the particle length L to the width W (the aspect ratio, AR) and the height-to-width ratio (HWR) ($L \geq W \geq H$; Figure 4.1a). Huang *et al.* (2020) compiled dozens of measurements

of AR ($= \frac{L}{W}$) and HWR ($= \frac{H}{W}$) worldwide. They found that both AR and HWR deviate substantially from unity, and thus that the ellipsoidal approximation of dust shape is more realistic than spherical or spheroidal approximations. In addition, *Huang et al.* (2020) found that both shape descriptors show little dependence on dust size, that AR and HWR are not correlated, and that both HWR and the deviation of AR from unity (AR-1) follow lognormal distributions (see Section 3.2.1 and Equations (3.1) and (3.2)). Although *Huang et al.* (2020) found modest differences in shape distributions for different regions (Table 4.1), sensitivity tests indicate that these regional differences in dust shape distributions produce only minor differences in diameter conversions (Figure 4.4). In the present study, we thus take the medians of AR and HWR as 1.70 ± 0.03 and 0.40 ± 0.07 , respectively, and the geometric standard deviations of AR-1 and HWR respectively as 0.70 ± 0.02 and 0.73 ± 0.09 , after the globally averaged distributions of AR and HWR (*Huang et al.*, 2020).

4.2.2 Linking the optical and geometric diameters

The geometric diameter is required in models to calculate dust impacts, whereas most measurements size dust in terms of the optical diameter by using optical particle counters (OPCs) (*Formenti et al.*, 2011). OPCs determine the size and abundance of aerosols by passing a light beam through an aerosol sample and measuring the scattered light intensity by individual aerosol particles (see top-left box in Figure 4.1a). OPC manufacturers calibrate their instruments generally against polystyrene latex spheres (PSLs; *ISO* (2009)), or occasionally equivalent non-absorbing spheres (*Rosenberg et al.*, 2014); by default, OPCs categorize aerosol samples into size bins in terms of the optical diameter of PSLs. This default relationship between measured scattered intensities and optical diameters of spherical PSLs is problematic for particles that are not PSLs, such as dust particles. In this section, we link the optical diameter of spherical PSLs to the geometric diameter of ellipsoidal dust that would generate the same scattered intensity as measured by OPCs.

The scattered intensity produced by an aerosol particle measured by an OPC within the

scattering angle range from θ_1 to θ_2 (Figure 4.2f, inset) is (Liou, 2002)

$$I_{OPC} = \frac{I_i}{4\pi} \times C_{sca} \times \int_0^{2\pi} \int_{\theta_1}^{\theta_2} P(\theta) \sin(\theta) d\theta d\phi \quad (4.1)$$

where I_i (W/m^2) is the incident light intensity that is a constant for a given OPC model, C_{sca} (m^2) is the scattering cross section, $P(\theta)$ (unitless) is the phase function quantifying the angular distribution of the scattered intensity, and ϕ (sr) is the azimuth angle (Liou, 2002). Since most OPCs use a concave mirror to direct and detect scattered light, the scattered intensity measured by most OPCs does not depend on ϕ . For simplicity, we express the normalized scattered intensity measured by OPCs as

$$SI = \frac{I_{OPC}}{I_i} = \frac{1}{2} \times Q_{sca} \times A \times \int_{\theta_1}^{\theta_2} P(\theta) \sin(\theta) d\theta \quad (4.2)$$

where $C_{sca} = Q_{sca} \times A$ and Q_{sca} (unitless) is the scattering efficiency that quantifies a particle's ability to scatter relative to its physical cross-sectional area, A (m^2) (Liou, 2002). We use Equation (4.2) to calculate the scattered intensity as a function of the optical diameter of spherical PSLs, and to calculate the scattered intensity of ellipsoidal dust with a wide range of sizes and shape descriptors. For each optical diameter of spherical PSLs, we then determine the average geometric diameter of ellipsoidal dust that produces the same scattered intensity. We discuss these steps in more detail below.

The scattered intensity is sensitive to particle shape. Since PSLs are spherical, we obtained their single-scattering properties, including Q_{sca} and $P(\theta)$, from Lorenz-Mie theory (Liou, 2002). However, since Lorenz-Mie theory is invalid for aspherical particles, we instead obtained Q_{sca} and $P(\theta)$ of aspherical dust approximated as ellipsoids by using the single-scattering database of Meng *et al.* (2010). This database combines four computational methods (Lorenz-Mie theory, T-matrix method, discrete dipole approximation, and an improved geometric optics method) to compute the single-scattering properties of ellipsoidal dust for a wide range of AR, HWR, size parameter, and refractive index. Specifically, we first used Monte-Carlo sampling to randomly generate a large number (10^8) of volume-equivalent ellipsoidal dust from the two lognormal distributions of AR and HWR (Section

4.2.1). Second, by assuming that each generated particle is randomly oriented, we calculated its A and used the *Meng et al.* (2010) database to obtain its Q_{sca} and $P(\theta)$. Finally, we averaged these values and obtained ensemble-averaged values of A , Q_{sca} , and $P(\theta)$ that account for dust asphericity.

Besides particle shape, the scattered intensity also depends on dust refractive index, the wavelength of the light beam used in the OPC, and the scattering angle range of the OPC's light sensor. OPCs usually measure sideward-scattered intensity within a wide range of scattering angles (e.g., $90^\circ \pm 60^\circ$) and use visible wavelengths (summarized in Table 4.2). At these wavelengths, PSLs have a well-calibrated refractive index of $1.59 - 0i$ (*ISO*, 2009), whereas the dust refractive index has a large uncertainty (*Di Biagio et al.*, 2017, 2019; *Sokolik and Toon*, 1999). We used six real parts of dust refractive index between 1.45 and 1.59 and eight imaginary parts between 0.0005 and 0.01 (covering the ranges of *Kok et al.* (2017); *Di Biagio et al.* (2019)). We provided a look-up table that contains the dust refractive index-, wavelength-, and scattering angle range-resolved conversions between the optical diameters of spherical PSLs and the geometric diameters of ellipsoidal dust.

This look-up table is available in a publicly-accessible repository (<http://doi.org/10.5281/zenodo.4317642>). It contains the following variables:

1. seven wavelengths (440, 550, 590, 630, 660, 780, and 880 nm) and five scattering angle ranges ($90^\circ \pm 60^\circ$, $90^\circ \pm 40^\circ$, $90^\circ \pm 5^\circ$, $60^\circ \pm 40^\circ$, and $8^\circ \pm 4^\circ$) after the OPC models used in the measurements of emitted dust aerosols (Table 4.2; *Fratini et al.* (2007); *Sow et al.* (2009); *Shao et al.* (2011a); *Rosenberg et al.* (2014); *Huang et al.* (2019); *Khalfallah et al.* (2020));
2. geometric diameter ranging from 0.1 μm to 50 μm ;
3. only one shape and one refractive index of PSLs, since spherical PSLs have a refractive index of $1.59 - 0i$ at the seven wavelengths, well-calibrated under the international standard *ISO* (2009);

4. six real parts (1.45, 1.50, 1.52, 1.53, 1.56, and 1.59) and eight imaginary parts (0.0005, 0.001, 0.002, 0.003, 0.004, 0.005, 0.006, and 0.01) of the dust refractive index covering the ranges in *Kok et al. (2017)*; *Di Biagio et al. (2019)*;

5. dust shape quantified by the globally-averaged lognormal distributions of AR and HWR (Equations (3.1) and (3.2) in *Huang et al. (2020)*). Note that the *Meng et al. (2010)* database cannot simulate optics with HWR less than 0.31. For dust with HWR less than 0.31, we take its single-scattering properties as the single-scattering properties of dust with the same geometric diameter, but with HWR= 0.31.

We find that OPCs underestimate dust diameter at coarse sizes, due to the combined effects of dust refractive index and dust asphericity. The difference in refractive index between PSLs and dust particles causes the optical diameter to underestimate the size of spherical dust at almost all sizes (blue lines, Figure 4.1b), but this underestimation due to refractive index difference is offset by dust asphericity (red lines, Figure 4.1b). We first isolated the effect of dust refractive index by comparing the optical diameter of PSLs with the geometric diameter of spherical dust particles (blue lines, Figure 4.1b). We find that PSLs produce a larger sideward-scattered intensity than spherical dust particles with the same diameter (black and blue lines, Figure 4.2a). This occurs because PSLs have a larger real and smaller imaginary refractive index than dust. Thus, a spherical dust with a larger size than a PSL produces the same amount of sideward-scattered intensity as measured by OPCs. Second, we isolated the effect of dust asphericity by comparing the spherical and ellipsoidal dust with the same refractive index (i.e., blue and red dotted lines, Figure 4.1b). We find that ellipsoidal dust has a larger sideward-scattered intensity than volume-equivalent spherical dust (red and blue lines, Figure 4.2a). This occurs because ellipsoidal dust has a larger total scattering efficiency (Figure 4.2b) but a smaller fraction of that total scattering occurs at angles that OPCs measure (Figure 4.2c). Thus, the size of an ellipsoidal dust that produces the same amount of sideward-scattered intensity as a PSL is smaller than the size of a spherical dust that produces this intensity (Figure 4.1b). Finally, after combining the effects of dust

refractive index and dust asphericity, we find that OPCs that use optical diameter by default underestimate dust geometric diameter at coarse sizes (red lines, Figure 4.1b). The diameter at which OPCs start to underestimate dust size decreases substantially with increasing dust imaginary refractive index (red lines, Figure 4.1b). When the imaginary part increases from 0.0005 to 0.002 and 0.006, the intersection between the red lines and the 1:1 reference line decreases from ~ 23 to ~ 8 , and $\sim 3 \mu m$ in optical diameter. This finding highlights the importance of determining dust imaginary refractive index during in situ measurements to precisely calibrate OPC’s size bins and reduce errors in the measured size-resolved data set.

4.2.3 Linking the projected area-equivalent and geometric diameters

After linking the optical and geometric diameters (Section 4.2.2), we next focus on the projected area-equivalent diameter, which is also commonly used as a measure of dust size (Chou *et al.*, 2008; Gillette *et al.*, 1972). The projected area-equivalent diameter, D_{area} , is obtained from a two-dimensional ($2-D$) projection image of a $3-D$ irregularly shaped dust particle with a volume-equivalent diameter of D_{geo} (Figure 4.1a). Most studies used $2-D$ optical or scanning electron microscopic images of individual dust particles obtained after these particles were collected on filters by ground-based or aircraft-carried impactors (Gillette *et al.*, 1972; Kandler *et al.*, 2007). These impactor-collected dust particles tend to deposit with their largest surface lying parallel to the collection surface, which corresponds to the particle’s smallest dimension being oriented perpendicular to the collection surface (Figure 4.1a). Indeed, Okada *et al.* (2001) and Sakai *et al.* (2010) respectively found that about 97% and 95% of dust particles deposited in this manner. Since the smallest dimension (the height H) is on average five times smaller than the largest dimension (the length L) and three times smaller than the intermediate dimension (the width W) (Huang *et al.*, 2020), the projected area-equivalent diameter substantially overestimates the geometric diameter. To quantify this effect, we assume for simplicity that all dust particles deposit in this orientation, such that the projected area-equivalent diameter equals $D_{area} = \sqrt{L \times W}$. We thus express the

ratio of the projected area-equivalent and geometric diameters as a function of AR ($= \frac{L}{W}$) and HWR ($= \frac{H}{W}$) as

$$\frac{D_{area}}{D_{geo}} = \frac{\sqrt{LW}}{\sqrt[3]{LWH}} = \frac{\sqrt[6]{AR}}{\sqrt[3]{HWR}}. \quad (4.3)$$

We used the globally averaged shape distributions of AR and HWR to obtain the probability distribution of $\frac{D_{area}}{D_{geo}}$ (Figure 4.1c). Specifically, we used Monte-Carlo sampling to randomly generate a large number of dust particles from the two lognormal distributions of AR and HWR. Then, for each generated particle, we used Equation (4.3) to obtain $\frac{D_{area}}{D_{geo}}$. We found that the projected area-equivalent diameter is on average $56.3\% \pm 0.8\%$ larger than the geometric diameter (Figure 4.1c). This indicates that studies that used projected area-equivalent diameter to quantify dust size have substantially overestimated dust size (e.g., *Chou et al. (2008)*; *Gillette et al. (1972)*).

4.2.4 Linking the geometric and aerodynamic diameters

After linking the optical, projected area-equivalent, and geometric diameters (Sections 4.2.2 and 4.2.3), we next focus on the aerodynamic diameter which is used in assessing dust impacts on human health (*Hinds, 1999*). The aerodynamic diameter, D_{aero} , is the diameter of a sphere with a density close to water that has the same gravitational settling velocity as the aspherical dust with a geometric diameter of D_{geo} (*Hinds, 1999*). Gravitational settling of dust aerosols occurs in the Stokes regime as the Reynolds number is far less than one (*Kok et al., 2012*). In the Stokes regime, the gravitational settling velocity of a spherical particle is (*Hinds, 1999*)

$$V_{sph} = \frac{g}{18 \times \mu} \times \rho \times D^2 \quad (4.4)$$

where g is the gravitational acceleration, ρ is the particle density, $\mu \approx 1.81 \times 10^{-5} Pa \times s$ is the dynamic viscosity of air, and D is the diameter of the spherical particle. For an aspherical particle, we express its gravitational settling velocity as (*Hinds, 1999*)

$$V_{asp} = \frac{1}{\chi} \times \frac{g}{18 \times \mu} \times \rho \times D_{geo}^2 \quad (4.5)$$

where χ is the dynamic shape factor that is the ratio of the aerodynamic resistance exerted on an aspherical particle to the resistance on a spherical particle with equal volume and density (*Hinds, 1999*). By equating the gravitational settling velocities in Equations (4.4) and (4.5), we link the aerodynamic and geometric diameters as

$$D_{aero} = D_{geo} \times \sqrt{\frac{\rho_d}{\chi \times \rho_0}} \quad (4.6)$$

where $\rho_d \approx 2.5 \times 10^3 \text{ kg/m}^3$ is the typical density of dust aerosols (*Kok et al., 2017*) and $\rho_0 = 1.0 \times 10^3 \text{ kg/m}^3$ is the density of water. For aspherical dust approximated as ellipsoids, $\chi = \frac{1}{2} \times \left(F_s^{\frac{1}{3}} + \frac{1}{F_s^{\frac{1}{3}}} \right)$ and (*Bagheri and Bonadonna, 2016; Huang et al., 2020*).

We used the globally averaged shape distributions of AR and HWR to obtain the probability distribution of $\frac{D_{aero}}{D_{geo}}$ (Figure 4.1d). Specifically, we used Monte-Carlo sampling to randomly generate a large number of dust particles from the two lognormal distributions of AR and HWR. Then, for each generated particle, we used Equation (4.6) to obtain $\frac{D_{aero}}{D_{geo}}$. We found that the aerodynamic diameter is on average $44.9\% \pm 0.3\%$ larger than the geometric diameter (Figure 4.1d). This result is partially due to dust having a greater density than water, and partially due to dust asphericity increasing the drag force relative to a volume-equivalent sphere.

4.3 Harmonizing size distributions of emitted dust

After linking the four diameters of aspherical dust (Section 4.2), we next use these diameter conversions to harmonize observational studies that sized dust using different diameter types. Eight studies have measured the PSDs of emitted dust in terms of either optical or projected area-equivalent diameters. Three of these studies quantified dust size in terms of projected area-equivalent diameter (Figure 4.3a; *Gillette et al. (1972, 1974); Gillette (1974)*); they used microscopy to determine the number fluxes of emitted dust from five distinct soils during 29 wind events (summarized in Table S1 of *Kok (2011a)*). The other five studies used optical diameter (Figure 4.3a; *Fratini et al. (2007); Sow et al. (2009); Shao et al.*

(2011a); *Rosenberg et al.* (2014); *Khalfallah et al.* (2020)); they used different OPC models to determine the number fluxes of emitted dust from five distinct regions during 24 wind events (Table 4.2). Since *Gillette* (1974) did measurements at three distinct soils, these eight studies yield a total of 10 data sets. These data sets have been used to parameterize the PSD of emitted dust in many modeling studies, thereby implicitly assuming that these different PSDs are in terms of geometric diameter. This includes the study of *Kok* (2011a), who derived a parameterization of the emitted dust PSD from the analogy of dust emission with the fragmentation of brittle materials such as glass spheres. This “brittle fragmentation theory (BFT)” yielded a relatively simple parameterization that was in good agreement with the (unharmonized) measurements of emitted dust PSDs available at the time. One key prediction of BFT parameterization was that atmospheric dust is substantially coarser than global aerosol models accounted for at the time, which has been supported by a number of subsequent experimental and modeling studies (e.g., *Adebisi and Kok* (2020); *Rosenberg et al.* (2014)). The BFT parameterization has been implemented in a large number of global aerosol models (e.g., *Nabat et al.* (2012); *Mahowald et al.* (2014); *Klose et al.* (2021)).

We harmonized observational data sets of emitted dust PSDs in order to better inform model parameterizations. We did so by converting the 10 PSDs from either optical or projected area-equivalent diameters to geometric and aerodynamic diameters. First, for the five microscopy data sets, we converted projected area-equivalent diameters to geometric diameters by dividing by the mean of $\frac{D_{area}}{D_{geo}}$ (Figure 4.1c). For the five OPC data sets, we converted optical diameters to geometric diameters by combining OPC parameters (Table 4.2) with the look-up table (Section 4.2.2). Second, we normalized each PSD data set following *Kok* (2011a), such that each number PSD of emitted dust follows a power law with exponent of one in the range of $2 \leq D_{area} \leq 10\mu m$ (corresponding to $1.28 \leq D_{geo} \leq 6.41\mu m$; Figure 4.1c). Third, we averaged the volume PSDs of various wind events at a given soil because wind speed has no statistically significant effect on the emitted dust PSD (*Kok*, 2011b), although a recent study has challenged this finding (*Shao et al.*, 2020). Fourth, we

normalized each volume PSD such that its integration over $0 \leq D_{geo} \leq 20\mu m$ yields one. Fifth, we obtained the maximum likelihood estimate (MLE) of the harmonized emitted dust PSD following (Kok *et al.*, 2017). Specifically, we fit each volume PSD with the analytical function derived from brittle fragmentation theory, and then combined these 10 analytical functions in a statistical model to obtain the MLE and its 95% confidence interval. Finally, we followed a similar procedure to obtain PSDs in terms of aerodynamic diameter. The above procedure yields a consistent data set of emitted dust PSDs in terms of geometric diameter (bottom x-axis, Figure 4.3b) and aerodynamic diameter (top x-axis, Figure 4.3b).

We obtained two key findings from the harmonized emitted dust PSDs and the MLE fit, which can be taken as the globally representative PSD of emitted dust (see discussion in Kok *et al.* (2017)). First, the harmonization reduces the divergence in emitted dust PSDs at coarse sizes (from a factor of ~ 15 to a factor of ~ 2 at diameters larger than $\sim 12\mu m$; Figures 4.3a and 4.3b). This occurs because, at coarse sizes, OPC studies underestimated geometric diameter (Figure 4.1b) and thus their PSDs shifted rightward after the harmonization, whereas microscopy studies overestimated geometric diameter (Figure 4.1c) and thus shifted leftward. The second key finding is that the original BFT parameterization (Kok, 2011a) substantially underestimates the emission of super-coarse dust ($D_{geo} \geq 10\mu m$), namely by a factor of ~ 2 in the $10 \leq D_{geo} \leq 20\mu m$ size range (Figure 4.3c). Furthermore, this parameterization has a cutoff diameter at $20\mu m$, whereas measurements show a substantial amount of emitted dust with $D_{geo} \geq 20\mu m$ (Figure 4.3c). Since the original BFT parameterization is substantially coarser than other parameterizations of the emitted dust PSD (Mahowald *et al.*, 2014), our findings indicate that global aerosol models have substantially underestimated the emission of super-coarse dust.

Our findings have several implications. First, the underestimation of super-coarse dust emission helps explain why models underestimate the concentration of super-coarse dust ($D_{geo} \geq 10\mu m$) in the atmosphere. Recent measurements have shown that super-coarse dust is substantially more abundant in the atmosphere than models account for (Adebiji

and Kok, 2020; Ryder et al., 2018; van der Does et al., 2018). This model underestimation of super-coarse dust in the air could be due to a number of physical processes omitted or inadequately represented by models, including the slowing of gravitational settling of super-coarse dust by dust asphericity (Huang et al., 2020), turbulent vertical mixing in dust layers (Gasteiger et al., 2017), electrostatic charging of dust (Harrison et al., 2018), the possible increase in vertical transport of coarse dust by topography-enhanced boundary layer turbulence (Chamecki et al., 2020), and inaccurate representations of wet deposition processes (van der Does et al., 2020; Yu et al., 2019). Our results indicate that models also underestimate super-coarse dust because of a substantial underestimation of super-coarse dust emission.

Second, our results imply a substantial emission (and thus deposition) flux of dust with diameter in excess of $20 \mu\text{m}$, which is not accounted for in most models. Our results are consistent with recent measurements finding a substantial amount of dust in the atmosphere with diameters larger than $20 \mu\text{m}$ (Ryder et al., 2018; van der Does et al., 2018). However, almost all large-scale models simulate the dust cycle with a cutoff diameter less than $20 \mu\text{m}$ (Huneeus et al., 2011; Wu et al., 2020). This super-coarse dust produces a net warming (Di Biagio et al., 2020; Ito et al., 2021) and carries more nutrients than fine dust (Marricotte et al., 2020). These important effects of super-coarse dust on weather, climate, and biogeochemistry, especially near source regions, are not accounted for by most models.

Finally, our results suggest that inconsistencies in diameter types used in measurements versus modeling studies have resulted in substantial biases. Studies commonly ignore the difference between diameter types, implicitly assuming that different diameter types are equivalent. We have shown here that this assumption results in substantial errors that propagate into inaccurate estimates of dust impacts. For future studies, we therefore recommend adopting the standardized size conversions obtained here. For published studies, we recommend carefully re-examining, diagnosing, and harmonizing the obtained size-resolved data sets.

4.4 Conclusions

Measurements of dust aerosol size usually obtain the optical or projected area-equivalent diameters, whereas model calculations of dust impacts use the geometric or aerodynamic diameters. Accurate conversions between the four diameter types are thus critical. However, this critical step of converting between diameter types has been overlooked in many previous studies, for instance in parameterizations of emitted dust size distribution. Furthermore, most existing diameter conversions assume dust is spherical, which is problematic as dust aerosols are highly aspherical.

Here, we address these problems by developing conversions between four diameter types that account for dust asphericity. We found that (1) optical particle counters underestimate dust geometric diameter at $D_{opt} \geq \sim 8\mu m$, (2) microscopy measurements using the projected area-equivalent diameter overestimate dust geometric diameter by $\sim 56\%$, and (3) the aerodynamic diameter exceeds dust geometric diameter by $\sim 45\%$. We encourage the dust research community to use these conversions to more accurately link different diameter types used in observational and modeling studies.

We used these diameter conversions to obtain a consistent observational constraint on the size distribution of emitted dust. This observational constraint is substantially coarser than parameterizations used in global aerosol models, which underestimate the mass of emitted dust within $10 \leq D_{geo} \leq 20\mu m$ by a factor of ~ 2 . This finding helps explain why global aerosol models underestimate the abundance of super-coarse dust with $D_{geo} \geq 10\mu m$ in the atmosphere relative to measurements. Furthermore, our results imply a substantial dust emission and deposition flux with $D_{geo} \geq 20\mu m$, which is not accounted for in most models. These models thus neglect the important effects of super-coarse dust on weather, climate, and biogeochemistry, especially near source regions.

Acknowledgements. The authors thank the two anonymous reviewers for their comments that helped to improve the manuscript. Y. Huang acknowledges the financial support by the National Aeronautics and Space Administration (NASA) grant 80NSSC19K1346, awarded under the Future Investigators in NASA Earth and Space Science and Technology (FINESST) program. J. F. Kok acknowledges the support by the National Science Foundation (NSF) grants 1552519 and 1856389, and the Army Research Office under Cooperative Agreement Number W911NF-20-2-0150. A. A. Adebisi acknowledges the support by University of California President’s Postdoctoral Fellowship. P. Formenti acknowledges support by the project DustClim, part of ERA4CS, an ERA-NET initiated by JPI Climate, and funded by FORMAS (SE), DLR (DE), BMFW (AT), IFD (DK), MINECO (ES), ANR (FR) with co-funding by the European Union (grant 690462). The views and conclusions contained in this manuscript are those of the authors and should not be interpreted as representing the official policies, either expressed or implied, of the Army Research Office or the US Government. The US Government is authorized to reproduce and distribute reprints for Government purposes notwithstanding any copyright notation herein. The authors thank Claudia Di Biagio for providing comments that helped improve the manuscript. In addition, the authors thank Philip Rosenberg and Bouthaina Khalfallah for providing experimental data and thank Carlos Pérez García-Pando, Natalie Mahowald, Konrad Kandler, Yoshihide Takano, Masahide Ishizuka, and Bingqi Yi for insightful discussions. Furthermore, the authors thank Mike Putnam at the Met One Instruments Inc., Randy Grater at the Climec Instruments Co., and Friedhelm Schneider at the GRIMM Aerosol Technik Ainring GmbH Co. KG for providing information on OPC parameters.

4.5 Tables and figures

Table 4.1: The median and the geometric standard deviation (GSD) of the two lognormally-distributed shape descriptors (the aspect ratio, AR, and the height-to-width ratio, HWR) of ellipsoidal dust for different regions. Values are taken after *Huang et al.* (2020), who compiled 25 datasets of AR and HWR across the world (6 for Asian dust, 16 for North African dust, and 3 for artificial dust).

	Asian source dust	Asian long-range transported dust	North African source dust	North African long-range transported dust	Global averages (used in the main text)
Median of AR	1.64	1.58	1.60	1.90	1.70
GSD of AR-1	0.56	0.47	0.91	0.70	0.70
Median of HWR	0.37	0.26	0.60*	0.60*	0.40
GSD of HWR	0.87	0.43	0.63*	0.63*	0.73

* Note that only one study has measured HWR of North African dust, therefore values of North African source dust are taken as the same as that of North African long-range transported dust.

Table 4.2: Parameters of the five studies that used optical particle counters (OPCs) to measure the particle size distributions (PSDs) of emitted dust.

		Fratini et al. (2007)	Sow et al. (2009)	Shao et al. (2011)	Rosenberg et al. (2014)		Khalfallah et al. (2020)
Measurement site		Gobi Desert, China (41.88° N, 100.54° E)	Banizoumbou, Niger (13.52° N, 2.63° E)	Australia (33.85° S, 142.74° E)	Western Sahara (22°N to 28°N, 4°W to 14°W)		Dar Dhaoui, Tunisia (33.30° N, 10.78° E)
Number of measurements (data source in parentheses)		3 (Fig. 10a)	3 (Fig. 9)	7 (Fig. 12)	3 (Fig. 5b; personal communication with Philip Rosenberg, 2015)		8 (Fig. 5)
OPC-related parameters	Manufacturer (model type)	Climet (CI-3100)	GRIMM (Model 1.108)	YGK Corp. (ADS-03-8CH)	DMT (PCASP 100-X)	DMT (CDP)	PALAS (Welas 2300)
	Wavelength, nm	780	780	780	632.8	658	440*
	Scattering angle range, deg	90±90	90±60.5	60±39.2	90±55	4–12	90±5*
	Nominal boundary diameters, µm	0.26–0.30–0.34–0.42–0.44–0.50–0.54–0.74–0.76–0.94–0.95–1.65–1.85–2.7–3–4–5–6–7	0.3–0.4–0.5–0.65–0.8–1–1.6–2–3–4–5–7.5–10–15–20	0.3–0.5–0.7–1–2–3–5–7	0.1–3	3–50	0.32–0.42–0.56–0.75–1.00–1.33–1.78–2.37–3.16–4.22–5.62–7.50–10.00
	Refractive index used in calibration (calibration particle type)	1.59–0i (PSL)	1.59–0i (PSL)	1.59–0i (PSL)	1.59–0i (PSL)	1.59–0i (Glass bead sphere)	1.59–0i (PSL)
Parameters used in published studies	Dust refractive index	1.59–0i	1.59–0i	1.5–0.001i	1.53–0.001i	1.53–0.001i	1.59–0i
	Dust shape assumption	Sphere	Sphere	Three-axis oval	Sphere	Sphere	Sphere
	Published boundary diameters, µm	0.26–0.30–0.34–0.42–0.44–0.50–0.54–0.74–0.76–0.94–0.95–1.65–1.85–2.7–3–4–5–6–7	0.3–0.4–0.5–0.65–0.8–1–1.6–2–3–4–5–7.5–10–15–20	0.3–0.6–0.9–1.4–2–3.5–5.9–8.4	0.48–0.62–0.76–0.95–1.19–1.52–1.85–2.06–2.25–2.46–2.69–2.91–3.17–3.94	3.94–5.98–9.45–13.99–22.56–36.96–51.96	0.32–0.42–0.56–0.75–1.00–1.33–1.78–2.37–3.16–4.22–5.62–7.50–10.00
Parameters used in this study	Dust refractive index	1.48–0.0012i	1.51–0.0029i	1.54–0.0013i	1.53–0.0001i	1.53–0.0001i	1.51–0.0038i
	Source of dust refractive index	Di Biagio et al. (2019) - Gobi	Di Biagio et al. (2019) - Niger	Di Biagio et al. (2019) - Australia	Ryder et al. (2013) - Fennec	Ryder et al. (2013) - Fennec	Di Biagio et al. (2019) - Tunisia
	Dust shape assumption	Tri-axial ellipsoid	Tri-axial ellipsoid	Tri-axial ellipsoid	Tri-axial ellipsoid	Tri-axial ellipsoid	Tri-axial ellipsoid
	Boundary diameters obtained here, µm	0.26–0.30–0.34–0.41–0.43–0.49–0.53–0.72–0.74–0.91–0.92–1.16–1.26–1.65–1.78–3.17–4.06–4.94–5.83	0.29–0.39–0.49–0.64–0.80–1.01–1.30–1.57–2.19–3.54–4.72–7.97–11.57–21.75–34.73	0.27–0.46–0.66–0.95–1.29–2.35–4.28–6.43	0.43–0.55–0.68–0.84–1.05–1.12–1.34–1.47–1.59–1.73–1.87–2.01–2.44–2.83	2.84–3.78–4.86–8.92–15.11–23.49–31.85	0.31–0.40–0.52–0.66–0.84–1.08–1.38–1.77–2.64–3.90–5.42–8.23–12.52

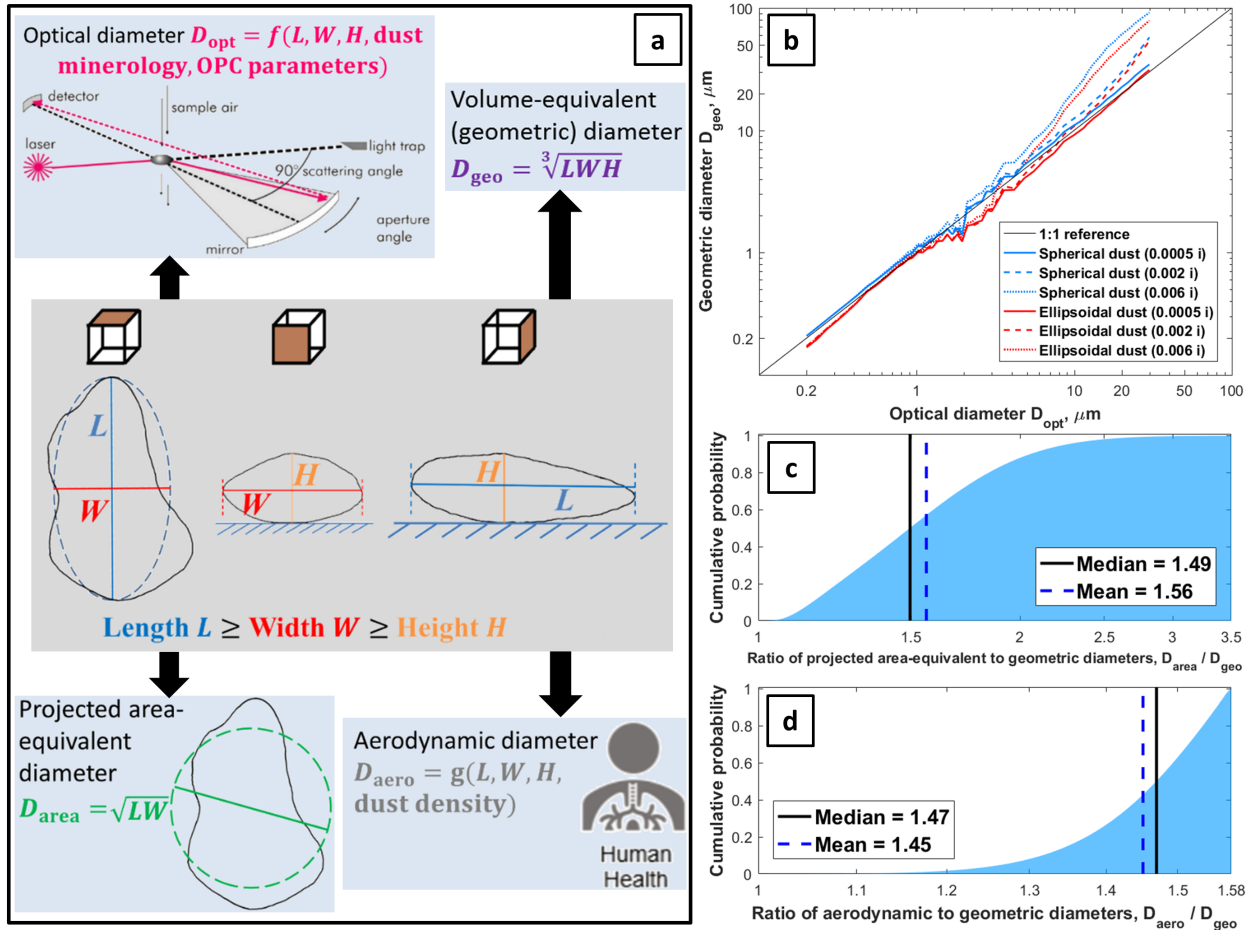


Figure 4.1: Linking the four different diameter types of aspherical dust. Shown are (a) a schematic of four diameter types of an aspherical dust particle, and conversions between (b) the geometric and optical diameters, (c) the projected area-equivalent and geometric diameters, and (d) the aerodynamic and geometric diameters. Diameter conversions in (b-d) account for dust asphericity using the globally averaged shape distributions (Section 4.2.1). In (b), the optical particle counter (OPC) wavelength is taken as 780 nm, the scattering angle range is $90^\circ \pm 60^\circ$, and the real part of dust refractive index is 1.52. These results indicate that optical diameter underestimates geometric diameter at coarse sizes, that projected area-equivalent diameter overestimates geometric diameter by $56.3\% \pm 0.8\%$, and that aerodynamic diameter exceeds geometric diameter by $44.9\% \pm 0.3\%$ (standard errors are propagated from errors in globally averaged shape distributions).

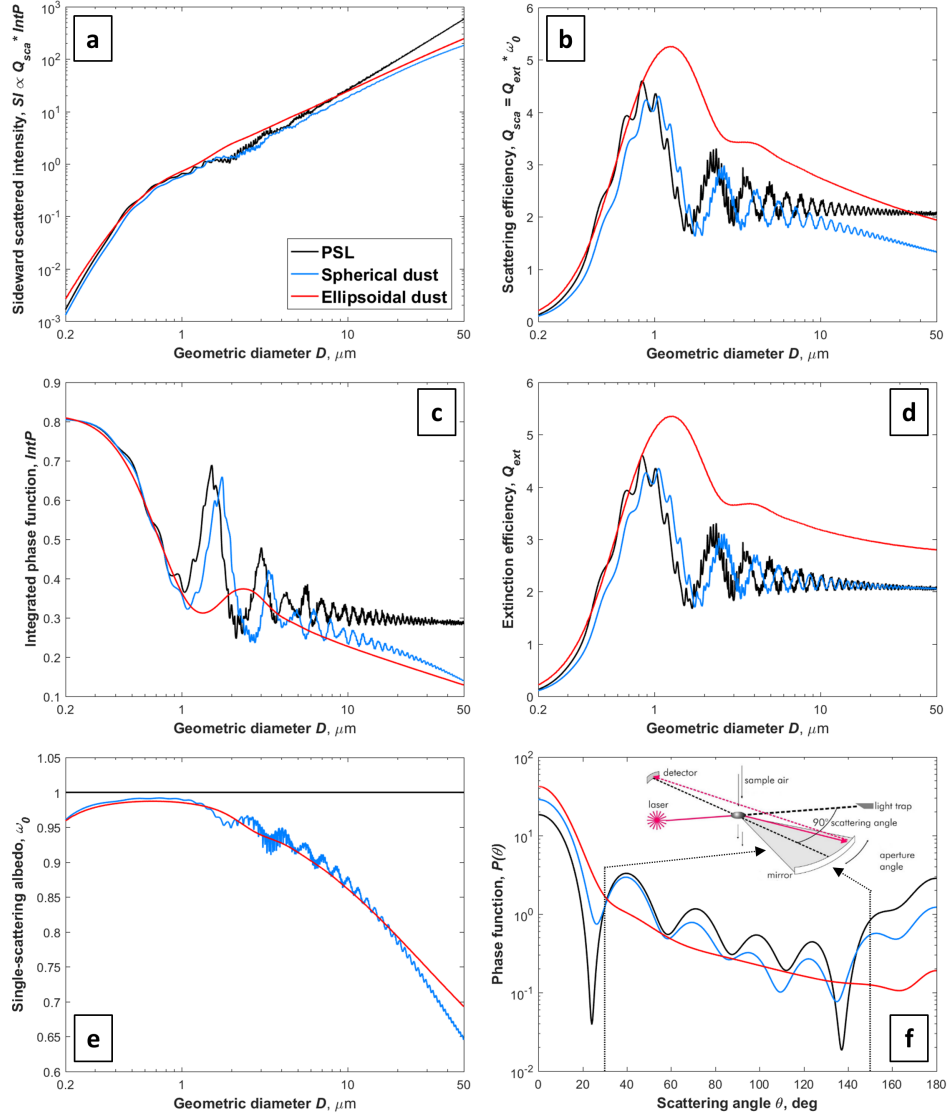


Figure 4.2: Diagnosis of the factors causing optical particle counters (OPCs) to underestimate the size of coarse dust. Shown are (a) the sideward-scattered intensity SI , (b) the scattering efficiency Q_{sca} , and (c) the integrated phase function $IntP$, such that $SI \propto Q_{sca} \times IntP$. The scattering efficiency Q_{sca} is a product of (d) the extinction efficiency Q_{ext} and (e) the single-scattering albedo ω_0 . The integrated phase function $IntP = \frac{1}{2} \int_{\theta_1}^{\theta_2} P(\theta) \sin(\theta) d\theta$ is the (f) phase function $P(\theta)$ integrated over the scattering angle range measured by OPCs (taken here as $90^\circ \pm 60^\circ$; range enveloped in black dotted lines in (f)).

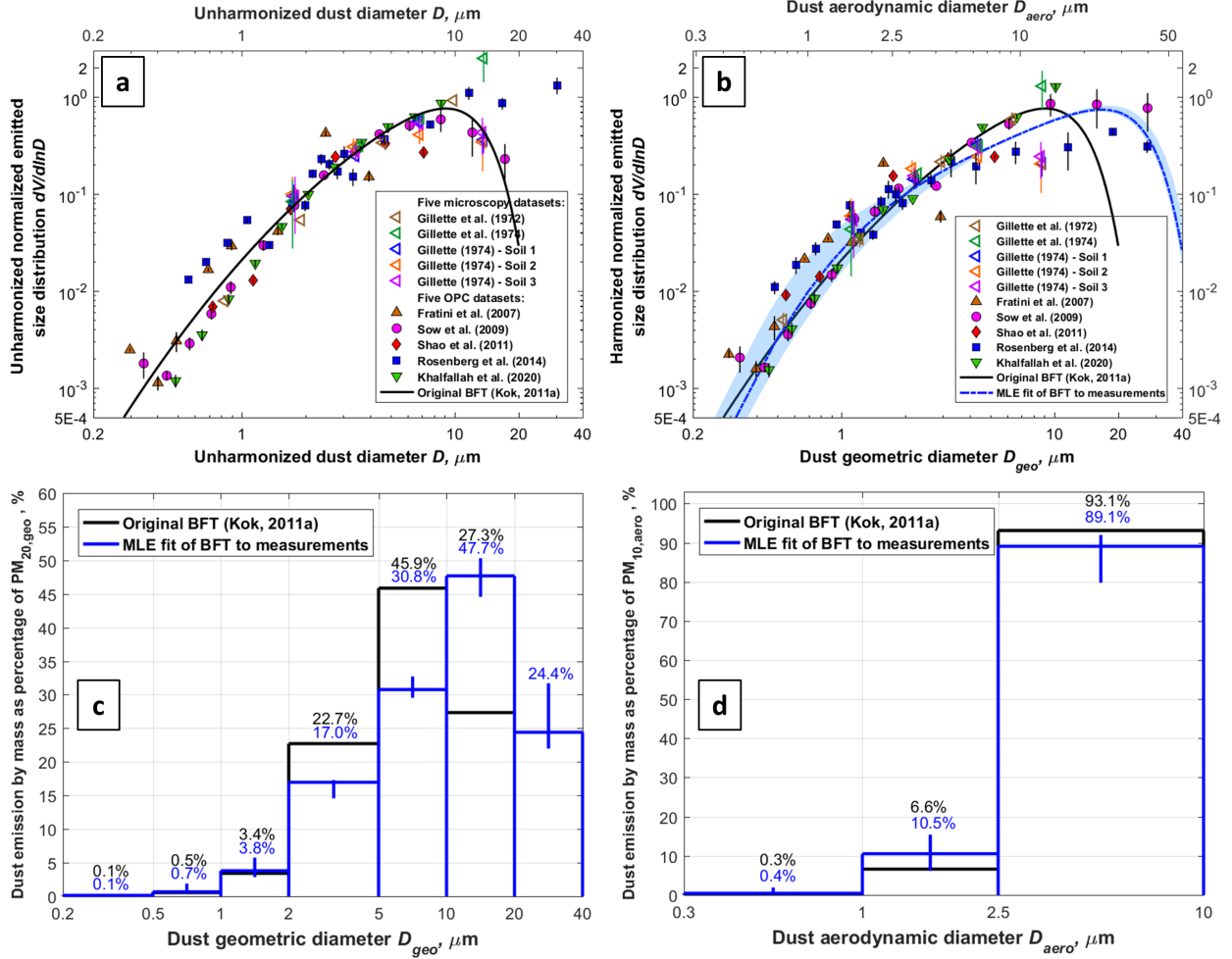


Figure 4.3: Normalized size distributions of emitted dust (a) before and (b) after harmonizing the different diameter types. Also shown are dust emission flux of individual size bins as percentages of (c) the size range within $0 \leq D_{geo} \leq 20\mu\text{m}$ ($PM_{20,geo}$) and (d) the size range within $0 \leq D_{aero} \leq 10\mu\text{m}$ ($PM_{10,aero}$). Vertical error bars in (a and b) denote the standard error of measurements under various wind events at a given soil. In (b), the blue dash-dotted line represents the maximum likelihood estimated (MLE) fit of brittle fragmentation theory (BFT; Kok (2011a)) to the 10 distinct data sets. Blue shading in (b) and vertical error bars in (c and d) denote 95% confidence interval. Compared to the MLE fit, the original BFT parameterization substantially underestimates the mass of emitted dust with $D_{geo} \geq 10\mu\text{m}$.

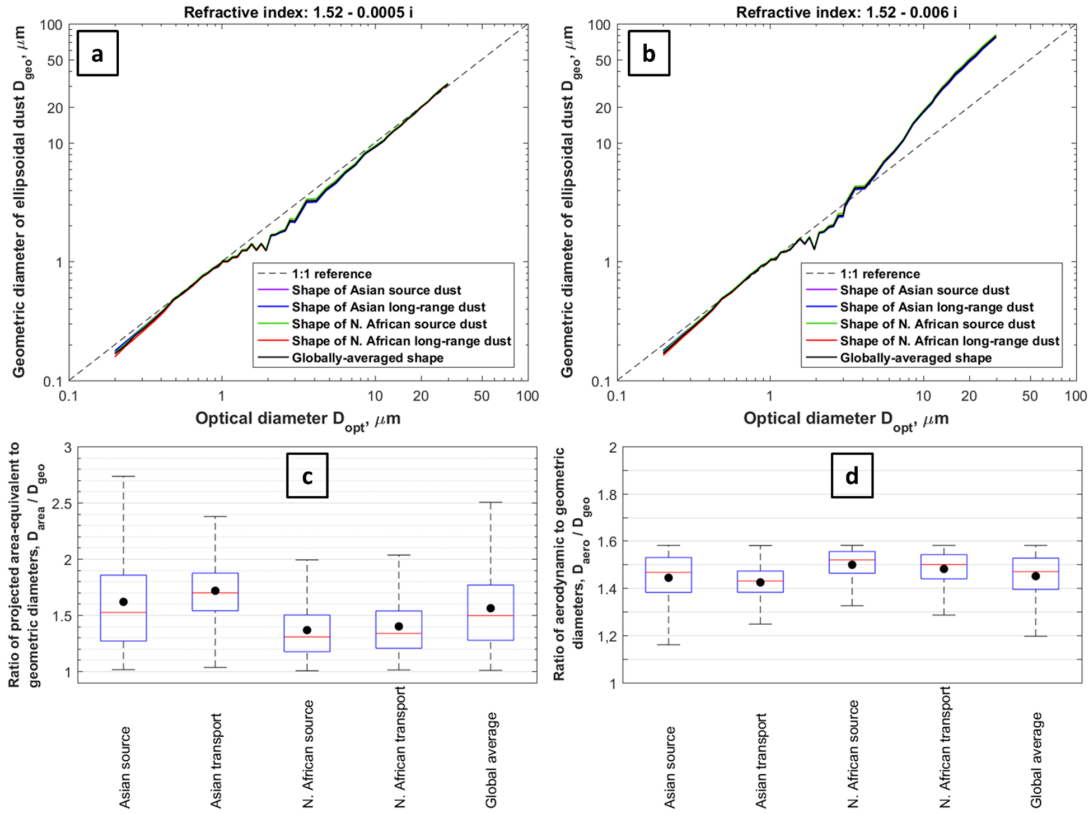


Figure 4.4: Sensitivity tests of the diameter conversions to dust shape distributions. Shown are diameter conversions between the geometric diameter and (a, b) the optical diameter, (c) the projected area-equivalent diameter, and (d) the aerodynamic diameter. Each panel contains diameter conversions under five different shape distributions representing different regions (their shape descriptors are given in Table 4.1). In panels (a) and (b), the wavelength is taken as 780 nm and the scattering angle range is $90^\circ \pm 60^\circ$, as for Fig. 4.1b in the main text. In panels (c) and (d), box plots present the statistics of the distribution of $\frac{D_{area}}{D_{geo}}$ and $\frac{D_{aero}}{D_{geo}}$, respectively. In each box plot, the central red line denotes the median, the black dot denotes the mean, the bottom and top edges of the blue box denote respectively the 25th- and 75th- percentiles, and the whiskers denote 95% confidence interval. These results indicate that regional differences in dust shape distributions produce only minor differences in diameter conversions.

CHAPTER 5

Single-scattering properties of ellipsoidal dust accounting for realistic shape distribution

[**Huang, Y.**, J. F. Kok, and O. Muñoz, Single-scattering properties of ellipsoidal dust accounting for realistic shape distribution, in preparation.]

Abstract

Accurate single-scattering properties of dust aerosols are critical to the global aerosol models and retrieval algorithms of remote sensing products to correctly simulate and retrieve dust distributions and estimate dust impacts. However, inconsistent and inaccurate quantifications of dust shape and shape distributions are used in models and retrievals, generating biases that propagate into estimated dust distributions and dust impacts. To improve models and retrieval algorithms in terms of dust shape quantification, here we for the first time account for a realistic dust shape distribution in obtaining single-scattering properties of dust aerosols. We find that neglecting the asphericity of dust and approximating dust as spherical particles underestimates the extinction efficiency, the mass extinction efficiency, the asymmetry factor, and the single-scattering albedo for all dust sizes at both shortwave and longwave spectra, since global aerosol models approximate dust as spheres. In addition, we find that the inaccurate quantification of dust shape in retrieval algorithms causes them

to generate an incorrect magnitude and wavelength dependence of the linear depolarization ratio relative to observations. Our new ellipsoidal dust optics accounting for realistic shape distributions produce an excellent agreement with the measured linear depolarization ratio. Although the new ellipsoidal dust optics show potential to improve models and retrievals, it underestimates the magnitude of the backscattering intensity relative to laboratory and field observations. This finding indicates that a realistic quantification of dust body shape is not sufficient and that an accurate quantification of dust surface texture is also critical to accurately reproduce dust optical properties at backscattering angles.

5.1 Introduction

Desert dust is likely the most dominant aerosol type by mass in the atmosphere (Gliß et al., 2021). Dust produces important effects on the Earth system throughout the dust cycle (including dust emission, short- and long-range transport, and deposition; *Shao et al.* (2011b)). First, dust absorbs and scatters both shortwave and longwave radiation, thereby directly modulating the Earth’s energy budget (*Kok et al.*, 2017; *Di Biagio et al.*, 2020). Second, dust acts as nuclei for cloud droplets and ice crystals, thereby modifying cloud microphysical properties and affecting the energy budget indirectly (*DeMott et al.*, 2015; *Kiselev et al.*, 2017). Third, dust carries key nutrients (i.e., iron and phosphorus), and its deposition to the downwind ocean and land boosts primary productivity and carbon sequestration (*Yu et al.*, 2015; *Ito et al.*, 2019). In this way, dust aerosols affect the carbon cycle and associated climate feedbacks. Furthermore, dust aerosols impact anthropogenic activities, including by depleting renewable energy generation (*Piedra and Moosmüller*, 2017; *Piedra et al.*, 2018), degrading regional air quality and visibility (*Mahowald et al.*, 2007; *Huang et al.*, 2019), and producing hazards to human health (*Burnett et al.*, 2014; *Giannadaki et al.*, 2014). To estimate these varied effects, accurate quantifications of the varying spatial and temporal dust distributions are needed and thus are key scientific objectives for a range of studies (*Huneeus et al.*, 2011; *Ginoux et al.*, 2012; *Ito et al.*, 2021; *Klose et al.*, 2021; *Kok et al.*, 2021a,b).

To simulate and retrieve dust’s abundance and spatiotemporal variability, dust single-scattering properties are needed in global aerosol models and retrieval algorithms of passive and active remote sensing products (e.g., *Dubovik et al. (2006)*; *Colarco et al. (2014)*; *Kahn and Gaitley (2015)*; *Tesche et al. (2019)*). These single-scattering properties are highly sensitive to dust shape (*Nousiainen and Kandler, 2015*). However, inconsistent assumptions about dust shape and shape distribution are used in models and retrieval algorithms. Specifically, current global aerosol models assume that dust aerosols are spherical (Table 5.1; Figure 3.5a); that is, models do not use a shape distribution to quantify dust single-scattering properties (*Hess et al., 1998*). While some retrieval algorithms approximate dust as spherical particles, most other retrieval algorithms approximate dust as spheroidal particles (Figures 3.5b and 3.5c; *Dubovik et al. (2006)*; *Hsu et al. (2019)*; *Tesche et al. (2019)*). The shape distribution of spheroidal dust is in general taken as the one that enables the simulated scattering matrix to reach the least disagreement relative to the laboratory-measured scattering matrix of a sample of crushed feldspar rocks (*Muñoz et al., 2012*), for instance in version 2 and version 3 algorithms of Aerosol Robotic Network (AERONET; *Dubovik et al. (2006)*) and the new Deep Blue algorithm (*Hsu et al., 2019*). Although this optimized shape distribution helps reach the best fit against laboratory observations, it differs substantially from in situ measurements of dust shape and shape distributions (*Huang et al., 2020*). Specifically, retrieval algorithms assume that two of the three dust dimensions are equal (Figures 3.5b and 3.5c), whereas extensive measurements have found that the three dimensions are highly different from each other (Figures 3.2a and 3.2b; *Huang et al. (2020)*). Furthermore, this optimized shape distribution assumes that dust length is on average 1.7 times larger than dust height, whereas extensive measurements have found that dust length is on average ~ 5 times larger than dust height (Figure 3.2c; *Huang et al. (2020)*). That is, retrieval algorithms substantially underestimate the dust asphericity. As such, the assumptions about dust shape and shape distribution in models and retrieval algorithms are not only inconsistent, but also inaccurate. These biases in dust shape and shape distribution can propagate into the

calculated single-scattering properties and ultimately into the simulated and retrieved dust distributions and the estimated dust impacts (*Yi et al.*, 2011; *Colarco et al.*, 2014).

To improve models and retrieval algorithms in terms of dust shape quantification, we investigate for the first time whether accounting for realistic dust shape distributions enables improved single-scattering properties. Section 5.2 details the globally representative dust shape distribution obtained from a measurement compilation, the shape-resolved single-scattering properties of ellipsoidal dust from an extensive database, and the combination of the shape distribution and shape-resolved single-scattering properties to yield single-scattering properties of ensemble dust aerosols. Section 5.3 presents results of the scattering angle-integrated single-scattering properties of dust ensembles (including the extinction efficiency, the mass extinction efficiency, the asymmetry factor, and the single-scattering albedo). Since almost all models approximated dust as spheres, these results quantify the biases in models due to inaccurate dust shape quantification. Section 5.4 presents results of scattering angle-resolved single-scattering properties of dust ensembles (i.e., the scattering matrices) and the resulting lidar ratio and linear depolarization ratio. These results are then validated against laboratory observations of the scattering matrices and field measurements of the lidar ratio and the linear depolarization ratio. Since retrieval algorithms use the lidar ratio and the linear depolarization ratio to distinguish dust from other types of aerosols, these results investigate the biases in retrieval algorithms due to inaccurate dust shape quantification. Discussions and conclusions follow in Section 5.5.

5.2 Methods

In Section 5.2.1, we first introduce the globally representative shape distribution, which approximates desert dust as tri-axial ellipsoids. In Section 5.2.2, we introduce an extensive database of the single-scattering properties of tri-axial ellipsoidal dust particles that is resolved by a wide range of shape, size, wavelength, and refractive index values. We then

combine the shape distribution and the shape-resolved single-scattering database to obtain the globally representative single-scattering properties of dust ensembles.

5.2.1 Dust shape and shape distribution

We approximate dust as tri-axial ellipsoids whose asphericity is quantified by the ratio of the particle length L to the width W (the aspect ratio, AR) and the height-to-width ratio (HWR) ($L \leq W \leq H$; Figure 3.5d). We use AR ($= L/W$) and HWR ($= H/W$) to quantify dust shape, because they are the most widely measured shape descriptors (*Huang et al.*, 2020) and they are less sensitive to microscopic image resolution and artifacts than other shape descriptors (*Almeida-Prieto et al.*, 2007; *Kandler et al.*, 2011).

To quantify the shape distribution of ellipsoidal dust, we assume that AR and HWR both follow lognormal distributions after a range of measurements (e.g., *Okada et al.* (2001); *Kandler et al.* (2007, 2009, 2011); *Sakai et al.* (2010)). A recent work compiled dozens of studies of AR and HWR across the world (See Section 3.2.1 and Figure 3.2; *Huang et al.* (2020)). Each of these studies measured the values of AR and HWR of an extensive number (from several hundred to tens of thousands) of individual dust aerosols (see the legend of Figure 3.2), which enabled *Huang et al.* (2020)'s compilation to be statistically significant. *Huang et al.* (2020) found that both AR and HWR deviate substantially from unity, and thus that the ellipsoidal approximation of dust shape is more realistic than spherical or spheroidal approximations (Figures 3.2 and 3.5). In addition, they found that both shape descriptors show little dependence on dust size, that AR and HWR are not correlated, and that little difference exists in AR and HWR distributions for dust from two of the largest dust sources of the world (i.e., Asian and North African sources; *Kok et al.* (2021a,b)). These findings enable two simple mathematical expressions of AR and HWR to represent the dust shape distributions at a global scale. Indeed, both HWR and the deviation of AR from unity (AR-1) follow lognormal distributions as Equations (3.1) and (3.2) (see Section 3.2.1). In the present study, we thus take the medians of AR and HWR as 1.70 ± 0.03

and 0.40 ± 0.07 , respectively, and the geometric standard deviations of AR-1 and HWR respectively as 0.70 ± 0.02 and 0.73 ± 0.09 , after the globally averaged distributions of AR and HWR (*Huang et al.*, 2020). Using these two shape distributions can substantially improve models and retrieval algorithms in terms of dust shape quantification, since current models and retrieval algorithms substantially underestimate dust asphericity by a factor of ~ 3 to 5 (Figure 3.2c).

5.2.2 Single-scattering properties of ellipsoidal dust

Single-scattering properties quantify the modification of aerosols on the incident light after one instance of elastic scattering (*Liou*, 2002). There are two categories of single-scattering properties based on whether they are dependent on the scattering angle or not. The first category (including the extinction efficiency, Q_{ext} , the single-scattering albedo, SSA , and the asymmetry factor, g) is independent on the scattering angle, and is needed in global aerosol models to simulate dust distributions and dust impacts (*Hess et al.*, 1998). The second category of single-scattering properties (i.e., the scattering matrix, $P_{4 \times 4}$) is highly sensitive to the scattering angle; the resulting lidar ratio, S , and the linear depolarization ratio, δ , are needed in retrieval algorithms to distinguish dust from other types of aerosols (*Dubovik et al.*, 2006; *Müller et al.*, 2012; *Gómez Martín et al.*, 2021). We introduce these single-scattering properties in detail below.

For incident light (with intensity I_i , linear polarization components Q_i and U_i , and circular polarization component V_i), the properties of the scattered light (with intensity I_s , linear polarization components Q_s and U_s , and circular polarization component V_s) after one single-scattering event with one aerosol particle is

$$\begin{bmatrix} I_s \\ Q_s \\ U_s \\ V_s \end{bmatrix} = \frac{C_{sca}}{4\pi s^2} \begin{bmatrix} P_{11} & P_{12} & P_{13} & P_{14} \\ P_{21} & P_{22} & P_{23} & P_{24} \\ P_{31} & P_{32} & P_{33} & P_{34} \\ P_{41} & P_{42} & P_{43} & P_{44} \end{bmatrix} \begin{bmatrix} I_i \\ Q_i \\ U_i \\ V_i \end{bmatrix} \quad (5.1)$$

where s (unit: m) is the distance between the light detector and the scatterer (i.e., the particle), C_{sca} (unit: m^2) is the scattering cross section of the particle, and the 4×4 matrix $P_{4 \times 4}$ (unitless) is the scattering matrix (also referred to as the Mueller matrix or the phase matrix) (Nousiainen and Kandler, 2015; Mishchenko and Yurkin, 2017; Saito et al., 2021). $C_{sca} = Q_{sca} \times A$ and Q_{sca} (unitless) is the scattering efficiency that quantifies a particle's ability to scatter relative to its physical cross-sectional area, A (unit: m^2) (Liou, 2002). In analogy to C_{sca} , $C_{abs} = Q_{abs} \times A$ and $C_{ext} = Q_{ext} \times A$ quantify respectively the absorbing and extinction (absorbing plus scattering) cross sections of this particle (Liou, 2002). The single-scattering albedo,

$$SSA = \frac{C_{sca}}{C_{ext}} \quad (5.2)$$

describes the portion of scattered light to extinguished light, and therefore is in between 0 to 1 (Liou, 2002). The scattering matrix reduces to six independent elements for randomly oriented particles, like dust aerosols (Nousiainen and Kandler, 2015; Mishchenko and Yurkin, 2017; Saito et al., 2021),

$$P_{4 \times 4}(\theta) = \begin{bmatrix} P_{11}(\theta) & P_{12}(\theta) & 0 & 0 \\ P_{12}(\theta) & P_{22}(\theta) & 0 & 0 \\ 0 & 0 & P_{33}(\theta) & P_{34}(\theta) \\ 0 & 0 & -P_{34}(\theta) & P_{44}(\theta) \end{bmatrix} \quad (5.3)$$

where $P_{11}(\theta)$ is the phase function quantifying the angular distribution of the scattered intensity, such that the integration of the phase function against the scattering angle, θ , and the azimuth angle, ϕ , yields 4π ,

$$\int_0^{2\pi} \int_0^\pi P_{11}(\theta) \sin(\theta) d\theta d\phi = 4\pi \quad (5.4)$$

In addition, $-\frac{P_{12}(\theta)}{P_{11}(\theta)}$ quantifies the degree of linear polarization of the scattered light for the unpolarized component of the incident light, and $1 - \frac{P_{22}(\theta)}{P_{11}(\theta)}$ describes the depolarization of the scattered light for the linear-polarized component of the incident light (Nousiainen and Kandler, 2015). $P_{33}(\theta)$, $P_{34}(\theta)$, and $P_{44}(\theta)$ quantify the circular polarization components

(Liou, 2002). The asymmetry factor scales with the portion of forward scattering,

$$\begin{aligned} g &= \frac{1}{4\pi} \int_0^{2\pi} \int_0^\pi P_{11}(\theta) \sin(\theta) \cos(\theta) d\theta d\phi \\ &= \frac{1}{2} \int_0^\pi P_{11}(\theta) \sin(\theta) \cos(\theta) d\theta \end{aligned} \quad (5.5)$$

where $g = 0$ when the scattered intensity is equally distributed at all scattering angles, and g increases with increasing forward scattering (Liou, 2002). The lidar ratio quantifies the ratio of extinguished light to backscattered light (Nousiainen and Kandler, 2015),

$$S = 4\pi \frac{C_{ext}}{C_{sca} \times P_{11}(\pi)} \quad (5.6)$$

The linear depolarization ratio describes how the degree of linear polarization of the transmitted light decreases through scattering for backscattered light as (Nousiainen and Kandler, 2015),

$$\delta = \frac{P_{11}(\pi) - P_{22}(\pi)}{P_{11}(\pi) + P_{22}(\pi)} \quad (5.7)$$

All the above mentioned single-scattering properties (including the extinction efficiency, Q_{ext} , the single-scattering albedo, SSA , the asymmetry factor, g , the scattering matrix, $P_{4 \times 4}$, the lidar ratio, S , and the linear depolarization ratio, δ) are sensitive to dust refractive index ($m = n - ki$), dust size (D), dust shape (AR and HWR), and the light wavelength (λ). In addition, $P_{4 \times 4}$ is also sensitive to the scattering angle, θ .

An extensive database of the single-scattering properties of tri-axial ellipsoidal dust particles is available (Meng *et al.*, 2010). This database combines four computational methods (Lorenz-Mie theory, T-matrix method, discrete dipole approximation, and an improved geometric optics method) to compute the single-scattering properties of ellipsoidal dust for a wide range of AR, HWR, size parameter, and refractive index values. This database contains the single-scattering properties (including the extinction efficiency, Q_{ext} , the single-scattering albedo, SSA , the asymmetry factor, g , and the six non-zero elements of the scattering matrix, $P_{4 \times 4}$) at:

1. 9 real parts of dust refractive index, $n = 1.10, 1.20, 1.30, 1.40, 1.50, 1.60, 1.70, 1.90,$ and 2.10 ;

2. 10 imaginary parts of dust refractive index, $k = 0.0005, 0.001, 0.005, 0.01, 0.02, 0.05, 0.08, 0.1, 0.2,$ and 0.5 ;

3. 11 values of HWR, $HWR = 0.30, 0.37, 0.42, 0.48, 0.56, 0.67, 0.83, 0.86, 0.89, 0.91,$ and 1.00 ;

4. 11 values of AR, $AR = 1.00, 1.10, 1.13, 1.16, 1.20, 1.50, 1.80, 2.10, 2.40, 2.70,$ and 3.30 ;

5. 100 size parameters ranging in between 0.025 and 1000; note that the size parameter in *Meng et al.* (2010) is defined as $x = \frac{\pi L}{\lambda}$, where λ is the wavelength and L is the largest dimension of an ellipsoidal dust (Figure 3.5d).

The single-scattering properties at values in between the pre-calculated results of $n, k, HWR, AR,$ and x are obtained through a five-dimensional linear interpolation method (after *Meng et al.* (2010)). The interpolation code is directly obtained from the authors of *Meng et al.* (2010).

We combine this extensive database and the globally representative shape distributions to obtain globally representative single-scattering properties of dust ensembles. Specifically, at a given $n, k, \lambda,$ and volume-equivalent diameter $D,$ we obtain single-scattering properties integrated against the two dust shape distributions (i.e., $f(AR)$ and $f(HWR)$; see Equations (3.1) and (3.2)) as (*Seinfeld and Pandis, 2016*),

$$\begin{aligned} \widehat{\beta}_{ext,ens}(n, k, \lambda, D) &= \int_{HWR_1}^{HWR_2} \int_{AR_1}^{AR_2} \frac{\pi D^2}{4} \times Q_{ext}(n, k, \lambda, D, AR, HWR) \\ &\times f(AR) \times f(HWR) dAR dHWR \end{aligned} \quad (5.8)$$

$$\begin{aligned} \widehat{\beta}_{sca,ens}(n, k, \lambda, D) &= \int_{HWR_1}^{HWR_2} \int_{AR_1}^{AR_2} \frac{\pi D^2}{4} \times Q_{ext}(n, k, \lambda, D, AR, HWR) \times SSA(n, k, \lambda, D, \\ &AR, HWR) \times f(AR) \times f(HWR) dAR dHWR \end{aligned} \quad (5.9)$$

$$SS\widehat{A}_{ens}(n, k, \lambda, D) = \frac{\beta_{sca,ens}(n, k, \lambda, D)}{\beta_{ext,ens}(n, k, \lambda, D)} \quad (5.10)$$

$$Q_{ext,ens}(n, k, \lambda, D) = \frac{\beta_{ext,ens}(n, k, \lambda, D)}{\frac{\pi D^2}{4}} \quad (5.11)$$

$$\begin{aligned} \widehat{P}_{ij,ens}(n, k, \lambda, D, \theta) &= \frac{1}{\beta_{sca,ens}(n, k, \lambda, D)} \times \int_{HWR_1}^{HWR_2} \int_{AR_1}^{AR_2} \frac{\pi D^2}{4} \times Q_{ext}(n, k, \lambda, D, AR, HWR) \\ &\times SSA(n, k, \lambda, D, AR, HWR) \times P_{ij}(n, k, \lambda, D, AR, HWR, \theta) \times f(AR) \\ &\times f(HWR) dAR dHWR \end{aligned} \quad (5.12)$$

$$\widehat{g}_{ens}(n, k, \lambda, D) = \frac{1}{2} \times \int_0^\pi P_{11,ens}(n, k, \lambda, D, \theta) \sin(\theta) \cos(\theta) d\theta \quad (5.13)$$

where the subscripts “*ens*” denote dust ensemble properties, $\widehat{\beta}_{ext,ens}$ is the bulk volume extinction coefficient, $\widehat{\beta}_{sca,ens}$ is the bulk volume scattering coefficient, $AR_1 = 1.0$, $AR_2 = 3.3$, $HWR_1 = 0.3$, and $HWR_2 = 1.0$. In addition, in Equation (5.12), $ij=11, 12, 22, 33, 34,$ and 44 . As such, we obtain the single-scattering properties of tri-axial ellipsoidal dust ensembles for a four-dimensional space resolved by dust refractive index (n and k), dust volume-equivalent diameter (D), and the wavelength of light (λ).

5.3 Single-scattering properties in aerosol models

All the 14 global aerosol models included in the Aerosol Comparisons between Observation and Models (AeroCom) phase III experiments assume that dust aerosols are spherical (Table 5.1). AeroCom is a modeling intercomparison project that fixes the meteorological fields used by all participant models and uses the output multi-model ensembles to identify strengths and weaknesses of individual aerosol modules and assesses the uncertainties of aerosol optical properties and the associated aerosol radiative forcing (*Kinne et al., 2006; Huneeus et al.,*

2011). AeroCom phase III presents the most recent results of multi-model ensembles and the evaluations of models against observations (Gliß et al., 2021). All the 14 models assume that dust aerosols are spherical (Table 5.1 and Figure 3.5a), thereby underestimating the dust asphericity by a factor of 5 relative to observations of dust shape (Figure 3.2).

To quantify the biases in models due to inaccurate dust shape quantification, we compare the single-scattering properties of spherical and tri-axial ellipsoidal dust at both shortwave and longwave spectrum (Figure 5.1 and Tables 5.2 and 5.3). We have four key findings. First, models that approximate dust particles as spheres underestimate the extinction efficiency, Q_{ext} , for all dust sizes at both shortwave and longwave spectrum (Figures 5.1a and 5.1e). At the wavelength of 500 nm, Q_{ext} of ellipsoidal dust is slightly larger (by ~ 0.3) than Q_{ext} of volume-equivalent spherical dust at sizes where dust size is smaller than the wavelength (i.e., size parameter, $x < \sim 3$); at sizes where dust size is comparable to the wavelength (i.e., $D = \sim 1\mu m$), Q_{ext} of ellipsoidal dust is 70% larger than Q_{ext} of spherical dust; at sizes where dust size is larger than the wavelength (i.e., $x > \sim 5$), Q_{ext} of ellipsoidal dust is larger than Q_{ext} of spherical dust by ~ 0.8 . Furthermore, the peak value of Q_{ext} of ellipsoidal dust is around 5.1 and the peak of Q_{ext} of spherical dust is around 4.3. Similar dependence on dust size occurs at the wavelength of 10 μm . At small sizes, Q_{ext} of ellipsoidal dust is slightly larger (by ~ 0.5) than Q_{ext} of volume-equivalent spherical dust; this enhancement by 55% peaks at $D = \sim 10\mu m$; at large sizes, Q_{ext} of ellipsoidal dust is larger than Q_{ext} of spherical dust by ~ 1.0 . Furthermore, the peak value of Q_{ext} of ellipsoidal dust is around 4.2 and the peak of Q_{ext} of spherical dust is around 3.0. The enhancement in the extinction efficiency after accounting for realistic dust asphericity occurs because an aspherical dust particle has a larger surface area than a volume-equivalent spherical dust to modulate the incident light (Kalashnikova and Sokolik, 2004; Colarco et al., 2014; Kok et al., 2017).

Second, models that approximate dust particles as spheres also underestimate the mass extinction efficiency, MEE , for all dust sizes at both shortwave and longwave spectra (Figures 5.1b and 5.1f). This occurs because MEE is a function of Q_{ext} , as $MEE = \frac{3}{2\rho D} \times Q_{ext}$

(where $\rho \approx 2500 \text{ kg} \times \text{m}^{-3}$ is the typical density of dust aerosols; *Kok et al. (2017)*).

Third, models that approximate dust particles as spheres underestimate the asymmetry factor, g , for all sizes at both the shortwave and longwave spectra (Figures 5.1c and 5.1g). This occurs because ellipsoidal dust has a larger forward scattering portion than volume-equivalent spherical dust (*Meng et al., 2010; Nousiainen and Kandler, 2015; Huang et al., 2021*), causing an enhancement in g after accounting for realistic dust asphericity. We notice that at the wavelength of $10 \mu\text{m}$, g of spherical dust is slightly higher than g of ellipsoidal dust at super-coarse sizes in between ~ 15 to $60 \mu\text{m}$. This range is equivalent to $D = 1.5$ to $3 \mu\text{m}$ at the wavelength of 550 nm . They occur due to the oscillation nature of Lorenz-Mie theory when particle size is comparable to the light wavelength (*Liou, 2002*).

Finally, models that approximate dust particles as spheres underestimate the single-scattering albedo, SSA , for most sizes at both the shortwave and longwave spectra (Figures 5.1d and 5.1h). SSA of ellipsoidal dust is slightly larger than SSA of volume-equivalent spherical dust at sizes where dust size is smaller than the wavelength (i.e., $x < \sim 3$); at sizes where dust size is comparable to the wavelength (i.e., $x \sim 2$ to 3), SSA of ellipsoidal dust is larger than SSA of spherical dust; at sizes where dust size is larger than the wavelength (i.e., $\sim 5 < x < \sim 85$), SSA of ellipsoidal dust is smaller than SSA of spherical dust; at super-coarse dust sizes (i.e., $x > \sim 85$), SSA of ellipsoidal dust is larger than SSA of spherical dust. The enhancement in the single-scattering albedo after accounting for realistic dust asphericity occurs because extinction scales with particle surface area whereas absorption scales with particle volume (*Liou, 2002*). Since an aspherical dust has a larger surface area but the same volume as a volume-equivalent spherical dust particle, this aspherical dust has a larger single-scattering albedo than the volume-equivalent spherical dust particle.

5.4 Single-scattering properties in remote sensing retrievals

Global aerosol models only need accurate scattering angle-independent single-scattering properties to simulate dust distributions and impacts (Section 5.3), whereas the retrieval algorithms of remote sensing products need accurate scattering angle-dependent single-scattering properties. Here, we first evaluate the scattering matrix of ellipsoidal dust ensemble against laboratory observations of the scattering matrix in Section 5.4.1. We then evaluate the lidar ratio and the linear depolarization ratio of ellipsoidal dust ensemble against field measurements in Section 5.4.2.

5.4.1 Evaluating the scattering matrix

The Amsterdam-Granada light scattering database (AGLSD; *Muñoz et al.* (2012)) is widely regarded as the standard to evaluate dust optical models (*Dubovik et al.*, 2006; *Merikallio et al.*, 2011; *Lindqvist et al.*, 2014; *Nousiainen and Kandler*, 2015; *Saito et al.*, 2021). AGLSD includes laboratory measurements of the six non-zero elements of the scattering matrices of a large number of aerosol samples at two different wavelengths, as well as the size distributions of these samples (Figure 5.2). In this study, we select one mineral sample (i.e., feldspar) and two dust samples (i.e., Gobi and SaharaOSN) (Figure 5.2) to evaluate the scattering matrix. We discuss the reason why we select these three samples below.

We compare against measurements of the scattering matrix of a crushed sample of feldspar rock (*Volten et al.*, 2001), because this is the only sample used to validate the retrieval algorithms of AERONET (*Dubovik et al.*, 2006). Specifically, *Dubovik et al.* (2006) first pre-calculated a kernel containing single-scattering properties of spheroidal dust that are resolved by refractive index, size, wavelength, and aspect ratio (defined as dust length to its height; Figure 3.5). Second, *Dubovik et al.* (2006) used this kernel to retrieve the distribution of aspect ratio at 441 nm for which the simulated scattering matrix showed the least disagreement with measurement of the scattering matrix of feldspar at 441 nm (see the

blue line in Figure 13 of *Dubovik et al. (2006)*). Third, similar to the second step, *Dubovik et al. (2006)* used this kernel to retrieve the distribution of aspect ratio at 633 nm (see the red line in Figure 13 of *Dubovik et al. (2006)*). Finally, since the retrieved aspect ratio distribution at 441 nm is different from that at 633 nm, *Dubovik et al. (2006)* calculated the averaged retrieved aspect ratio distribution (Figure 5.3 and the green line in Figure 13 of *Dubovik et al. (2006)*); this averaged shape distribution has been used in retrieval algorithms of AERONET and a range of other remote sensing products by default. However, to reach agreement at both wavelengths, different shape distributions are retrieved at different wavelengths, indicating that the optical model of spheroidal dust does not adequately represent actual atmospheric dust particles (*Nousiainen and Kandler, 2015; Huang et al., 2020*). Also, the averaged retrieved aspect ratio distribution substantially underestimates measurements of dust asphericity (Figure 5.3). This study aims to test if accounting for realistic dust shape and shape distribution results in an improved agreement with laboratory measurements, relative to *Dubovik et al. (2006)*. To do so, we compare the laboratory measurements of the scattering matrix of feldspar, the simulated scattering matrix using *Dubovik et al. (2006)*'s kernel and the averaged retrieved shape distribution, the simulated scattering matrix using *Meng et al. (2010)*'s database and the shape distributions from measurement compilation, and the simulated scattering matrix using Lorenz-Mie theory (*Liou, 2002; Mätzler, 2002*).

In addition to feldspar, we also use the two newest dust samples (i.e., Gobi and SaharaOSN) added to the Amsterdam-Granada light scattering database (*Gómez Martín et al., 2021*). These two dust samples are collected during a severe dust storm in Beijing on April 16th 2006 and during a Saharan dust transport event reaching the Observatory of Sierra Nevada in Spain in 2004, respectively. These two samples are deposited dust aerosols, which are different from other mineral samples included in the AGLSD that were either purchased from commercial sources or generated in the lab by grinding the mineral rocks and are thus less accurate representations of dust aerosols (*Volten et al., 2001; Muñoz et al., 2012*).

Due to the reasons in the above paragraphs, we thus use the three AGLSD samples

(i.e., feldspar, Gobi, and SaharaOSN) in our evaluation of whether angle-dependent dust optics based on ellipsoids better reproduces measurements than the prevailing optics based on spheroids that are used in many remote sensing retrievals. Specifically, we compare the six laboratory-measured non-zero elements of the scattering matrix of the three AGLSD samples against three types of simulated scattering matrix elements: (1) the first simulation combines AGLSD samples' size distributions and spherical optics calculated by Lorenz-Mie theory (*Liou, 2002; Mätzler, 2002*); (2) the second simulation combines AGLSD samples' size distributions, *Dubovik et al. (2006)*'s kernel of spheroidal dust optics, and *Dubovik et al. (2006)*'s averaged retrieved distribution of aspect ratio; and (3) the third simulation combines AGLSD samples' size distributions, *Meng et al. (2010)*'s database of ellipsoidal dust optics, and *Huang et al. (2020)*'s compiled lognormal distributions of AR and HWR. In addition, we use the same refractive index and the same wavelength for all three types of simulations. As such, any difference in the simulated scattering matrix will be due to the different approximations of dust shape and shape distribution.

The comparisons between observations and the three types of simulations yield several key findings. First, optics using the ellipsoidal dust shape and shape distribution show better agreement against measurements of the feldspar scattering matrix than optics using the spheroidal shape and shape distribution (Figures 5.4 and 5.7). These improvements include that (1) ellipsoid optics show an improved wavelength dependence of the phase function P_{11} , (2) the sign of $-\frac{P_{12}}{P_{11}}$ of ellipsoid optics agrees with observations at all scattering angles, whereas spheroid optics show a problematic negative value around 160° , and (3) the magnitudes of all the six elements of ellipsoid optics agree better with observations at almost all scattering angles than spheroid optics. Note that the shape distribution of spheroid optics was obtained by best fitting the simulated scattering matrix against the measured scattering matrix of feldspar whereas no such optimization was done for the ellipsoid optics. Therefore, using a realistic shape distribution for spheroidal simulations will result in even greater disagreement with the measured scattering matrix of feldspar. This further strengthens our

finding that ellipsoidal dust shape and shape distribution show an improved agreement with the measurement of feldspar.

Our second finding is that although a significantly improved agreement occurs in reproducing the scattering matrix of feldspar, the ellipsoid optics do not show an obvious improvement for the two dust samples (Figures 5.5, 5.6, 5.8, and 5.9). Ellipsoid optics have smaller magnitudes of P_{11} at the scattering angle $\sim 60^\circ$ and backward scattering angles (i.e., in between $\sim 140^\circ$ to 180°) than spheroid optics and observations. In addition, neither the ellipsoid optics nor the spheroid optics can reproduce all the six laboratory-measured elements well. Note that although these two dust samples are significantly coarser in size than the feldspar sample (Figure 5.2), they have a stronger ability to backscatter light (i.e., P_{11} at backscatter angles) and a weaker ability to polarize incident unpolarized light (i.e., $-\frac{P_{12}}{P_{11}}$) and depolarize incident linear polarized light (i.e., $\frac{P_{22}}{P_{11}}$) compared to feldspar. This indicates that differences in the mineralogy and morphology between the two dust samples and feldspar determine the scattering matrix, instead of the difference in sample size. Therefore, it makes sense that using the same shape distribution and refractive index cannot achieve improvements for all three samples. Unfortunately, AGLSD did not measure sample mineralogy and morphology, limiting our ability to test this hypothesis.

5.4.2 Evaluating the linear depolarization ratio and the lidar ratio

Passive ground-based (e.g., AERONET) and satellite remote sensing products (e.g., MISR) need an accurate scattering matrix to retrieve the properties of aggregate dust aerosols in the atmospheric column (Section 5.4.1), whereas active remote sensing products need accurate linear depolarization ratio and lidar ratio to separate dust from other aerosol types in the vertical profiles and to retrieve height-resolved dust properties (*Burton et al.*, 2012).

The lidar ratio (also referred to as the extinction-to-backscatter ratio) quantifies the ratio between the aerosol extinction and backscatter coefficients. The value of the lidar ratio needs to be prescribed in retrievals of elastic backscatter lidars (like the CALIOP instrument;

Winker et al. (2007)), since these lidars cannot simultaneously measure the aerosol extinction and backscatter coefficients. The CALIOP retrieval assumes a spatially homogeneous value of the lidar ratio (~ 40 sr in general) for dust layers (*Omar et al.*, 2009; *Burton et al.*, 2012), but in field observations, the lidar ratio of dust aerosols vary substantially in space (*Ansmann et al.*, 2012; *Burton et al.*, 2012; *Müller et al.*, 2012; *Amiridis et al.*, 2015; *Tesche et al.*, 2019).

The linear depolarization ratio quantifies aerosols' ability to polarize incident laser light. Remote sensing measurements of the linear depolarization ratio can effectively separate aspherical particles from spherical ones, since spherical particles have a linear depolarization ratio of zero, whereas aspherical particles have a linear depolarization ratio greater than zero; this occurs because spherical particles do not depolarize incident laser light, but aspherical particles do (*Liou*, 2002). Furthermore, the value of the linear depolarization ratio can effectively separate dust from other aerosol types, since dust aerosols tend to have the largest values of linear depolarization ratio than other aerosol types (*Sakai et al.*, 2010; *Ansmann et al.*, 2012; *Burton et al.*, 2012). Indeed, a range of laboratory and field observations have found that the linear depolarization ratio of dust plumes is within the range of 0.2 to 0.4 (Figure 5.7; *Tesche et al.* (2019)).

Here, we combine the ellipsoidal dust optics with the globally representative size distribution (*Adebisi and Kok*, 2020) and shape distributions (*Huang et al.* (2020); Section 5.2.1) of dust aerosols to predict the linear depolarization ratio and the lidar ratio. We then compare the predicted values with field and laboratory observations to evaluate the performance of ellipsoid optics.

We find that the ellipsoid optics can predict the magnitude and the wavelength dependence of the linear depolarization ratio in excellent agreement with measurements (Figure 5.10). Field observations have found that the linear depolarization ratio is ~ 0.25 at the wavelength of 355 nm, increases to ~ 0.35 at the wavelength of 710 nm, and then decreases to ~ 0.30 at the wavelength of 1064 nm. The ellipsoid optics excellently reproduce the magnitude and the trend that the linear depolarization ratio increases with wavelength up to ~ 700

nm, and then remains constant or slightly decreases with wavelength. The ellipsoidal optics show improved agreement with observations relative to spheroid optics. The spheroid optics used in AERONET retrievals (*Müller et al.*, 2010; *Shin et al.*, 2018) predicted the linear depolarization ratio to keep increasing with wavelength, which disagrees with the observations; in addition, the predicated values of the linear depolarization ratios are 30% smaller than observations at almost all wavelengths. Furthermore, an independent study (i.e., *Wiegner et al.* (2009)) that also assumed dust as spheroidal particles but used different shape distributions and spheroidal optics kernel found a similar increasing trend with wavelength and a similar magnitude of the linear depolarization ratio. This indicates that the spheroid optics cannot adequately represent the wavelength-dependent linear depolarization ratio of atmospheric dust particles. Instead, the ellipsoid optics enables improved agreement with observations, suggesting a strong potential to apply ellipsoid optics in future lidar retrievals.

Although the ellipsoid optics can reproduce the linear depolarization ratio, it overestimates the magnitude of the lidar ratio. The ellipsoid optics predicts the value of the lidar ratio to be in the range of 100 to 120 sr, which is a factor of ~ 2 to 3 larger than the range of 40 to ~ 80 sr found in field measurements (Figure 5.11) (*Ansmann et al.*, 2012; *Burton et al.*, 2012; *Müller et al.*, 2012; *Amiridis et al.*, 2015; *Tesche et al.*, 2019). This occurs because the ellipsoid optics underestimate the phase function at 180 degree relative to laboratory measurements (Figures 5.4, 5.5, and 5.6). Compared to simulations of ellipsoid optics and spheroid optics, laboratory measurements show a significantly larger backward scattering (Figures 5.4, 5.5, and 5.6), possibly because of the surface roughness and sharp corners of the dust particles, which are not accounted for by either spheroid or ellipsoid optics (*Gasteiger et al.*, 2011; *Kemppinen et al.*, 2015; *Kahnert et al.*, 2020). Indeed, several studies found that increasing roughness in their simulations increased the simulated lidar ratio (*Gasteiger et al.*, 2011; *Kemppinen et al.*, 2015). This finding indicates that a realistic quantification of dust body shape is not sufficient and that an accurate quantification of dust surface texture is critical to accurately reproduce the lidar ratio.

5.5 Discussions and Conclusions

To improve models and retrieval algorithms in terms of dust shape quantification, here we investigate for the first time whether accounting for realistic dust shape distributions enables improved single-scattering properties. To do so, we first approximate desert dust as tri-axial ellipsoids (Figure 3.5) and use globally representative shape distributions (Figure 3.2) from a measurement compilation (Section 5.2.1). We then combine this shape distribution and the shape-resolved single-scattering database to obtain globally representative single-scattering properties of ellipsoidal dust ensembles (Section 5.2.2). We obtain results of the scattering angle-independent single-scattering properties used in global aerosol models (Section 5.3) and the scattering angle-dependent single-scattering properties used in remote sensing retrievals (Section 5.4). We find that neglecting the asphericity of dust and approximating dust as spherical particles underestimates the extinction efficiency, the mass extinction efficiency, the asymmetry factor, and the single-scattering albedo for all dust sizes at both shortwave and longwave spectrum (Figure 5.1; Tables 5.2 and 5.3), since all global aerosol models included in the AeroCom phase III project approximate dust as spheres (Table 5.1). In addition, we find that the retrieval algorithms of most passive and active remote sensing products approximate dust as spheroids with a prescribed shape distribution that substantially underestimates dust asphericity (Figure 5.3). We evaluate the spheroid optics used in retrieval algorithms and our newly developed ellipsoid optics against laboratory measurements of the scattering matrices of three samples (Figure 5.2) and field observations of the linear depolarization ratio and the lidar ratio. We find that although the ellipsoid optics can reproduce the scattering matrix in excellent agreement with the laboratory-measured scattering matrix of the feldspar sample (Figures 5.4 and 5.7), it does not show improved agreement relative to spheroid optics in reproducing the scattering matrix of two dust samples (Figures 5.5, 5.6, 5.8, and 5.9). In particular, ellipsoid optics underestimate backscattering relative to measurements and more spherical optics. Furthermore, we find that although the ellipsoid optics can reproduce the magnitude and the wavelength dependence of the linear depolarization ratio in an excellent

agreement with field measurements (Figure 5.10), it overestimates the lidar ratio by a factor of ~ 2 to 3 (Figure 5.11) due to an underestimation in the magnitude of the backscattered light.

Our results are subject to a few important limitations. First, due to the range limitation of *Meng et al. (2010)*, we cannot obtain dust optics with a height-to-width ratio less than 0.3. For dust extracted from the lognormal distribution of HWR with an HWR less than 0.3, we take its single-scattering properties as the single-scattering properties of dust with the same geometric diameter, but with HWR=0.3. As such, we may underestimate the effect of highly aspherical dust on the optics of ellipsoidal dust ensembles. Second, the size distributions of the three samples of the Amsterdam-Granada light scattering database were measured by the laser particle sizers (*Muñoz et al., 2012; Gómez Martín et al., 2021*), and thus these size distributions are in terms of optical diameter. However, models and retrieval algorithms require volume-equivalent diameter, and a significant difference exists between the optical diameter and the volume-equivalent diameter of aspherical dust particles (*Huang et al., 2021*). We cannot correct the measured diameters due to a lack of information in the parameters of the laser particle sizers (including the wavelength of the sensor’s emitter and the scattering angle range of the sensor’s detector mirror) and in the microphysical properties of the samples (including mineralogy and morphology).

These results have several important implications. First, the effect of dust shape and shape distribution on dust radiative effects can be larger than previously thought. *Räisänen et al. (2013)* used *Dubovik et al. (2006)*’s spheroid optics and found that the dust shortwave radiative forcing of spheroidal dust did not differ much from that of volume-equivalent spherical dust at both the top of the atmosphere and the surface (by 3% to 4%). However, *Yi et al. (2011)* used ellipsoidal dust shape with a similar shape distribution as *Räisänen et al. (2013)* and found that the effect of different dust shapes can cause a difference in the dust shortwave radiative forcing at the top of the atmosphere by 30%. Although *Yi et al. (2011)* is more advanced than *Räisänen et al. (2013)* in terms of dust shape, neither study considered

the realistic shape distribution, since their shape distributions were taken as the one that enables a best fit between the simulated and laboratory-measured dust optics instead of the shape distribution from measurements. As such, accounting for realistic shape distribution can enable improved quantifications of the dust direct radiative effect.

Second, our finding that neither the global aerosol models nor the retrieval algorithms of remote sensing products have accounted for realistic dust shape and shape distribution highlights the importance of model and algorithm developments. The errors in the single-scattering properties can propagate in the simulated and retrieved dust distributions and the estimated dust effects. Indeed, the recent AeroCom phase III intercomparison project found that the global dust emission differs by a factor of 7, the dust burden differs by a factor of 4, and the mass extinction efficiency differs by a factor of 4 among the multi-model ensembles (Gliß et al., 2021). Accounting for realistic dust shape and shape distribution in models and retrievals can be a key step towards improved estimations of dust distributions and dust effects.

Acknowledgements. Y. Huang acknowledges the financial support by the National Aeronautics and Space Administration (NASA) grant 80NSSC19K1346, awarded under the Future Investigators in NASA Earth and Space Science and Technology (FINESST) program. J. F. Kok acknowledges the support by the National Science Foundation (NSF) grants 1552519 and 1856389, and the Army Research Office under Cooperative Agreement Number W911NF-20-2-0150. The views and conclusions contained in this manuscript are those of the authors and should not be interpreted as representing the official policies, either expressed or implied, of the Army Research Office or the US Government. The US Government is authorized to reproduce and distribute reprints for Government purposes notwithstanding any copyright notation herein. The authors thank Oleg Dubovik for providing the kernel of the spheroidal dust optics, thank Bingqi Yi for providing the interpolation code of the

Meng et al. (2010)’s database of the ellipsoidal dust optics, and thank Matthias Tesche for providing his compilation data on the linear depolarization ratio. In addition, the authors thank Ping Yang, Masanori Saito, Yu Gu, and Kuo-Nan Liou for insightful discussions.

5.6 Tables and figures

Table 5.1: Dust shape approximations used in current global aerosol models. The 14 global aerosol models are used in the AeroCom phase III intercomparison project (Gliß et al., 2021). All of them approximate dust as spheres.

Model names	Dust shape in models	References
CAM5-ATRAS	Sphere	Matsui and Mahowald (2017)
EC-Earth3-AerChem	Sphere	van Noije et al. (2020)
ECHAM-HAM	Sphere	Tegen et al. (2019)
ECHAM-SALSA	Sphere	Kokkola et al. (2018)
ECMWF-IFS	Sphere	Rémy et al. (2019)
EMEP-MS-CW	Sphere	Simpson et al. (2012)
GFDL-AM4	Sphere	Zhao et al. (2018)
GISS-OMA	Sphere	Miller et al. (2006); Bauer et al. (2020)
GOCART	Sphere	Chin et al. (2010)
INCA	Sphere	Balkanski et al. (2004)
MIROC-SPRINTARS	Sphere	Takemura et al. (2005)
NorESM2	Sphere	Kirkevåg et al. (2018)
OsloCTM3	Sphere	Lund et al. (2018)
TM5	Sphere	van Noije et al. (2014)

Table 5.2: Comparisons between single-scattering properties of ellipsoidal dust (denoted as “ellipsoid”) and those of spherical dust (denoted as “sphere”) at the wavelength of 550 nm. The refractive index of dust aerosols is taken the same for both shape approximations as $1.53 \pm 0.03 - 10^{-2.75 \pm 0.25} i$, which covers the range of *Di Biagio et al.* (2019). The values in parentheses denote the 95% confidence interval. The errors in single-scattering properties are propagated from errors in dust refractive index for spherical dust, and from errors in dust refractive index and the parameters of the lognormal distributions of the shape descriptors for ellipsoidal dust (see Section 5.2.1).

Volume-equivalent diameter, μm	Extinction efficiency, Q_{ext}		Mass extinction efficiency, MEE		Single-scattering albedo, SSA		Asymmetry factor, g	
	Ellipsoid	Sphere	Ellipsoid	Sphere	Ellipsoid	Sphere	Ellipsoid	Sphere
0.2	0.61 (0.41, 0.93)	0.38 (0.31, 0.47)	1.83 (1.19, 2.89)	1.15 (0.88, 1.50)	0.98 (0.95, 0.99)	0.98 (0.95, 0.99)	0.29 (0.27, 0.31)	0.27 (0.26, 0.28)
0.5	3.91 (3.25, 4.72)	3.56 (3.07, 3.86)	4.69 (3.68, 6.01)	4.24 (3.46, 5.14)	0.99 (0.98, 1.00)	0.99 (0.98, 1.00)	0.72 (0.71, 0.74)	0.73 (0.70, 0.75)
1	5.10 (4.94, 5.28)	2.96 (2.33, 3.26)	3.06 (2.63, 3.63)	1.75 (1.31, 2.18)	0.98 (0.96, 0.99)	0.98 (0.93, 0.99)	0.75 (0.70, 0.78)	0.58 (0.50, 0.71)
2	3.59 (3.45, 3.77)	2.61 (1.94, 2.95)	1.08 (0.93, 1.29)	0.79 (0.57, 1.00)	0.94 (0.89, 0.98)	0.96 (0.86, 0.98)	0.72 (0.69, 0.75)	0.76 (0.66, 0.81)
5	3.26 (3.16, 3.38)	2.24 (2.02, 2.42)	0.39 (0.34, 0.46)	0.27 (0.22, 0.33)	0.89 (0.81, 0.96)	0.90 (0.78, 0.96)	0.82 (0.78, 0.86)	0.80 (0.76, 0.85)
10	2.99 (2.91, 3.09)	2.16 (2.05, 2.22)	0.18 (0.15, 0.21)	0.13 (0.11, 0.15)	0.83 (0.73, 0.92)	0.84 (0.68, 0.93)	0.85 (0.81, 0.91)	0.84 (0.80, 0.90)
20	2.82 (2.75, 2.91)	2.09 (2.05, 2.12)	0.08 (0.07, 0.10)	0.06 (0.05, 0.07)	0.76 (0.64, 0.86)	0.74 (0.59, 0.87)	0.88 (0.84, 0.94)	0.88 (0.84, 0.93)
50	2.68 (2.62, 2.76)	2.05 (2.03, 2.06)	0.03 (0.03, 0.04)	0.02 (0.02, 0.03)	0.66 (0.57, 0.75)	0.60 (0.55, 0.74)	0.92 (0.89, 0.95)	0.93 (0.88, 0.95)

Table 5.3: Comparisons between single-scattering properties of ellipsoidal dust (denoted as “ellipsoid”) and those of spherical dust (denoted as “sphere”) at the wavelength of 10 μm . The refractive index of dust aerosols is taken the same for both shape approximations as $1.70 \pm 0.20 - 10^{-0.40 \pm 0.11}i$, which covers the ranges of *Volz* (1972, 1973); *Hess et al.* (1998); *Di Biagio et al.* (2017). The values in parentheses denote the 95% confidence interval. The errors in single-scattering properties are propagated from errors in dust refractive index for spherical dust, and from errors in dust refractive index and the parameters of the lognormal distributions of the shape descriptors for ellipsoidal dust (see Section 5.2.1).

Volume-equivalent diameter, μm	Extinction efficiency, Q_{ext}		Mass extinction efficiency, MEE		Single-scattering albedo, SSA		Asymmetry factor, g	
	Ellipsoid	Sphere	Ellipsoid	Sphere	Ellipsoid	Sphere	Ellipsoid	Sphere
0.2	0.07 (0.04, 0.09)	0.04 (0.02, 0.07)	0.20 (0.11, 0.29)	0.13 (0.07, 0.20)	6.76E-5 (2.72E-5, 2.40E-4)	2.07E-4 (9.60E-5, 4.90E-4)	1.1E-3 (1.00E-3, 1.20E-3)	8.68E-4 (7.26E-4, 1.00E-3)
0.5	0.17 (0.10, 0.24)	0.11 (0.06, 0.17)	0.21 (0.12, 0.29)	0.13 (0.07, 0.20)	4.00E-3 (2.10E-3, 8.40E-3)	3.20E-3 (1.50E-3, 7.50E-3)	6.30E-3 (5.90E-3, 6.70E-3)	5.40E-3 (4.50E-3, 6.50E-3)
1	0.37 (0.22, 0.48)	0.23 (0.13, 0.34)	0.22 (0.13, 0.31)	0.14 (0.08, 0.21)	0.03 (0.02, 0.06)	0.02 (0.01, 0.05)	0.02 (0.02, 0.03)	0.02 (0.02, 0.03)
2	0.98 (0.64, 1.19)	0.61 (0.41, 0.78)	0.29 (0.18, 0.38)	0.18 (0.11, 0.25)	0.16 (0.08, 0.29)	0.14 (0.07, 0.27)	0.10 (0.09, 0.10)	0.09 (0.07, 0.11)
5	3.17 (2.12, 4.31)	2.51 (1.55, 3.29)	0.38 (0.25, 0.54)	0.29 (0.18, 0.41)	0.44 (0.31, 0.59)	0.44 (0.31, 0.59)	0.54 (0.51, 0.56)	0.55 (0.51, 0.58)
10	4.20 (3.34, 4.72)	2.84 (2.46, 3.13)	0.25 (0.19, 0.31)	0.17 (0.14, 0.21)	0.51 (0.42, 0.58)	0.47 (0.43, 0.54)	0.79 (0.75, 0.81)	0.79 (0.73, 0.82)
20	3.93 (3.70, 4.13)	2.51 (2.43, 2.55)	0.12 (0.10, 0.14)	0.07 (0.06, 0.09)	0.51 (0.49, 0.53)	0.48 (0.47, 0.51)	0.86 (0.82, 0.90)	0.87 (0.84, 0.90)
50	3.47 (3.38, 3.61)	2.30 (2.26, 2.30)	0.04 (0.04, 0.05)	0.03 (0.02, 0.03)	0.51 (0.50, 0.52)	0.53 (0.51, 0.55)	0.89 (0.85, 0.93)	0.90 (0.87, 0.94)

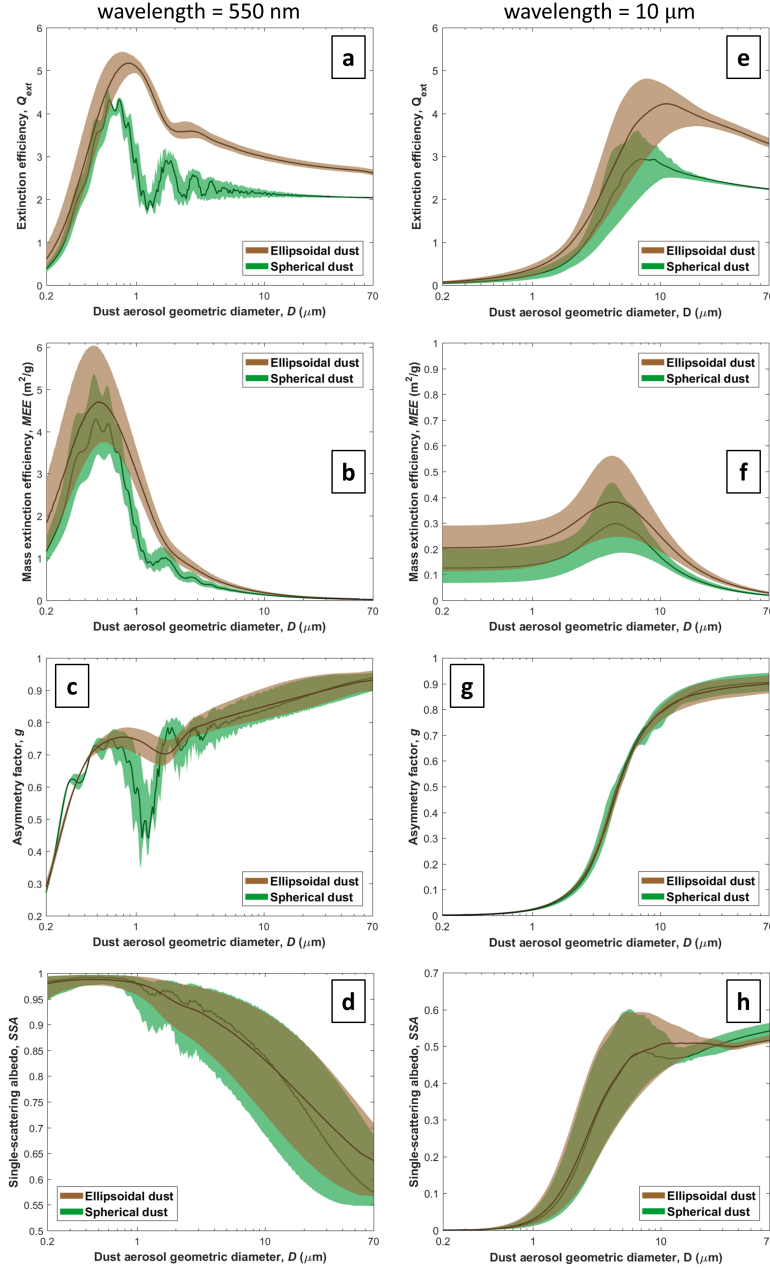


Figure 5.1: Single-scattering properties of spherical and ellipsoidal dust in the shortwave and longwave spectra. Left column includes: (a) extinction efficiency, (b) mass extinction efficiency, (c) asymmetry factor, and (d) single-scattering albedo, at a wavelength of 550 nm. Right column includes these variables at 10 μm . The refractive index of dust aerosols is $1.53 \pm 0.03 - 10^{-2.75 \pm 0.25}i$ at 550 nm and $1.70 \pm 0.20 - 10^{-0.40 \pm 0.11}i$ at 10 μm . Values at geometric diameters of 0.2, 0.5, 1, 2, 5, 10, 20, and 50 μm are detailed in Table 5.2 at 550 nm and Table 5.3 at 10 μm .

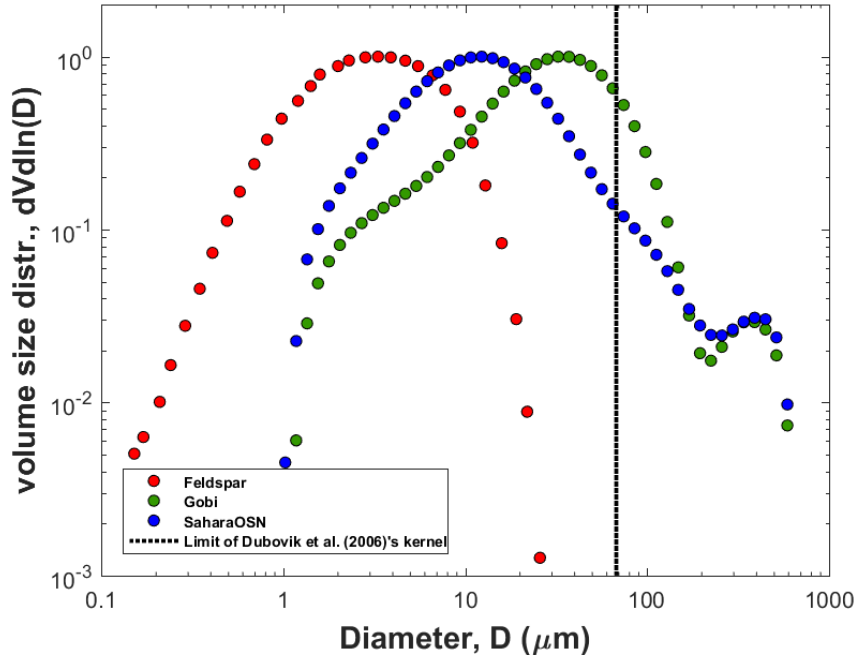


Figure 5.2: Size distributions of the feldspar sample and two dust samples included in the Amsterdam-Granada Light Scattering Database (AGLSD). The size distributions were measured using a laser particle sizer (model Mastersizer 2000) with water as dispersive medium (*Gómez Martín et al., 2021*). The black dotted line denotes the upper limit (i.e., $67.8 \mu\text{m}$ in diameter) of dust size range in *Dubovik et al. (2006)*'s kernel, which is the most widely used database in remote sensing retrievals. In Section 5.4.1, we only use the size distributions at $D \leq 67.8 \mu\text{m}$ when using both *Dubovik et al. (2006)*'s kernel and the single-scattering database of ellipsoidal dust (*Meng et al., 2010*) (see Section 5.2.2) for consistency. Among the three samples (i.e., feldspar, Gobi, and SaharaOSN), only feldspar is fully within the size range limit.

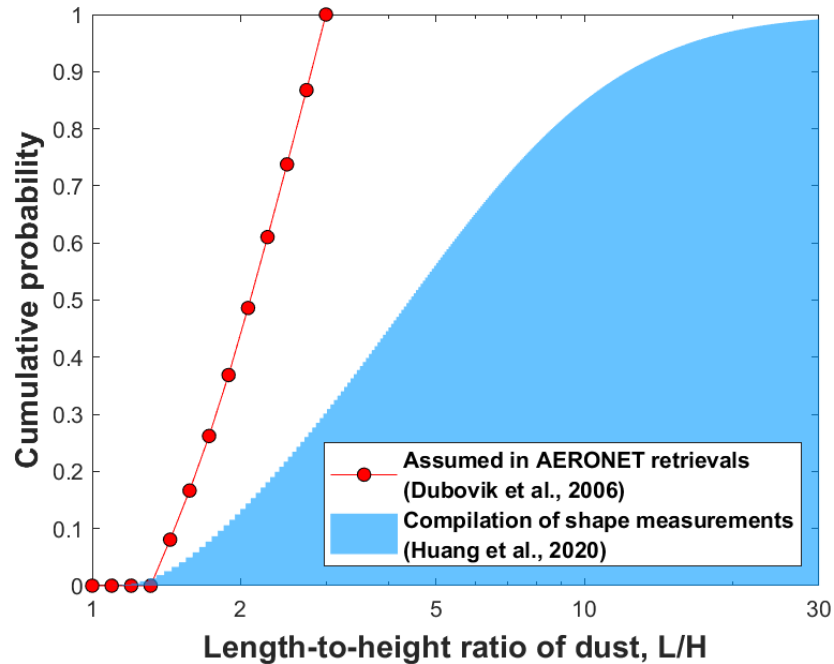


Figure 5.3: A comparison between the cumulative probability distribution of dust length-to-height ratio used in the retrieval algorithms of AERONET and from a measurement compilation. Both the retrieval algorithms (*Dubovik et al., 2006*) and the measurement compilation (*Huang et al., 2020*) (see Section 5.2.1) assume that dust shape is invariant with dust size. AERONET’s retrieval algorithms use this size-invariant cumulative probability distribution (red line with markers) by default for retrievals of dust properties. This default shape distribution is used not only in version 2 and version 3 retrieval algorithms of AERONET, but also in the new Deep Blue algorithm (*Hsu et al., 2019*) and a developing retrieval algorithm for lidar observations (*Tesche et al., 2019*). The cumulative probability distribution used in retrieval algorithms substantially underestimates dust asphericity relative to measurement of dust asphericity.

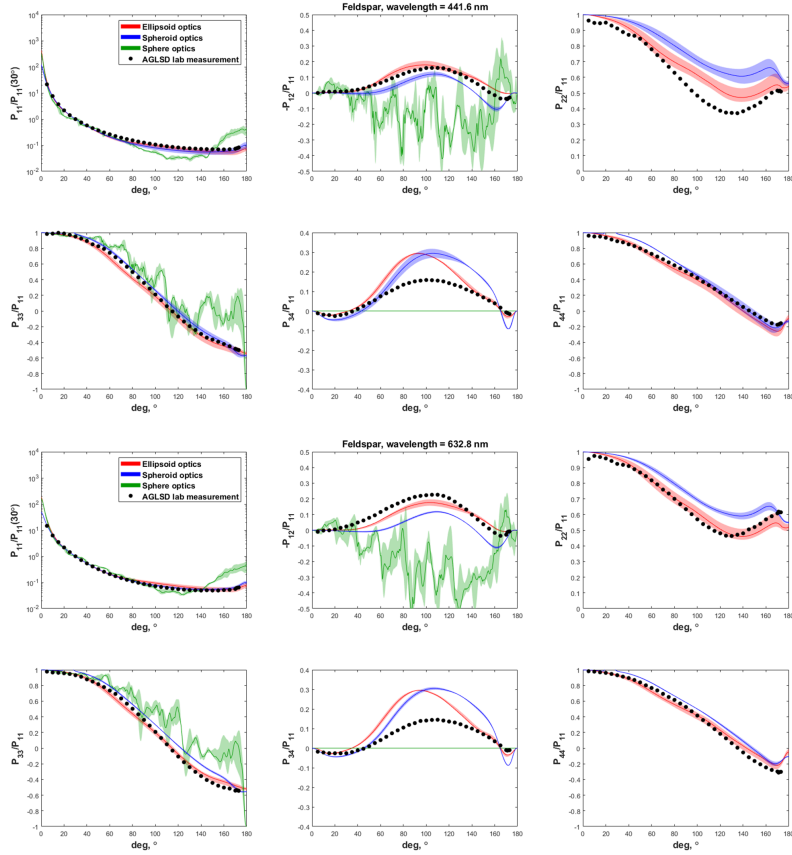


Figure 5.4: Comparisons between the six non-zero elements of the laboratory-measured scattering matrix of a sample of crushed feldspar rock with three types of simulations at two wavelengths (441.6 and 632.8 nm). The three types of simulations include (1) “Ellipsoid optics” (red line) that combines AGLSD samples’ size distributions, *Meng et al.* (2010)’s database of ellipsoidal dust optics, and *Huang et al.* (2020)’s compiled lognormal distributions of AR and HWR; (2) “Spheroid optics” (blue line) that combines AGLSD samples’ size distributions, *Dubovik et al.* (2006)’s kernel of spheroidal dust optics, and *Dubovik et al.* (2006)’s averaged retrieved distribution of aspect ratio; and (3) “Sphere optics” (green line) that combines AGLSD samples’ size distributions and spherical dust optics calculated by Lorenz-Mie theory. For all three types of simulations, the refractive index is taken as $1.53 \pm 0.03 - 10^{-2.75 \pm 0.25}i$ (same as Fig. 5.1 and Table 5.2) at both 441.6 and 632.8 nm. The shaded ranges denote uncertainties propagated from the refractive index.

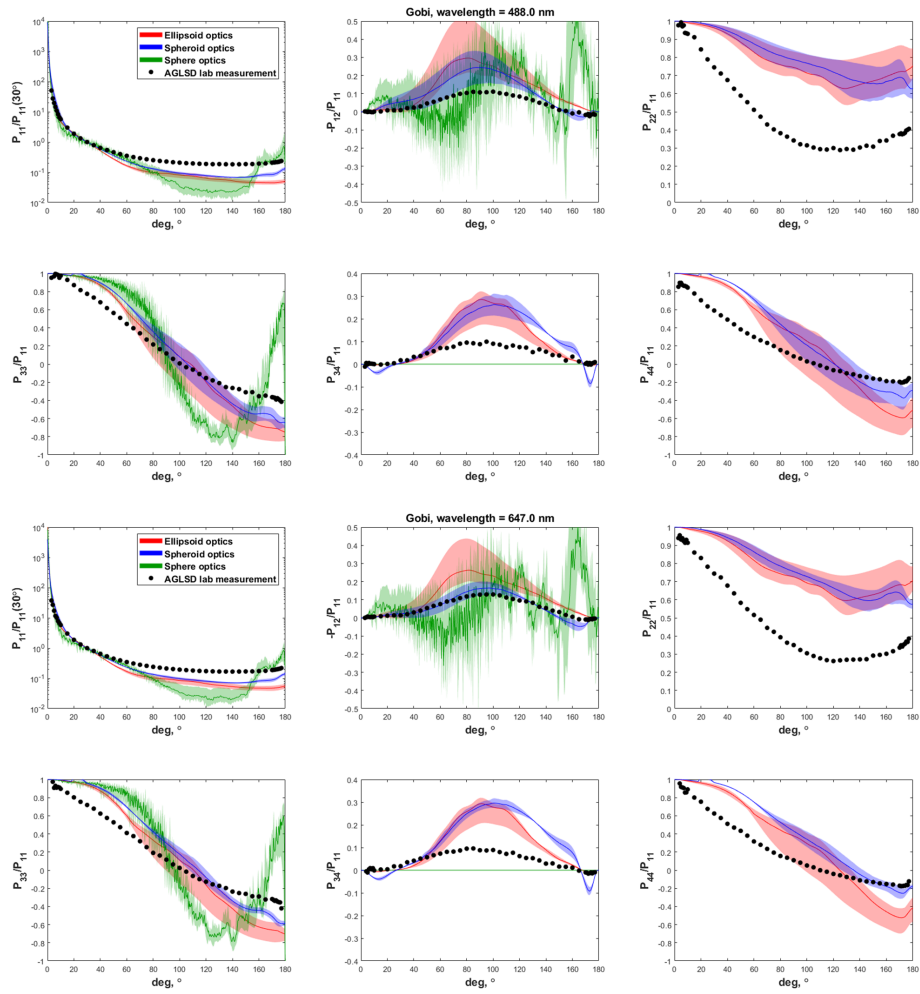


Figure 5.5: Same as Fig. 5.4 but for dust sample Gobi.

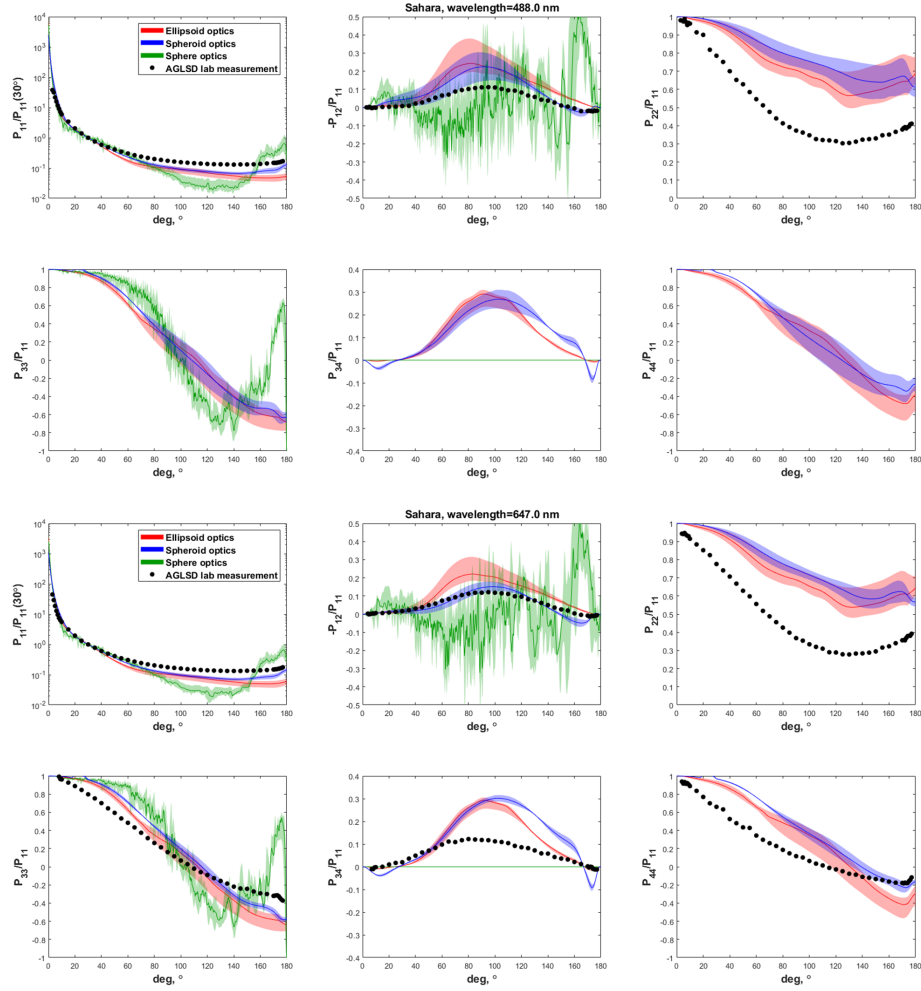


Figure 5.6: Same as Figs. 5.4 and 5.5 but for dust sample SaharaOSN. Note that laboratory measurements of P_{33}/P_{11} , P_{34}/P_{11} , and P_{44}/P_{11} at the wavelength of 488 nm are not available due to sensor issues (see *Gómez Martín et al. (2021)*).

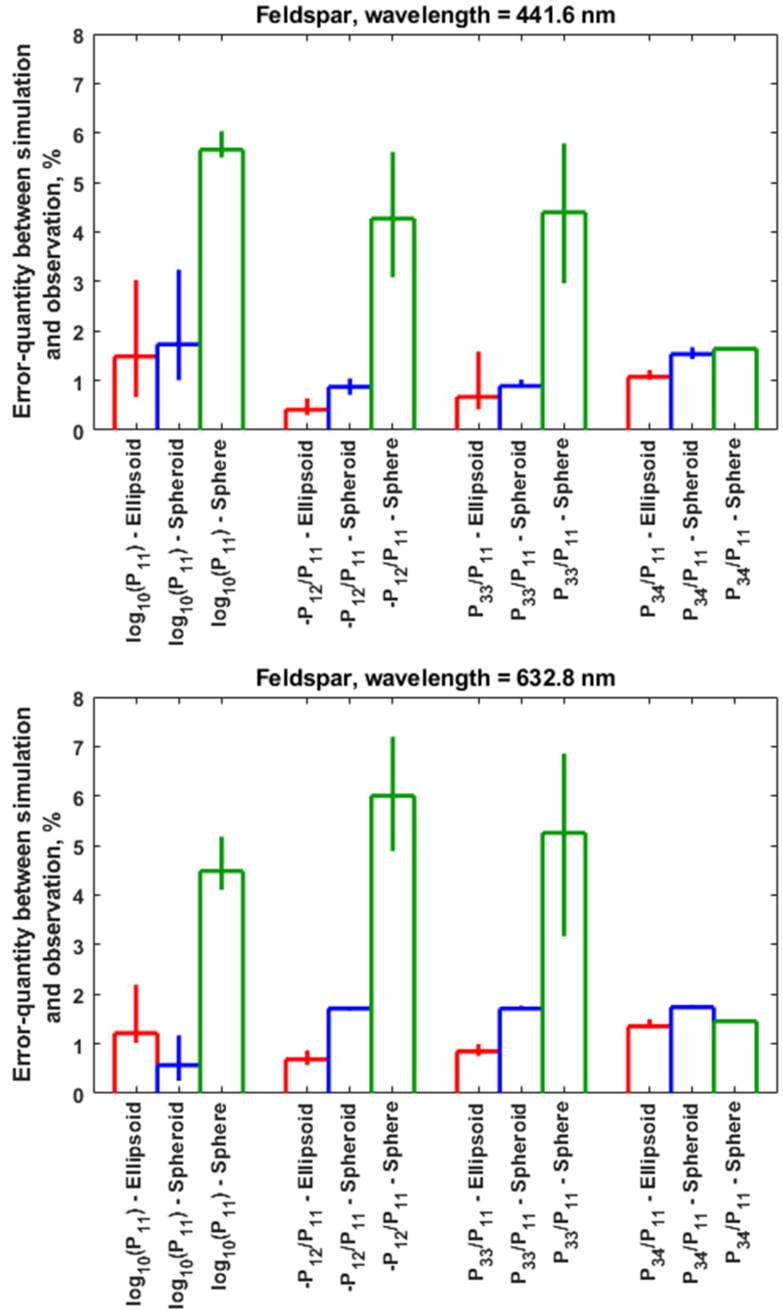


Figure 5.7: Error-quantity between the three types of simulations (ellipsoid, spheroid, and sphere optics) and the laboratory observations for sample feldspar at two wavelengths (441.6 and 632.8 nm). The error bars denote uncertainties propagated from the dust refractive index (see the caption of Fig. 5.4). Ellipsoid and spheroid optics show significantly improved agreement with observations than sphere optics. Ellipsoid optics show significantly improved agreement with observations than spheroid optics.

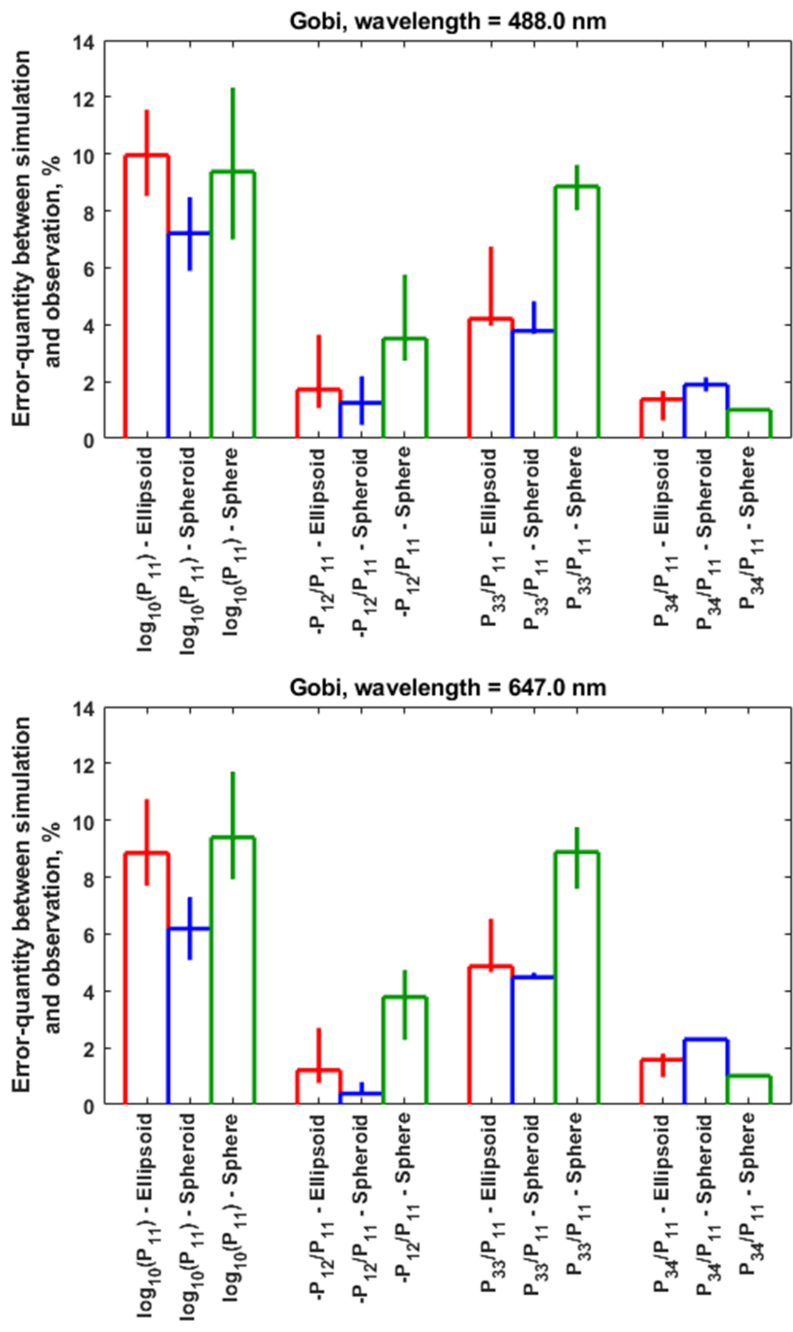


Figure 5.8: Same as Fig. 5.7 but for dust sample Gobi.

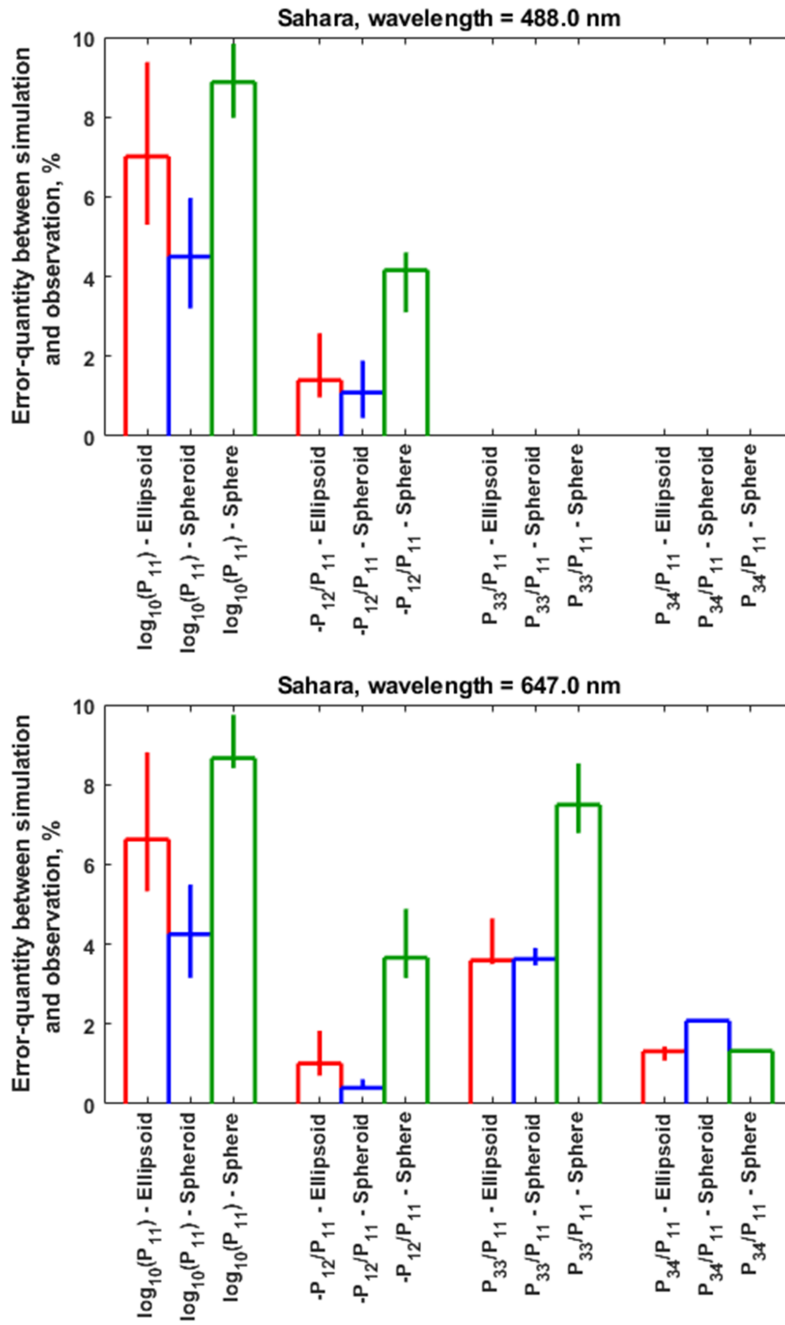


Figure 5.9: Same as Figs. 5.7 and 5.8 but for dust sample SaharaOSN. Note that laboratory measurements of P_{33}/P_{11} , P_{34}/P_{11} , and P_{44}/P_{11} at the wavelength of 488 nm are not available due to sensor issues (see Gómez Martín et al. (2021)).

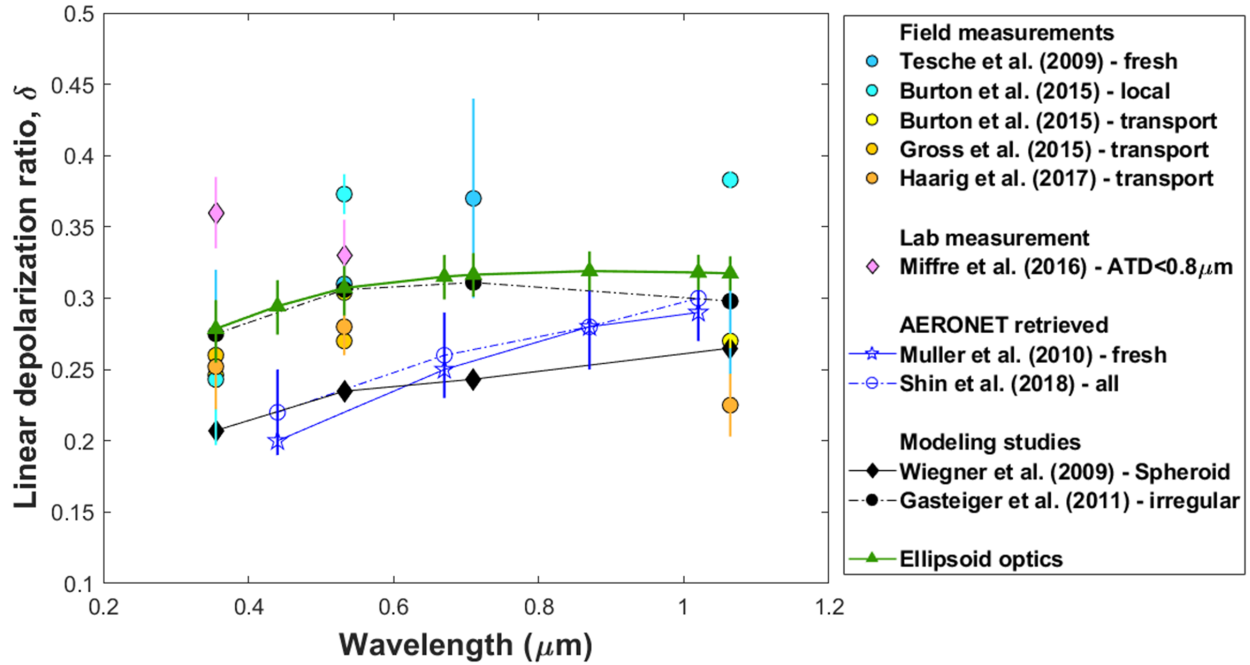


Figure 5.10: Wavelength dependence of the linear depolarization ratio of dust aerosols. Shown are the results at 4 wavelengths where field and laboratory observations of the linear depolarization ratio were taken (i.e., 355, 532, 710, 1064 nm) and at the 4 wavelengths of AERONET retrievals (i.e., 440, 670, 870, 1020 nm). The data compilation is after Fig. 1 of *Tesche et al.* (2019). The measurement compilation shows that the linear depolarization ratio peaks at 0.3 around the wavelength of 600 nm. Spheroid optics used in AERONET and an independent study (*Wiegner et al.*, 2009) cannot reproduce the magnitude or the wavelength dependence of the linear depolarization ratio, whereas the ellipsoid optics can excellently reproduce that.

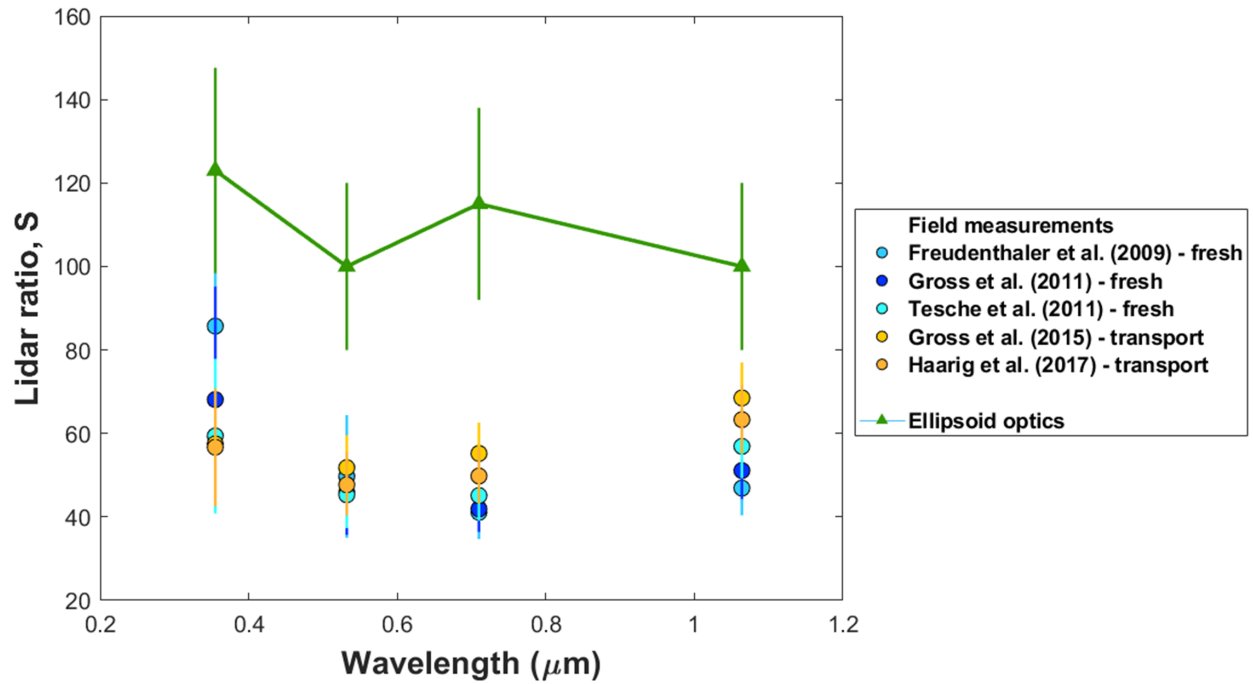


Figure 5.11: Wavelength dependence of the lidar ratio of dust aerosols. Shown are the results at four wavelengths where field observations of the lidar ratio were taken (i.e., 355, 532, 710, 1064 nm). The data compilation is taken after Fig. 4 of *Saito and Yang (2021)*. The simulation "ellipsoid optics" combines the shape-resolved single-scattering properties of ellipsoidal dust (*Meng et al., 2010*), the globally representative dust shape distributions (*Huang et al., 2020*), and the globally representative size distribution of dust aerosols (*Adebisi and Kok, 2020*). Results show that the ellipsoid optics overestimate dust lidar ratio by a factor of ~ 2 to 3 at all four wavelengths.

CHAPTER 6

Final conclusions and future work

6.1 Final conclusions

Desert dust is the dominant aerosol type by mass in the atmosphere (*IPCC AR5*, 2013). Throughout the dust cycle (including dust emission, short- and long-range transport, and deposition; *Shao et al.* (2011b)), dust produces important effects on the Earth system. First, dust absorbs and scatters both shortwave and longwave radiations, thereby modulating the Earth’s energy budget directly (*Kok et al.*, 2017). Second, dust acts as nuclei for cloud droplets and ice crystals, thereby modifying cloud microphysical properties and affecting the energy budget indirectly (*DeMott et al.*, 2015). Third, dust carries key nutrients (i.e., iron and phosphorus), and its deposition to the downwind ocean and land boosts primary productivity and carbon sequestration (*Yu et al.*, 2015; *Ito et al.*, 2019). In this way, dust aerosols affect the carbon cycle and associated climate feedbacks. Furthermore, dust aerosols impact anthropogenic activities, including by depleting renewable energy generation (*Piedra and Moosmüller*, 2017), degrading regional air quality and visibility (*Mahowald et al.*, 2007), and producing hazards to human health (*Burnett et al.*, 2014).

These varied impacts above depend sensitively on dust microphysical properties, especially dust size and shape. The overall effect of the fine dust cools the Earth system by scattering shortwave radiation, whereas coarse dust net warms the system by also absorbing both shortwave and longwave radiation (*Kok et al.*, 2017). In addition, dust asphericity increases aerodynamic drag force at a given volume and mass, causing aspherical dust to have a longer lifetime in the atmosphere than volume-equivalent spherical dust (*Yang et al.*, 2013;

Huang et al., 2020). Aspherical dust also differs from volume-equivalent spherical dust in the angular and the wavelength dependencies of single-scattering properties (*Dubovik et al.*, 2006; *Nousiainen and Kandler*, 2015). As such, accurate knowledge of dust shape and size is key to, for instance, accurate estimates of dust deposition fluxes, spatial and temporal distributions, and direct radiative effects at both regional and global scales.

Although accurate quantifications of dust shape and size are thus important for calculating dust impacts, current representations of dust shape and size in global aerosol models and remote sensing retrievals conflict with in situ measurements. Specifically, models and retrieval algorithms lack a consistent quantification of dust shape (*Kalashnikova et al.*, 2005; *Dubovik et al.*, 2006; *Mahowald et al.*, 2014); their quantifications are inaccurate relative to measurements of dust shape (*Huang et al.*, 2020). In addition, models and retrieval algorithms substantially underestimate the abundance of coarse dust in the atmosphere relative to measurements (*Ryder et al.*, 2019; *Adebiyi and Kok*, 2020). During the validation process, measurements are treated as the "ground truth" in general; however, measurements of size distributions can be problematic because they are based on different diameter types that do not account for realistic dust shapes (*Huang et al.*, 2021). Furthermore, measurements of emitted dust size distributions are not available for some major soil types (e.g., active sands), making the validation process for these regions difficult. The resulting biases in dust shape and size can propagate into dust optical properties used in models and retrieval algorithms, which further contributes to inaccurate estimates of dust effects on the Earth system. In this dissertation, I address the above issues in the following chapters.

In Chapter 2, I present the first (to my knowledge) in situ field measurements of the size distributions of emitted dust from active sands, which cover 20% of arid lands worldwide (*Huang et al.*, 2019). I conducted field measurements of dust emission under natural aeolian saltation from coastal Oceano Dunes in California as well as laboratory analyses on the topsoil sand samples. I found that dust emission from active sands differs from dust emission from non-sandy soils not only in the size distribution of emitted dust, but also in the magnitude

of dust emission flux, the magnitude and the shear velocity dependence of the sandblasting efficiency, and the mineralogical composition of the emitted dust. This work improves the understanding on the physical processes that drive dust emission from active sands, and suggests important implications of dust emission from active sands for downwind human health, park management, the hydrological cycle, and climate.

In Chapter 3, I present a globally representative parameterization of dust shape from a measurement compilation (*Huang et al.*, 2020). I compiled dozens of measurements of dust shape descriptors across the globe. I found that at the regional scale, North African dust becomes more aspherical during transport, whereas Asian dust might become less aspherical. At the global scale, the longest dimension (dust length) is on average five times larger than the smallest dimension (dust height), and current climate models and remote sensing retrievals underestimate this dust asphericity (i.e., dust length divided by its height) by a factor of $\sim 3 - 5$. Accounting for realistic dust asphericity increases gravitational settling lifetime by $\sim 20\%$, which helps explain the underestimation of coarse dust transport by models. This work points out the direction for future improvements with regard to dust shape in global aerosol models and the retrieval algorithms of remote sensing products.

In Chapter 4, I harmonize the measurements of dust size distributions that are based on four different types of diameters (including the geometric, aerodynamic, optical, and projected area-equivalent diameters) (*Huang et al.*, 2021). I obtained conversions between these different diameter types that account for dust asphericity. Even for the same dust particle, these diameter types are highly different from each other, suggesting the importance of diameter standardization in the dust research community. I then used these diameter conversions to obtain a consistent observational constraint on the size distribution of emitted dust. This observational constraint is substantially coarser than parameterizations used in global aerosol models, which underestimate the mass of emitted dust with a diameter in between 10 to 20 μm by a factor of ~ 2 and usually do not account for the substantial dust emissions larger than 20 μm in diameter. This work suggests that models substantially

underestimate coarse dust emission, which helps explain the underestimation of coarse dust transport by models (*Adebiyi and Kok, 2020*).

In Chapter 5, I for the first time account for a realistic dust shape distribution in obtaining single-scattering properties of dust aerosols. I found that neglecting the asphericity of dust and approximating dust as spherical particles underestimates the extinction efficiency, the mass extinction efficiency, the asymmetry factor, and the single-scattering albedo for all dust sizes at both shortwave and longwave spectra, since global aerosol models approximate dust as spheres. In addition, I found that the inaccurate quantification of dust shape in retrieval algorithms causes them to generate an incorrect magnitude and wavelength dependence of the linear depolarization ratio relative to observations. The newly-developed ellipsoidal dust optics accounting for realistic shape distributions produce an excellent agreement with the measured linear depolarization ratio. Although the new ellipsoidal dust optics show potential to improve models and retrievals, it underestimates the magnitude of the backscattering intensity relative to laboratory and field observations. This finding indicates that a realistic quantification of dust body shape is not sufficient and that an accurate quantification of dust surface texture is also critical to accurately reproduce dust optical properties at backscattering angles.

6.2 Future work

The focus of future study is to investigate the effect of dust surface texture on the dust single-scattering properties. The scientific questions are:

- (1) How to quantify the surface texture of atmospheric dust aerosols?
- (2) Does an increase in the surface texture generate a larger backscattered light? and
- (3) Does accounting for both realistic dust body shape and surface roughness enable an improved agreement with field observations of back-scattering properties?

To answer these questions, I will carry a literature review on the measurements of

dust surface texture, and run the discrete dipole approximation code to obtain the single-scattering properties of dust with different levels of rough surfaces.

BIBLIOGRAPHY

- Adebiyi, A. A., and J. F. Kok (2020), Climate models miss most of the coarse dust in the atmosphere, *Science Advances*, *6*(15), eaaz9507, doi:10.1126/sciadv.aaz9507.
- Adebiyi, A. A., J. F. Kok, Y. Wang, A. Ito, D. A. Ridley, P. Nabat, and C. Zhao (2020), Dust Constraints from joint Observational-Modelling-experiMental analysis (Dust-COMM): comparison with measurements and model simulations, *Atmospheric Chemistry and Physics*, *20*(2), 829–863, doi:10.5194/acp-2019-484.
- Alexander, J. M., V. H. Grassian, M. A. Young, and P. D. Kleiber (2015), Optical properties of selected components of mineral dust aerosol processed with organic acids and humic material, *Journal of Geophysical Research*, *120*(6), 2437–2452, doi:10.1002/2014JD022782.
- Alfaro, S. C., and L. Gomes (2001), Modeling mineral aerosol production by wind erosion: Emission intensities and aerosol size distributions in source areas, *Journal of Geophysical Research: Atmospheres*, *106*(D16), 18,075–18,084, doi:10.1029/2000JD900339.
- Almeida-Prieto, S., J. Blanco-Méndez, and F. J. Otero-Espinar (2007), Microscopic image analysis techniques for the morphological characterization of pharmaceutical particles: Influence of the software, and the factor algorithms used in the shape factor estimation, *European Journal of Pharmaceutics and Biopharmaceutics*, *67*(3), 766–776, doi:10.1016/j.ejpb.2007.04.001.
- Amiridis, V., E. Marinou, A. Tsekeri, U. Wandinger, A. Schwarz, E. Giannakaki, R. Mamouri, P. Kokkalis, I. Biniotoglou, S. Solomos, T. Herekakis, S. Kazadzis, E. Gerasopoulos, E. Proestakis, M. Kottas, D. Balis, A. Papayannis, C. Kontoes, K. Kourtidis, N. Papagiannopoulos, L. Mona, G. Pappalardo, O. Le Rille, and A. Ansmann (2015), L-LIVAS: a 3-D multi-wavelength aerosol/cloud database based on CALIPSO and EARLINET, *Atmospheric Chemistry and Physics*, *15*(13), 7127–7153, doi:10.5194/acp-15-7127-2015.

- Andreas, E. L., K. J. Claffey, R. E. Jordan, C. W. Fairall, P. S. Guest, P. O. G. Persson, and A. A. Grachev (2006), Evaluations of the von Kármán constant in the atmospheric surface layer, *Journal of Fluid Mechanics*, *559*, 117–149, doi:10.1017/S0022112006000164.
- Ansmann, A., P. Seifert, M. Tesche, and U. Wandinger (2012), Profiling of fine and coarse particle mass: case studies of Saharan dust and Eyjafjallajökull/Grimsvötn volcanic plumes, *Atmospheric Chemistry and Physics*, *12*(20), 9399–9415, doi:10.5194/acp-12-9399-2012.
- Ansmann, A., F. Rittmeister, R. Engelmann, S. Basart, O. Jorba, C. Spyrou, S. Remy, A. Skupin, H. Baars, P. Seifert, F. Senf, and T. Kanitz (2017), Profiling of Saharan dust from the Caribbean to western Africa - Part 2: Shipborne lidar measurements versus forecasts, *Atmospheric Chemistry and Physics*, *17*(24), 14,987–15,006, doi:10.5194/acp-17-14987-2017.
- Ashkenazy, Y., H. Yizhaq, and H. Tsoar (2012), Sand dune mobility under climate change in the Kalahari and Australian deserts, *Climatic Change*, *112*(3-4), 901–923, doi:10.1007/s10584-011-0264-9.
- Atkinson, J. D., B. J. Murray, M. T. Woodhouse, T. F. Whale, K. J. Baustian, K. S. Carslaw, S. Dobbie, D. O’Sullivan, and T. L. Malkin (2013), The importance of feldspar for ice nucleation by mineral dust in mixed-phase clouds, *Nature*, *498*(7454), 355–358, doi:10.1038/nature12278.
- Baddock, M. C., T. E. Gill, J. E. Bullard, M. D. Acosta, and N. I. Rivera Rivera (2011), Geomorphology of the Chihuahuan Desert based on potential dust emissions, *Journal of Maps*, *7*(1), 249–259, doi:10.4113/jom.2011.1178.
- Bagheri, G., and C. Bonadonna (2016), On the drag of freely falling non-spherical particles, *Powder Technology*, *301*, 526–544, doi:10.1016/j.powtec.2016.06.015.

- Barchyn, T. E., C. H. Hugenholtz, B. Li, C. M. Neuman, and R. Steven Sanderson (2014), From particle counts to flux: Wind tunnel testing and calibration of the 'Wenglor' aeolian sediment transport sensor, *Aeolian Research*, 15, 311–318, doi:10.1016/j.aeolia.2014.06.009.
- Bohren, C. F., and D. R. Huffman (1983), *Absorption and scattering of light by small particles*, 1 ed., 1–544 pp., Wiley-VCH.
- Bowler, J. M. (1973), Clay dunes: Their occurrence, formation and environmental significance, *Earth Science Reviews*, 9(4), 315–338, doi:10.1016/0012-8252(73)90001-9.
- Bullard, J. E., G. H. McTainsh, and C. Pudmenzky (2004), Aeolian abrasion and modes of fine particle production from natural red dune sands: an experimental study, *Sedimentology*, 51(5), 1103–1125, doi:10.1111/j.1365-3091.2004.00662.x.
- Bullard, J. E., G. H. McTainsh, and C. Pudmenzky (2007), Factors affecting the nature and rate of dust production from natural dune sands, *Sedimentology*, 54(1), 169–182, doi:10.1111/j.1365-3091.2006.00827.x.
- Bullard, J. E., S. P. Harrison, M. C. Baddock, N. Drake, T. E. Gill, G. McTainsh, and Y. Sun (2011), Preferential dust sources: A geomorphological classification designed for use in global dust-cycle models, *Journal of Geophysical Research: Earth Surface*, 116(F4), F04,034, doi:10.1029/2011JF002061.
- Burnett, R. T., C. Arden Pope, M. Ezzati, C. Olives, S. S. Lim, S. Mehta, H. H. Shin, G. Singh, B. Hubbell, M. Brauer, H. Ross Anderson, K. R. Smith, J. R. Balmes, N. G. Bruce, H. Kan, F. Laden, A. Prüss-Ustün, M. C. Turner, S. M. Gapstur, W. R. Diver, and A. Cohen (2014), An integrated risk function for estimating the global burden of disease attributable to ambient fine particulate matter exposure, *Environmental Health Perspectives*, 122(4), 397–403, doi:10.1289/ehp.1307049.

- Burton, S. P., R. A. Ferrare, C. A. Hostetler, J. W. Hair, R. R. Rogers, M. D. Obland, C. F. Butler, A. L. Cook, D. B. Harper, and K. D. Froyd (2012), Aerosol classification using airborne High Spectral Resolution Lidar measurements-methodology and examples, *Atmospheric Measurement Techniques*, 5(1), 73–98, doi:10.5194/amt-5-73-2012.
- Chamecki, M., L. S. Freire, N. L. Dias, B. Chen, C. Q. Dias-Junior, L. A. T. Machado, M. Sörgel, A. Tsokankunku, and A. C. De Araújo (2020), Effects of vegetation and topography on the boundary layer structure above the amazon forest, *Journal of the Atmospheric Sciences*, 77(8), 2941–2957, doi:10.1175/JAS-D-20-0063.1.
- Chou, C., P. Formenti, M. Maille, P. Ausset, G. Helas, M. Harrison, and S. Osborne (2008), Size distribution, shape, and composition of mineral dust aerosols collected during the African Monsoon Multidisciplinary Analysis Special Observation Period 0: Dust and Biomass-Burning Experiment field campaign in Niger, January 2006, *Journal of Geophysical Research Atmospheres*, 113(23), D00C10, doi:10.1029/2008JD009897.
- Colarco, P. R., E. P. Nowottnick, C. A. Randles, B. Yi, P. Yang, K.-M. Kim, J. A. Smith, and C. G. Bardeen (2014), Impact of radiatively interactive dust aerosols in the NASA GEOS-5 climate model: Sensitivity to dust particle shape and refractive index, *Journal of Geophysical Research: Atmospheres*, 119(2), 753–786, doi:10.1002/2013JD020046.
- Combellick, R. A., and R. H. Osborne (1977), Sources and petrology of beach sand from southern Monterey Bay, California, *Journal of Sedimentary Petrology*, 47(2), 891–907.
- Compton, J. S. (1991), Origin and diagenesis of clay minerals in the Monterey Formation, Santa Maria Basin Area, California, *Clays and Clay Minerals*, 39(5), 449–466, doi:10.1346/CCMN.1991.0390501.
- Cooper, W. S. (1967), *Coastal dunes of California*, 1–147 pp., Geological Society of America, doi:https://dx.doi.org/10.1130/MEM104-p1.

- Coz, E., F. J. Gómez-Moreno, M. Pujadas, G. S. Casuccio, T. L. Lersch, and B. Artíñano (2009), Individual particle characteristics of North African dust under different long-range transport scenarios, *Atmospheric Environment*, *43*(11), 1850–1863, doi:10.1016/j.atmosenv.2008.12.045.
- Creamean, J. M., K. J. Suski, D. Rosenfeld, A. Cazorla, P. J. DeMott, R. C. Sullivan, A. B. White, F. Ralph, P. Minnis, J. M. Comstock, J. M. Tomlinson, and K. A. Prather (2013), Dust and Biological Aerosols from the Sahara and Asia Influence Precipitation in the Western U.S., *Science*, *339*(6127), 1572–1578, doi:10.1126/science.1227279.
- Crouvi, O., K. Schepanski, R. Amit, A. R. Gillespie, and Y. Enzel (2012), Multiple dust sources in the Sahara Desert: The importance of sand dunes, *Geophysical Research Letters*, *39*(13), L13,401, doi:10.1029/2012GL052145.
- Delmonte, B., J. Petit, and V. Maggi (2002), Glacial to Holocene implications of the new 27000-year dust record from the EPICA Dome C (East Antarctica) ice core, *Climate Dynamics*, *18*(8), 647–660, doi:10.1007/s00382-001-0193-9.
- DeMott, P. J., K. Sassen, M. R. Poellot, D. Baumgardner, D. C. Rogers, S. D. Brooks, A. J. Prenni, and S. M. Kreidenweis (2003), African dust aerosols as atmospheric ice nuclei, *Geophysical Research Letters*, *30*(14), 26–29, doi:10.1029/2003GL017410.
- DeMott, P. J., A. J. Prenni, G. R. McMeeking, R. C. Sullivan, M. D. Petters, Y. Tobo, M. Niemand, O. Mohler, J. R. Snider, Z. Wang, and S. M. Kreidenweis (2015), Integrating laboratory and field data to quantify the immersion freezing ice nucleation activity of mineral dust particles, *Atmospheric Chemistry and Physics*, *15*(1), 393–409, doi:10.5194/acp-15-393-2015.
- Denjean, C., S. Caquineau, K. Desboeufs, B. Laurent, M. Maille, M. Quiñones Rosado, P. Vallejo, O. L. Mayol-Bracero, and P. Formenti (2015), Long-range transport across

the Atlantic in summertime does not enhance the hygroscopicity of African mineral dust, *Geophysical Research Letters*, *42*(18), 7835–7843, doi:10.1002/2015GL065693.

Dettinger, M. D., D. R. Cayan, M. K. Meyer, and A. Jeton (2004), Simulated hydrologic responses to climate variations and change in the Merced, Carson, and American River basins, Sierra Nevada, California, 1900-2099, *Climatic Change*, *62*(1-3), 283–317, doi:10.1023/B:CLIM.0000013683.13346.4f.

Di Biagio, C., P. Formenti, Y. Balkanski, L. Caponi, M. Cazaunau, E. Pangui, E. Journet, S. Nowak, S. Caquineau, M. O. Andreae, K. Kandler, T. Saeed, S. Piketh, D. Seibert, E. Williams, and J.-F. Doussin (2017), Global scale variability of the mineral dust long-wave refractive index: a new dataset of in situ measurements for climate modeling and remote sensing, *Atmospheric Chemistry and Physics*, *17*(3), 1901–1929, doi:10.5194/acp-17-1901-2017.

Di Biagio, C., P. Formenti, Y. Balkanski, L. Caponi, M. Cazaunau, E. Pangui, E. Journet, S. Nowak, M. O. Andreae, K. Kandler, T. Saeed, S. Piketh, D. Seibert, E. Williams, and J.-F. Doussin (2019), Complex refractive indices and single scattering albedo of global dust aerosols in the shortwave spectrum and relationship to iron content and size, *Atmospheric Chemistry and Physics*, *19*(24), 15,503–15,531, doi:10.5194/acp-2019-145.

Di Biagio, C., Y. Balkanski, S. Albani, O. Boucher, and P. Formenti (2020), Direct Radiative Effect by Mineral Dust Aerosols Constrained by New Microphysical and Spectral Optical Data, *Geophysical Research Letters*, *47*(2), 1–12, doi:10.1029/2019GL086186.

Domingo, R. A., R. J. Southard, and K. Lee (2010), Laboratory System for Dust Generation from Soils, *Journal of Environment Quality*, *39*(4), 1254–1261, doi:10.2134/jeq2008.0380.

Dubovik, O., A. Sinyuk, T. Lapyonok, B. N. Holben, M. Mishchenko, P. Yang, T. F. Eck, H. Volten, O. Muñoz, B. Veihelmann, W. J. van der Zande, J. F. Leon, M. Sorokin, and

- I. Slutsker (2006), Application of spheroid models to account for aerosol particle non-sphericity in remote sensing of desert dust, *Journal of Geophysical Research Atmospheres*, *111*(11), D11,208, doi:10.1029/2005JD006619.
- Dueker, M. E., K. C. Weathers, G. D. O'Mullan, A. R. Juhl, and M. Uriarte (2011), Environmental Controls on Coastal Coarse Aerosols : Implications for Microbial Content and Deposition in the Near-Shore Environment, *Environmental science technology*, *45*(8), 3386–3392, doi:10.1021/es1035128.
- Dutta, P. K., Z. Zhou, and P. R. dos Santos (1993), A theoretical study of mineralogical maturation of eolian sand, *Geological Society of America Special Paper*, *284*, 203–209.
- Engelstaedter, S., I. Tegen, and R. Washington (2006), North African dust emissions and transport, *Earth-Science Reviews*, *79*(1-2), 73–100, doi:10.1016/j.earscirev.2006.06.004.
- Evan, A. T., S. Fiedler, C. Zhao, L. Menut, K. Schepanski, C. Flamant, and O. Doherty (2015), Derivation of an observation-based map of North African dust emission, *Aeolian Research*, *16*, 153–162, doi:10.1016/j.aeolia.2015.01.001.
- Feng, J.-L., L.-P. Zhu, J.-T. Ju, L.-P. Zhou, X.-L. Zhen, W. Zhang, and G. Shao-Peng (2008), Heavy dust fall in Beijing on April 16-17, 2006: geochemical properties and indications of the dust provenance, *Geochemical Journal*, *42*(2), 221–236, doi:https://doi.org/10.2343/geochemj.42.221.
- Formenti, P., L. Schütz, Y. Balkanski, K. Desboeufs, M. Ebert, K. Kandler, A. Petzold, D. Scheuven, S. Weinbruch, and D. Zhang (2011), Recent progress in understanding physical and chemical properties of African and Asian mineral dust, *Atmospheric Chemistry and Physics*, *11*(16), 8231–8256, doi:10.5194/acp-11-8231-2011.
- Fratini, G., P. Ciccioli, A. Febo, A. Forgione, and R. Valentini (2007), Size-segregated fluxes of mineral dust from a desert area of northern China by eddy covariance, *Atmospheric Chemistry and Physics*, *7*(11), 2133–2168, doi:10.5194/acpd-7-2133-2007.

- Fryrear, D. (1986), A field dust sampler, *Journal of Soil and Water Conservation*, 41(2), 117–120.
- Gardner, R., and K. Pye (1981), Nature, origin and palaeoenvironmental significance of red coastal and desert dune sands, *Progress in Physical Geography*, 5(4), 514–534, doi:10.1177/030913338100500402.
- Gasteiger, J., M. Wiegner, S. Groß, V. Freudenthaler, C. Toledano, M. Tesche, and K. Kandler (2011), Modelling lidar-relevant optical properties of complex mineral dust aerosols, *Tellus, Series B: Chemical and Physical Meteorology*, 63(4), 725–741, doi:10.1111/j.1600-0889.2011.00559.x.
- Gasteiger, J., S. Groß, D. Sauer, M. Haarig, A. Ansmann, and B. Weinzierl (2017), Particle settling and vertical mixing in the Saharan Air Layer as seen from an integrated model, lidar, and in situ perspective, *Atmospheric Chemistry and Physics*, 17(1), 297–311, doi:10.5194/acp-17-297-2017.
- Giannadaki, D., A. Pozzer, and J. Lelieveld (2014), Modeled global effects of airborne desert dust on air quality and premature mortality, *Atmospheric Chemistry and Physics*, 14(2), 957–968, doi:10.5194/acp-14-957-2014.
- Gillette, D., I. Blifford Jr., and D. Fryrear (1974), The influence of wind velocity on the size distributions of aerosols generated by the wind erosion of soils, *Journal of Geophysical Research*, 79(27), 4068–4075, doi:10.1029/JC079i027p04068.
- Gillette, D. A. (1974), On the production of soil wind erosion aerosols having the potential for long range transport, *Journal de Recherches Atmospheriques*, 8, 734–744.
- Gillette, D. A., I. H. Blifford, and C. R. Fenster (1972), Measurements of aerosol size distributions and vertical fluxes of aerosols on land subject to wind erosion, *Journal of Applied Meteorology and Climatology*, 11(6), 977–987, doi:10.1175/1520-0450(1972)011<0977:MOASDA>2.0.CO;2.

- Gillies, J., and L. Berkofsky (2004), Eolian suspension above the saltation layer, the concentration profile, *Journal of Sedimentary Research*, *74*(2), 176–183, doi:10.1306/091303740176.
- Gillies, J. A., V. Etyemezian, G. Nikolich, R. Glick, P. Rowland, T. Pesce, and M. Skinner (2017), Effectiveness of an array of porous fences to reduce sand flux: Oceano Dunes, Oceano CA, *Journal of Wind Engineering and Industrial Aerodynamics*, *168*(April 2016), 247–259, doi:10.1016/j.jweia.2017.06.015.
- Ginoux, P. (2003), Effects of nonsphericity on mineral dust modeling, *Journal of Geophysical Research*, *108*(D2), 4052, doi:10.1029/2002JD002516.
- Ginoux, P., M. Chin, I. Tegen, J. M. Prospero, B. Holben, O. Dubovik, and S.-J. Lin (2001), Sources and distributions of dust aerosols simulated with the GOCART model, *Journal of Geophysical Research: Atmospheres*, *106*(D17), 20,255–20,273, doi:10.1029/2000JD000053.
- Ginoux, P., J. M. Prospero, T. E. Gill, N. C. Hsu, and M. Zhao (2012), Global-scale attribution of anthropogenic and natural dust sources and their emission rates based on MODIS Deep Blue aerosol products, *Reviews of Geophysics*, *50*(3), 1–36, doi:10.1029/2012RG000388.
- Gómez Martín, J. C., D. Guirado, E. Frattin, M. Bermudez-Edo, P. Cariñanos Gonzalez, F. J. Olmo Reyes, T. Nousiainen, P. J. Gutiérrez, F. Moreno, and O. Muñoz (2021), On the application of scattering matrix measurements to detection and identification of major types of airborne aerosol particles: Volcanic ash, desert dust and pollen, *Journal of Quantitative Spectroscopy and Radiative Transfer*, *271*, 107,761, doi:10.1016/j.jqsrt.2021.107761.
- Goossens, D., and B. Buck (2011), Effects of wind erosion, off-road vehicular activity, atmospheric conditions and the proximity of a metropolitan area on PM10 characteristics in a

- recreational site, *Atmospheric Environment*, 45(1), 94–107, doi:10.1016/j.atmosenv.2010.09.046.
- Goossens, D., Z. Offer, and G. London (2000), Wind tunnel and field calibration of five aeolian sand traps, *Geomorphology*, 35(3-4), 233–252, doi:10.1016/S0169-555X(00)00041-6.
- Goossens, D., B. Buck, and B. McLaurin (2012), Contributions to atmospheric dust production of natural and anthropogenic emissions in a recreational area designated for off-road vehicular activity (Nellis Dunes, Nevada, USA), *Journal of Arid Environments*, 78, 80–99, doi:10.1016/j.jaridenv.2011.10.015.
- Gualtieri, A. (1996), Modal analysis of pyroclastic rocks by combined Rietveld and RIR methods, *Powder Diffraction*, 11(2), 97–106, doi:10.1017/S0885715600009052.
- Gualtieri, A. F. (2000), Accuracy of XRPD QPA using the combined Rietveld-RIR method, *Journal of Applied Crystallography*, 33, 267–278, doi:10.1107/S002188989901643X.
- Harrison, R. G., K. A. Nicoll, G. J. Marlton, C. L. Ryder, and A. J. Bennett (2018), Saharan dust plume charging observed over the UK, *Environmental Research Letters*, 13(5), 1–9, doi:10.1088/1748-9326/aabcd9.
- Hess, M., P. Koepke, and I. Schult (1998), Optical properties of aerosols and clouds: the software package OPAC, *Bulletin of the American Meteorological Society*, 79, 831–844, doi:10.1175/1520-0477(1998)079<0831:OPOAAC>2.0.CO;2.
- Hillel, D. (1998), *Environmental soil physics*, 1 ed., 1–771 pp., Academic Press, San Diego.
- Hinds, W. C. (1999), *Aerosol technology: properties, behavior, and measurement of airborne particles*, 2 ed., 1–504 pp., Wiley-Interscience.
- Hsu, N., J. Lee, A. Sayer, W. Kim, C. Bettenhausen, and S.-C. Tsay (2019), VIIRS Deep Blue Aerosol Products over Land: Extending the EOS Long-Term Aerosol Data Records, *Journal of Geophysical Research: Atmospheres*, 124(7), 4026–4053, doi:10.1029/2018jd029688.

- Huang, Y., J. F. Kok, R. L. Martin, N. Swet, I. Katra, T. E. Gill, R. L. Reynolds, and L. S. Freire (2019), Fine dust emissions from active sands at coastal Oceano Dunes, California, *Atmospheric Chemistry and Physics*, *19*(5), 2947–2964, doi:10.5194/acp-19-2947-2019.
- Huang, Y., J. F. Kok, K. Kandler, H. Lindqvist, T. Nousiainen, T. Sakai, A. Adebisi, and O. Jokinen (2020), Climate models and remote sensing retrievals neglect substantial desert dust asphericity, *Geophysical Research Letters*, *47*(6), 1–11, doi:10.1029/2019GL086592.
- Huang, Y., A. A. Adebisi, P. Formenti, and J. F. Kok (2021), Linking the different diameter types of aspherical desert dust indicates that models underestimate coarse dust emission, *Geophysical Research Letters*, *48*(6), 1–12, doi:10.1029/2020GL092054.
- Huneeus, N., M. Schulz, Y. Balkanski, J. Griesfeller, J. M. Prospero, S. Kinne, S. Bauer, O. Boucher, M. Chin, F. Dentener, T. Diehl, R. C. Easter, D. Fillmore, S. Ghan, P. Ginoux, A. Grini, L. Horowitz, D. Koch, M. C. Krol, W. Landing, X. Liu, N. Mahowald, R. Miller, J.-J. Morcrette, G. Myhre, J. E. Penner, J. Perlwitz, P. Stier, T. Takemura, and C. S. Zender (2011), Global dust model intercomparison in AeroCom phase I, *Atmospheric Chemistry and Physics*, *11*(15), 7781–7816, doi:10.5194/acp-11-7781-2011.
- IPCC AR5 (2013), Chapt1-Introduction in Climate Change 2013, *Intergovernmental Panel on Climate Change 2013: The Physical Science Basis. Contribution of Working Group I to the Fifth Assessment Report of the Intergovernmental Panel on Climate Change*, pp. 119–158, doi:10.1017/CBO9781107415324.007.
- ISO (2009), Determination of particle size distribution: single particle light interaction methods, part 1: Light scattering aerosol spectrometer, *ISO 21501-1*.
- Ito, A., and J. F. Kok (2017), Do dust emissions from sparsely vegetated regions dominate atmospheric iron supply to the Southern Ocean?, *Journal of Geophysical Research: Atmospheres*, *122*(7), 3987–4002, doi:10.1002/2016JD025939.

- Ito, A., S. Myriokefalitakis, M. Kanakidou, N. M. Mahowald, R. A. Scanza, D. S. Hamilton, A. R. Baker, T. Jickells, M. Sarin, S. Bikkina, Y. Gao, R. U. Shelley, C. S. Buck, W. M. Landing, A. R. Bowie, M. M. Perron, C. Guieu, N. Meskhidze, M. S. Johnson, Y. Feng, J. F. Kok, A. Nenes, and R. A. Duce (2019), Pyrogenic iron: The missing link to high iron solubility in aerosols, *Science Advances*, *5*(5), eaau7671, doi:10.1126/sciadv.aau7671.
- Ito, A., A. A. Adebiyi, Y. Huang, and J. F. Kok (2021), Less atmospheric radiative heating due to aspherical dust with coarser size, *Atmospheric Chemistry and Physics Discussions*, (February), doi:10.5194/acp-2021-134.
- James, W. C., G. H. Mack, and L. J. Suttner (1981), Relative alteration of microcline and sodic plagioclase in semi-arid and humid climates, *Journal of Sedimentary Petrology*, *51*(1), 151–163.
- Jari, M. (1995), Effects of grinding and chemical factors on the generation and composition of the till fine fraction: an experimental study, *Journal of Geochemical Exploration*, *54*(1), 49–62, doi:10.1016/0375-6742(95)00008-D.
- Jeong, G. Y., M. Y. Park, K. Kandler, T. Nousiainen, and O. Kemppinen (2016), Mineralogical properties and internal structures of individual fine particles of Saharan dust, *Atmospheric Chemistry and Physics*, *16*(19), 12,397–12,410, doi:10.5194/acp-16-12397-2016.
- Jerolmack, D. J., and T. A. Brzinski (2010), Equivalence of abrupt grain-size transitions in alluvial rivers and eolian sand seas: A hypothesis, *Geology*, *38*(8), 719–722, doi:10.1130/G30922.1.
- Jerolmack, D. J., M. D. Reitz, and R. L. Martin (2011), Sorting out abrasion in a gypsum dune field, *Journal of Geophysical Research Earth Surface*, *116*(2), F02,003, doi:10.1029/2010JF001821.
- Jickells, T. D., Z. S. An, K. K. Andersen, A. R. Baker, G. Bergametti, N. Brooks, J. J. Cao, P. W. Boyd, R. A. Duce, K. A. Hunter, H. Kawahata, N. Kubilay, J. LaRoche, P. S. Liss,

- N. M. Mahowald, J. M. Prospero, A. J. Ridgwell, I. Tegen, and R. Torres (2005), Global Iron Connections Between Desert Dust, Ocean Biogeochemistry, and Climate, *Science*, *308*(5718), 67–71, doi:10.1126/science.1105959.
- Kahn, R. A., and B. J. Gaitley (2015), An analysis of global aerosol type as retrieved by MISR, *Journal of Geophysical Research : Atmospheres*, *120*(9), 4248–4281, doi:10.1002/2015JD023322.Received.
- Kahnert, M., F. Kanngießer, E. Järvinen, and M. Schnaiter (2020), Aerosol-optics model for the backscatter depolarisation ratio of mineral dust particles, *Journal of Quantitative Spectroscopy and Radiative Transfer*, *254*, 107,177, doi:10.1016/j.jqsrt.2020.107177.
- Kalashnikova, O. V., and I. N. Sokolik (2004), Modeling the radiative properties of non-spherical soil-derived mineral aerosols, *Journal of Quantitative Spectroscopy and Radiative Transfer*, *87*(2), 137–166, doi:10.1016/j.jqsrt.2003.12.026.
- Kalashnikova, O. V., R. Kahn, I. N. Sokolik, and W.-H. Li (2005), Ability of multiangle remote sensing observations to identify and distinguish mineral dust types: Optical models and retrievals of optically thick plumes, *Journal of Geophysical Research: Atmospheres*, *110*(18), D18S14, doi:10.1029/2004JD004550.
- Kandler, K., N. Benker, U. Bundke, E. Cuevas, M. Ebert, P. Knippertz, S. Rodríguez, L. Schütz, and S. Weinbruch (2007), Chemical composition and complex refractive index of Saharan Mineral Dust at Izaña, Tenerife (Spain) derived by electron microscopy, *Atmospheric Environment*, *41*(37), 8058–8074, doi:10.1016/j.atmosenv.2007.06.047.
- Kandler, K., L. Schütz, C. Deutscher, M. Ebert, H. Hofmann, S. Jäckel, R. Jaenicke, P. Knippertz, K. Lieke, A. Massling, A. Petzold, A. Schladitz, B. Weinzierl, A. Wiedensohler, S. Zorn, and S. Weinbruch (2009), Size distribution, mass concentration, chemical and mineralogical composition and derived optical parameters of the boundary layer aerosol

- at Tinfou, Morocco, during SAMUM 2006, *Tellus, Series B: Chemical and Physical Meteorology*, 61(1), 32–50, doi:10.1111/j.1600-0889.2008.00385.x.
- Kandler, K., L. Schütz, S. Jäckel, K. Lieke, C. Emmel, D. Müller-Ebert, M. Ebert, D. Scheuven, A. Schladitz, B. Šegvić, A. Wiedensohler, and S. Weinbruch (2011), Ground-based off-line aerosol measurements at Praia, Cape Verde, during the Saharan Mineral Dust Experiment: Microphysical properties and mineralogy, *Tellus, Series B: Chemical and Physical Meteorology*, 63(4), 459–474, doi:10.1111/j.1600-0889.2011.00546.x.
- Kasper-Zubillaga, J. J., H. Zolezzi-Ruiz, A. Carranza-Edwards, P. Girón-García, G. Ortiz-Zamora, and M. Palma (2007), Sedimentological, modal analysis and geochemical studies of desert and coastal dunes, Altar Desert, NW Mexico, *Earth Surface Processes and Landforms*, 32(4), 489–508, doi:doi.org/10.1002/esp.1402.
- Katra, I., and H. Yizhaq (2017), Intensity and degree of segregation in bimodal and multimodal grain size distributions, *Aeolian Research*, 27, 23–34, doi:10.1016/j.aeolia.2017.05.002.
- Kemppinen, O., T. Nousiainen, and H. Lindqvist (2015), The impact of surface roughness on scattering by realistically shaped wavelength-scale dust particles, *Journal of Quantitative Spectroscopy and Radiative Transfer*, 150, 55–67, doi:10.1016/j.jqsrt.2014.05.024.
- Khalfallah, B., C. Bouet, M. T. Labiadh, S. C. Alfaro, G. Bergametti, B. Marticorena, S. Lafon, S. Chevaillier, A. Féron, P. Hease, T. Henry des Tureaux, S. Sekrafi, P. Zapf, and J. L. Rajot (2020), Influence of Atmospheric Stability on the Size Distribution of the Vertical Dust Flux Measured in Eroding Conditions Over a Flat Bare Sandy Field, *Journal of Geophysical Research: Atmospheres*, 125(4), 1–20, doi:10.1029/2019JD031185.
- Kind, R. J. (1992), One-dimensional aeolian suspension above beds of loose particles-A new concentration-profile equation, *Atmospheric Environment*, 26A(5), 927–931, doi:10.1016/0960-1686(92)90250-O.

- Kinne, S., M. Schulz, C. Textor, S. Guibert, Y. Balkanski, S. E. Bauer, T. Berntsen, T. F. Berglen, O. Boucher, M. Chin, W. Collins, F. Dentener, T. Diehl, R. Easter, J. Feichter, D. Fillmore, S. Ghan, P. Ginoux, S. Gong, A. Grini, J. Hendricks, M. Herzog, L. Horowitz, I. Isaksen, T. Iversen, A. Kirkevåg, S. Kloster, D. Koch, J. E. Kristjansson, M. Krol, A. Lauer, J. F. Lamarque, G. Lesins, X. Liu, U. Lohmann, V. Montanaro, G. Myhre, J. E. Penner, G. Pitari, S. Reddy, O. Seland, P. Stier, T. Takemura, and X. Tie (2006), An AeroCom initial assessment - Optical properties in aerosol component modules of global models, *Atmospheric Chemistry and Physics*, *6*(7), 1815–1834, doi:10.5194/acp-6-1815-2006.
- Kiselev, A., F. Bachmann, P. Pedevilla, S. J. Cox, A. Michaelides, D. Gerthsen, and T. Leisner (2017), Active sites in heterogeneous ice nucleation—the example of K-rich feldspars, *Science*, *355*(6323), 367–371, doi:10.1126/science.aai8034.
- Klose, M., and Y. Shao (2012), Stochastic parameterization of dust emission and application to convective atmospheric conditions, *Atmospheric Chemistry and Physics*, *12*(16), 7309–7320, doi:10.5194/acp-12-7309-2012.
- Klose, M., O. Jorba, M. G. Ageitos, J. Escribano, L. Dawson, V. Obiso, E. D. Tomaso, S. Basart, G. M. Pinto, F. Macchia, P. Ginoux, J. Guerschman, C. Prigent, Y. Huang, J. F. Kok, R. L. Miller, and C. P. García-pando (2021), Mineral dust cycle in the Multiscale Online Nonhydrostatic Atmosphere Chemistry model (MONARCH) Version 2.0, *Geoscientific Model Development Discussions*, (February), 1–59, doi:10.5194/gmd-2021-32.
- Klute, E. A. (1986), *Methods of Soil Analysis. Part 1. Physical and Mineralogical Methods*, 2nd ed., 1–1358 pp., American Society of Agronomy, Inc.; Soil Science Society of America, Inc., Madison, Wisconsin USA.
- Kok, J. F. (2011a), A scaling theory for the size distribution of emitted dust aerosols suggests climate models underestimate the size of the global dust cycle, *Proceedings of the National Academy of Sciences of the United States of America*, *108*(3), 1016–1021, doi:10.1073/pnas.1014798108.

- Kok, J. F. (2011b), Does the size distribution of mineral dust aerosols depend on the wind speed at emission?, *Atmospheric Chemistry and Physics*, *11*(19), 10,149–10,156, doi:10.5194/acp-11-10149-2011.
- Kok, J. F., E. J. R. Parteli, T. I. Michaels, and D. B. Karam (2012), The physics of wind-blown sand and dust, *Reports on Progress in Physics*, *75*(10), doi:10.1088/0034-4885/75/10/106901.
- Kok, J. F., N. M. Mahowald, G. Fratini, J. A. Gillies, M. Ishizuka, J. F. Leys, M. Mikami, M. S. Park, S. U. Park, R. S. Van Pelt, and T. M. Zobeck (2014a), An improved dust emission model - Part 1: Model description and comparison against measurements, *Atmospheric Chemistry and Physics*, *14*(23), 13,023–13,041, doi:10.5194/acp-14-13023-2014.
- Kok, J. F., S. Albani, N. M. Mahowald, and D. S. Ward (2014b), An improved dust emission model - Part 2: Evaluation in the Community Earth System Model, with implications for the use of dust source functions, *Atmospheric Chemistry and Physics*, *14*(23), 13,043–13,061, doi:10.5194/acp-14-13043-2014.
- Kok, J. F., D. A. Ridley, Q. Zhou, R. L. Miller, C. Zhao, C. L. Heald, D. S. Ward, S. Albani, and K. Haustein (2017), Smaller desert dust cooling effect estimated from analysis of dust size and abundance, *Nature Geoscience*, *10*, 274–278, doi:10.1038/ngeo2912.
- Kok, J. F., D. S. Ward, N. M. Mahowald, and A. T. Evan (2018), Global and regional importance of the direct dust-climate feedback, *Nature Communications*, *9*(241), 1–11, doi:10.1038/s41467-017-02620-y.
- Kok, J. F., A. A. Adebisi, S. Albani, Y. Balkanski, R. Checa-Garcia, M. Chin, P. Colarco, D. S. Hamilton, Y. Huang, A. Ito, M. Klose, D. M. Leung, L. Li, N. M. Mahowald, R. L. Miller, V. Obiso, C. Pérez García-Pando, A. Rocha-Lima, J. S. Wan, and C. A. Whicker (2021a), Improved representation of the global dust cycle using observational constraints

- on dust properties and abundance, *Atmospheric Chemistry and Physics*, 21(10), 8127–8167, doi:10.5194/acp-21-8127-2021.
- Kok, J. F., A. A. Adebisi, S. Albani, Y. Balkanski, R. Checa-Garcia, M. Chin, P. Colarco, D. Hamilton, Y. Huang, A. Ito, M. Klose, L. Li, N. M. Mahowald, R. L. Miller, V. Obiso, C. Pérez García-Pando, A. Rocha-Lima, and J. S. Wan (2021b), Contribution of the world’s main dust source regions to the global cycle of desert dust, *Atmospheric Chemistry and Physics*, 21(10), 8169–8193, doi:10.5194/acp-21-8169-2021.
- Kuenen, P. H. (1960), Experimental abrasion 4: Eolian Action, *The Journal of Geology*, 68(4), 427–449, doi:10.1086/626675.
- Kuenen, P. H. (1969), Origin of quartz silt, *Journal of Sedimentary Research*, 39(4), 1631–1633, doi:https://doi.org/10.1306/74D71ED3-2B21-11D7-8648000102C1865D.
- Laskina, O., M. A. Young, P. D. Kleiber, and V. H. Grassian (2013), Infrared extinction spectroscopy and micro-Raman spectroscopy of select components of mineral dust mixed with organic compounds, *Journal of Geophysical Research Atmospheres*, 118(12), 6593–6606, doi:10.1002/jgrd.50494.
- Li, J., and K. Osada (2007), Water-Insoluble Particles in Spring Snow at Mt. Tateyama, Japan: Characteristics of the Shape Factors and Size Distribution in Relation with Their Origin and Transportation, *Journal of the Meteorological Society of Japan. Ser. II*, 85(2), 137–149, doi:10.2151/jmsj.85.137.
- Liang, T., M. Chamecki, and X. Yu (2016), Sea salt aerosol deposition in the coastal zone: A large eddy simulation study, *Atmospheric Research*, 180, 119–127, doi:10.1016/j.atmosres.2016.05.019.
- Lindqvist, H., O. Jokinen, K. Kandler, D. Scheuven, and T. Nousiainen (2014), Single scattering by realistic, inhomogeneous mineral dust particles with stereogrammetric shapes, *Atmospheric Chemistry and Physics*, 14(1), 143–157, doi:10.5194/acp-14-143-2014.

- Liou, K.-N. (2002), *An introduction to atmospheric radiation*, 2 ed., 1–583 pp., Academic Press, Inc.
- Liu, H., G. Peters, and T. Foken (2001), New equations for sonic temperature variance and buoyancy heat flux with an omnidirectional sonic anemometer, *Boundary-Layer Meteorology*, *100*(3), 459–468, doi:10.1023/A:1019207031397.
- Mahowald, N., S. Albani, J. F. Kok, S. Engelstaeder, R. Scanza, D. S. Ward, and M. G. Flanner (2014), The size distribution of desert dust aerosols and its impact on the Earth system, *Aeolian Research*, *15*, 53–71, doi:10.1016/j.aeolia.2013.09.002.
- Mahowald, N. M., J. A. Ballantine, J. Feddema, and N. Ramankutty (2007), Global trends in visibility: implications for dust sources, *Atmospheric Chemistry and Physics*, *7*(12), 3309–3339, doi:10.5194/acp-7-3309-2007.
- Marcotte, A. R., A. D. Anbar, B. J. Majestic, and P. Herckes (2020), Mineral Dust and Iron Solubility: Effects of Composition, Particle Size, and Surface Area, *Atmosphere*, *11*(5), 1–12, doi:10.3390/atmos11050533.
- Martcorena, B., and G. Bergametti (1995), Modeling the atmospheric dust cycle: 1. Design of a soil-derived dust emission scheme, *Journal of Geophysical Research: Atmospheres*, *100*(D8), 16,415–16,430, doi:10.1029/95JD00690.
- Martin, R. L., and J. F. Kok (2017), Wind-invariant saltation heights imply linear scaling of aeolian saltation flux with shear stress, *Science Advances*, *3*(6), e1602569, doi:10.1126/sciadv.1602569.
- Martin, R. L., J. F. Kok, C. H. Hugenholtz, T. E. Barchyn, M. Chamecki, and J. T. Ellis (2018), High-frequency measurements of aeolian saltation flux: Field-based methodology and applications, *Aeolian Research*, *30*, 97–114, doi:10.1016/j.aeolia.2017.12.003.
- Mätzler, C. (2002), MATLAB Functions for Mie Scattering and Absorption, version 2, *IAP Res. Rep.*, pp. 1–24, doi:10.1039/b811392k.

- McKee, E. D. (1979), Ancient sandstones considered to be eolian, *U.S. Geological Survey Professional Paper, 1052*, 189–238.
- Meng, Z., P. Yang, G. W. Kattawar, L. Bi, K. N. Liou, and I. Laszlo (2010), Single-scattering properties of tri-axial ellipsoidal mineral dust aerosols: A database for application to radiative transfer calculations, *Journal of Aerosol Science*, *41*(5), 501–512, doi:10.1016/j.jaerosci.2010.02.008.
- Merikallio, S., H. Lindqvist, T. Nousiainen, and M. Kahnert (2011), Modelling light scattering by mineral dust using spheroids: Assessment of applicability, *Atmospheric Chemistry and Physics*, *11*(11), 5347–5363, doi:10.5194/acp-11-5347-2011.
- Miller, R. L., I. Tegen, and J. Perlwitz (2004), Surface radiative forcing by soil dust aerosols and the hydrologic cycle, *Journal of Geophysical Research: Atmospheres*, *109*(D4), D04,203, doi:10.1029/2003JD004085.
- Miller, R. L., R. V. Cakmur, J. Perlwitz, I. V. Geogdzhayev, P. Ginoux, D. Koch, K. E. Kohfeld, C. Prigent, R. Ruedy, G. A. Schmidt, and I. Tegen (2006), Mineral dust aerosols in the NASA Goddard Institute for Space Sciences ModelE atmospheric general circulation model, *Journal of Geophysical Research Atmospheres*, *111*(6), D06,208, doi:10.1029/2005JD005796.
- Mishchenko, M. I., and M. A. Yurkin (2017), On the concept of random orientation in far-field electromagnetic scattering by nonspherical particles, *Optics Letters*, *42*(3), 494–497, doi:10.1364/ol.42.000494.
- Moreno, T., W. Gibbons, T. Jones, and R. Richards (2003), The geology of ambient aerosols: characterising urban and rural/coastal silicate PM_{10-2.5} and PM_{2.5} using high-volume cascade collection and scanning electron microscopy, *Atmospheric Environment*, *37*(30), 4265–4276, doi:10.1016/S1352-2310(03)00534-X.

- Muhs, D. R. (2004), Mineralogical maturity in dunefields of North America, Africa and Australia, *Geomorphology*, 59(1-4), 247–269, doi:10.1016/j.geomorph.2003.07.020.
- Muhs, D. R., T. W. Stafford, J. B. Swinehart, S. D. Cowherd, S. A. Mahan, C. A. Bush, R. F. Madole, and P. B. Maat (1997), Late Holocene eolian activity in the mineralogically mature Nebraska Sand Hills, *Quaternary Research*, 48(2), 162–176, doi:10.1006/qres.1997.1913.
- Müller, D., A. Ansmann, V. Freudenthaler, K. Kandler, C. Toledano, A. Hiebsch, J. Gasteiger, M. Esselborn, M. Tesche, B. Heese, D. Althausen, B. Weinzierl, A. Petzold, and W. Von Hoyningen-Huene (2010), Mineral dust observed with AERONET Sun photometer, Raman lidar, and in situ instruments during SAMUM 2006: Shape-dependent particle properties, *Journal of Geophysical Research Atmospheres*, 115(D11), 1–11, doi: <https://doi.org/10.1029/2009JD012523>.
- Müller, D., K.-H. Lee, J. Gasteiger, M. Tesche, B. Weinzierl, K. Kandler, T. Müller, C. Toledano, S. Otto, D. Althausen, and A. Ansmann (2012), Comparison of optical and microphysical properties of pure Saharan mineral dust observed with AERONET Sun photometer, Raman lidar, and in situ instruments during SAMUM 2006, *Journal of Geophysical Research Atmospheres*, 117(D7), D07,211, doi:10.1029/2011JD016825.
- Muñoz, O., F. Moreno, D. Guirado, D. D. Dabrowska, H. Volten, and J. W. Hovenier (2012), The Amsterdam-Granada Light Scattering Database, *Journal of Quantitative Spectroscopy and Radiative Transfer*, 113(7), 565–574, doi:10.1016/j.jqsrt.2012.01.014.
- Murray, B. J., D. O’Sullivan, J. D. Atkinson, and M. E. Webb (2012), Ice nucleation by particles immersed in supercooled cloud droplets, *Chemical Society Reviews*, 41(19), 6519, doi:10.1039/c2cs35200a.
- Nabat, P., F. Solmon, M. Mallet, J. F. Kok, and S. Somot (2012), Dust emission size distribution impact on aerosol budget and radiative forcing over the Mediterranean region:

- A regional climate model approach, *Atmospheric Chemistry and Physics*, 12(21), 10,545–10,567, doi:10.5194/acp-12-10545-2012.
- Nesbitt, H. W., C. M. Fedo, and G. M. Young (1997), Quartz and Feldspar Stability, Steady and Non-Steady-State Weathering, and Petrogenesis of Siliciclastic Sands and Muds, *The Journal of Geology*, 105(2), 173–192, doi:10.1086/515908.
- Nousiainen, T., and K. Kandler (2015), Light scattering by atmospheric mineral dust particles, *Light Scattering Reviews* 9, pp. 3–52.
- O’Dowd, C. D., and G. de Leeuw (2007), Marine aerosol production: a review of the current knowledge, *Philosophical Transactions of the Royal Society A: Mathematical, Physical and Engineering Sciences*, 365(1856), 1753–1774, doi:10.1098/rsta.2007.2043.
- O’Hara-Dhand, K., R. L. S. Taylor, I. J. Smalley, D. H. Krinsley, and C. Vita-Finzi (2010), Loess and dust on Earth and Mars: particle generation by impact mechanisms, *Central European Journal of Geosciences*, 2(1), 45–51, doi:10.2478/v10085-010-0001-z.
- Okada, K., J. Heintzenberg, K. Kai, and Y. Qin (2001), Shape of atmospheric mineral particles collected in three Chinese arid-regions, *Geophysical Research Letters*, 28(16), 3123–3126, doi:10.1029/2000GL012798.
- Omar, A. H., D. M. Winker, C. Kittaka, M. A. Vaughan, Z. Liu, Y. Hu, C. R. Trepte, R. R. Rogers, R. A. Ferrare, K. P. Lee, R. E. Kuehn, and C. A. Hostetler (2009), The CALIPSO automated aerosol classification and lidar ratio selection algorithm, *Journal of Atmospheric and Oceanic Technology*, 26(10), 1994–2014, doi:10.1175/2009JTECHA1231.1.
- Orme, A. R. (1992), Late Quaternary Deposits Near Point Sal, South Central California: A Time Frame For Coastal-Dune Emplacement, *Society for Sedimentary Geology Special Publication*, 48, 310–315, doi:10.2110/pec.92.48.0309.
- Osada, K. (2013), Water soluble fraction of Asian dust particles, *Atmospheric Research*, 124, 101–108, doi:10.1016/j.atmosres.2013.01.001.

- Ouren, B. D. S., C. Haas, C. P. Melcher, S. C. Stewart, P. D. Ponds, N. R. Sexton, L. Burris, T. Fancher, and Z. H. Bowen (2007), Environmental effects of off-highway vehicles on bureau of land management lands: a literature synthesis, annotated bibliographies, extensive bibliographies, and internet resources, *Tech. rep.*
- Pérez, C., S. Nickovic, G. Pejanovic, J. M. Baldasano, and E. Özsoy (2006), Interactive dust-radiation modeling: A step to improve weather forecasts, *Journal of Geophysical Research Atmospheres*, *111*(D16), D16,206, doi:10.1029/2005JD006717.
- Piedra, P., and H. Moosmüller (2017), Optical losses of photovoltaic cells due to aerosol deposition: Role of particle refractive index and size, *Solar Energy*, *155*, 637–646, doi:10.1016/j.solener.2017.06.047.
- Piedra, P. G., L. R. Llanza, and H. Moosmüller (2018), Optical losses of photovoltaic modules due to mineral dust deposition: Experimental measurements and theoretical modeling, *Solar Energy*, *164*(February), 160–173, doi:10.1016/j.solener.2018.02.030.
- Price, H. C., K. J. Baustian, J. B. McQuaid, A. Blyth, K. N. Bower, T. Choularton, R. J. Cotton, Z. Cui, P. R. Field, M. Gallagher, R. Hawker, A. Merrington, A. Miltenberger, R. R. Neely, S. T. Parker, P. D. Rosenberg, J. W. Taylor, J. Trembath, J. Vergara-Temprado, T. F. Whale, T. W. Wilson, G. Young, and B. J. Murray (2018), Atmospheric ice-nucleating particles in the dusty tropical Atlantic, *Journal of Geophysical Research: Atmospheres*, *123*(4), 2175–2193, doi:10.1002/2017JD027560.
- Prospero, J. M., P. Ginoux, O. Torres, S. E. Nicholson, and T. E. Gill (2002), Environmental characterization of global sources of atmospheric soil dust identified with the NIMBUS 7 Total Ozone Mapping Spectrometer (TOMS) absorbing aerosol product, *Reviews of Geophysics*, *40*(1), 1–31, doi:10.1029/2000RG000095.
- Pye, K., and C. H. B. Sperling (1983), Experimental investigation of silt formation by static

- breakage processes: the effect of temperature, moisture and salt on quartz dune sand and granitic regolith, *Sedimentology*, *30*(1), 49–62, doi:10.1111/j.1365-3091.1983.tb00649.x.
- Pye, K., and H. Tsoar (2009), *Aeolian sand and sand dunes*, 1st ed., 1–395 pp., Springer, Berlin Heidelberg, doi:10.1007/978-3-540-85910-9.
- Räisänen, P., P. Haapanala, C. E. Chung, M. Kahnert, R. Makkonen, J. Tonttila, and T. Nousiainen (2013), Impact of dust particle non-sphericity on climate simulations, *Quarterly Journal of the Royal Meteorological Society*, *139*(677), 2222–2232, doi:10.1002/qj.2084.
- Ramanathan, V., P. J. Crutzen, J. T. Kiehl, and D. Rosenfeld (2001), Aerosols, climate, and the hydrological cycle, *Science*, *294*(5549), 2119–2124, doi:10.1126/science.1064034.
- Reid, E. A., J. S. Reid, M. M. Meier, M. R. Dunlap, S. S. Cliff, A. Broumas, K. Perry, and H. Maring (2003), Characterization of African dust transported to Puerto Rico by individual particle and size segregated bulk analysis, *Journal of Geophysical Research*, *108*(D19), 8591, doi:10.1029/2002JD002935.
- Rosenberg, P. D., A. R. Dean, P. I. Williams, J. R. Dorsey, A. Minikin, M. A. Pickering, and A. Petzold (2012), Particle sizing calibration with refractive index correction for light scattering optical particle counters and impacts upon PCASP and CDP data collected during the Fennec campaign, *Atmospheric Measurement Techniques*, *5*(5), 1147–1163, doi:10.5194/amt-5-1147-2012.
- Rosenberg, P. D., D. J. Parker, C. L. Ryder, J. H. Marsham, L. Garcia-Carrersa, J. R. Dorsey, I. M. Brooks, A. R. Dean, J. Crosier, J. B. McQuaid, and R. Washington (2014), Quantifying particle size and turbulent scale dependence of dust flux in the Sahara using aircraft measurements, *Journal of Geophysical Research Atmospheres*, *119*(12), 7577–7598, doi:10.1002/2013JD021255.
- Ryder, C. L., E. J. Highwood, P. D. Rosenberg, J. Trembath, J. K. Brooke, M. Bart, A. Dean, J. Crosier, J. Dorsey, H. Brindley, J. Banks, J. H. Marsham, J. B. McQuaid, H. Sodemann,

- and R. Washington (2013), Optical properties of Saharan dust aerosol and contribution from the coarse mode as measured during the Fennec 2011 aircraft campaign, *Atmospheric Chemistry and Physics*, *13*(1), 303–325, doi:10.5194/acp-13-303-2013.
- Ryder, C. L., F. Marengo, J. K. Brooke, V. Estelles, R. Cotton, P. Formenti, J. B. Mcquaid, H. C. Price, D. Liu, P. Ausset, P. D. Rosenberg, J. W. Taylor, T. Choularton, K. Bower, H. Coe, M. Gallagher, J. Crosier, G. Lloyd, E. J. Highwood, and B. J. Murray (2018), Coarse-mode mineral dust size distributions, composition and optical properties from AER-D aircraft measurements over the tropical eastern Atlantic, *Atmospheric Chemistry and Physics*, *18*(23), 17,225–17,257, doi:10.5194/acp-18-17225-2018.
- Ryder, C. L., E. J. Highwood, A. Walser, P. Seibert, A. Philipp, and B. Weinzierl (2019), Coarse and giant particles are ubiquitous in Saharan dust export regions and are radiatively significant over the Sahara, *Atmospheric Chemistry and Physics*, *19*(24), 15,353–15,376, doi:10.5194/acp-19-15353-2019.
- Saito, M., and P. Yang (2021), Advanced bulk optical models linking the backscattering and microphysical properties of mineral dust aerosol, *Geophysical Research Letters*, *Accepted*.
- Saito, M., P. Yang, J. Ding, and X. Liu (2021), A comprehensive database of the optical properties of irregular aerosol particles for radiative transfer simulations, *Journal of the Atmospheric Sciences*, *78*(7), 2089–2111, doi:10.1175/jas-d-20-0338.1.
- Sakai, T., T. Nagai, Y. Zaizen, and Y. Mano (2010), Backscattering linear depolarization ratio measurements of mineral, sea-salt, and ammonium sulfate particles simulated in a laboratory chamber, *Applied Optics*, *49*(23), 4441, doi:10.1364/AO.49.004441.
- Seinfeld, J. H., and S. N. Pandis (2016), *Atmospheric chemistry and physics: from air pollution to climate change*, 3 ed., 1–1152 pp., Wiley.
- Shao, Y. (2008), *Physics and modelling of wind erosion*, 2nd ed., 1–452 pp., Springer, Netherlands, doi:10.1007/978-1-4020-8895-7.4.

- Shao, Y., M. R. Raupach, and P. A. Findlater (1993), Effect of saltation bombardment on the entrainment of dust by wind, *Journal of Geophysical Research: Atmospheres*, *98*(D7), 12,719–12,726, doi:10.1029/93JD00396.
- Shao, Y., M. Ishizuka, M. Mikami, and J. F. Leys (2011a), Parameterization of size-resolved dust emission and validation with measurements, *Journal of Geophysical Research: Atmospheres*, *116*(D8), D08,203, doi:10.1029/2010JD014527.
- Shao, Y., K. H. Wyrwoll, A. Chappell, J. Huang, Z. Lin, G. H. McTainsh, M. Mikami, T. Y. Tanaka, X. Wang, and S. Yoon (2011b), Dust cycle: An emerging core theme in Earth system science, *Aeolian Research*, *2*(4), 181–204, doi:10.1016/j.aeolia.2011.02.001.
- Shao, Y., J. Zhang, M. Ishizuka, M. Mikami, J. Leys, and N. Huang (2020), Dependency of particle size distribution at dust emission on friction velocity and atmospheric boundary-layer stability, *Atmospheric Chemistry and Physics*, *20*(21), 12,939–12,953, doi:10.5194/acp-2020-425.
- Shin, S. K., M. Tesche, K. Kim, M. Kezoudi, B. Tatarov, D. Müller, and Y. Noh (2018), On the spectral depolarisation and lidar ratio of mineral dust provided in the AERONET version 3 inversion product, *Atmospheric Chemistry and Physics*, *18*(17), 12,735–12,746, doi:10.5194/acp-18-12735-2018.
- Sokolik, I. N., and O. B. Toon (1999), Incorporation of mineralogical composition into models of the radiative properties of mineral aerosol from UV to IR wavelengths, *Journal of Geophysical Research Atmospheres*, *104*(D8), 9423–9444, doi:10.1029/1998JD200048.
- Sommariva, M., M. Gateshki, J. A. Gertenbach, J. Bolze, U. König, B. Vasile, and V. A. Surdu (2014), Characterizing nanoparticles with a laboratory diffractometer: From small-angle to total X-ray scattering, *Powder Diffraction*, *29*(2013), S47–S53, doi:10.1017/S0885715614001043.

- Sow, M., S. C. Alfaro, J. L. Rajot, and B. Marticorena (2009), Size resolved dust emission fluxes measured in Niger during 3 dust storms of the AMMA experiment, *Atmospheric Chemistry and Physics*, *9*(12), 3881–3891, doi:10.5194/acp-9-3881-2009.
- Sterk, G., A. F. G. Jacobs, and J. H. Van Boxel (1998), The effect of turbulent flow structures on saltation sand transport in the atmospheric boundary layer, *Earth Surface Processes and Landforms*, *23*(10), 877–887, doi:10.1002/(SICI)1096-9837(199810)23.
- Stull, R. B. (1988), *An introduction to boundary layer meteorology*, 1 ed., 1–666 pp., Springer Netherlands, doi:10.1007/978-94-009-3027-8.
- Sweeney, M. R., V. A. Zlotnik, R. M. Joeckel, and J. E. Stout (2016), Geomorphic and hydrologic controls of dust emissions during drought from Yellow Lake playa, West Texas, USA, *Journal of Arid Environments*, *133*, 37–46, doi:10.1016/j.jaridenv.2016.05.007.
- Swet, N., and I. Katra (2016), Reduction in soil aggregation in response to dust emission processes, *Geomorphology*, *268*, 177–183, doi:10.1016/j.geomorph.2016.06.002.
- Swet, N., T. Elperin, J. F. Kok, R. L. Martin, H. Yizhaq, and I. Katra (2019), Can active sands generate dust particles by wind-induced processes?, *Earth and Planetary Science Letters*, *506*, 371–380, doi:10.1016/j.epsl.2018.11.013.
- Swet, N., J. F. Kok, Y. Huang, H. Yizhaq, and I. Katra (2020), Low dust generation potential from active sand grains by wind abrasion, *Journal of Geophysical Research Earth Surface*, *125*(7), 1–25, doi:10.1029/2020JF005545.
- Tang, M., D. J. Cziczo, and V. H. Grassian (2016), Interactions of Water with Mineral Dust Aerosol: Water Adsorption, Hygroscopicity, Cloud Condensation, and Ice Nucleation, *Chemical Reviews*, *116*(7), 4205–4259, doi:10.1021/acs.chemrev.5b00529.
- Tegen, I., S. P. Harrison, K. Kohfeld, C. I. Prentice, M. Coe, and M. Heimann (2002), Impact of vegetation and preferential source areas on global dust aerosol: Results from

- a model study, *Journal of Geophysical Research: Atmospheres*, 107(D21), AAC 14–1–AAC 14–27, doi:10.1029/2001JD000963.
- Tesche, M., A. Kolgotin, M. Haarig, S. P. Burton, R. A. Ferrare, C. A. Hostetler, and D. Müller (2019), 3+2 + X: What is the most useful depolarization input for retrieving microphysical properties of non-spherical particles from lidar measurements using the spheroid model of Dubovik et al. (2006)?, *Atmospheric Measurement Techniques*, 12(8), 4421–4437, doi:10.5194/amt-12-4421-2019.
- Tiessen, H., H. K. Hauffe, and A. R. Mermut (1991), Deposition of Harmattan dust and its influence on base saturation of soils in northern Ghana, *Geoderma*, 49(3-4), 285–299, doi:10.1016/0016-7061(91)90081-4.
- Ulanowski, Z., J. Bailey, P. W. Lucas, J. H. Hough, and E. Hirst (2007), Alignment of atmospheric mineral dust due to electric field, *Atmospheric Chemistry and Physics*, 7(24), 6161–6173, doi:10.5194/acp-7-6161-2007.
- Usher, C. R., H. Al-Hosney, S. Carlos-Cuellar, and V. H. Grassian (2002), A laboratory study of the heterogeneous uptake and oxidation of sulfur dioxide on mineral dust particles, *Journal of Geophysical Research: Atmospheres*, 107(D23), doi:10.1029/2002JD002051.
- van der Does, M., P. Knippertz, P. Zschenderlein, R. G. Harrison, and J.-B. W. Stuut (2018), The mysterious long-range transport of giant mineral dust particles, *Science Advances*, 4(12), 1–8, doi:10.1126/sciadv.aau2768.
- van der Does, M., G. J. A. Brummer, F. C. van Crimpen, L. F. Korte, N. M. Mahowald, U. Merkel, H. Yu, P. Zuidema, and J. B. W. Stuut (2020), Tropical Rains Controlling Deposition of Saharan Dust Across the North Atlantic Ocean, *Geophysical Research Letters*, 47(5), 1–10, doi:10.1029/2019GL086867.
- Vaughan, M. (2018), Air Board Approves Historic Order for State Parks to Reduce Dust from Oceano Dunes.

- Volten, H., O. Muñoz, E. Rol, J. F. de Haan, W. Vassen, J. W. Hovenier, K. Muinonen, and T. Nousiainen (2001), Scattering matrices of mineral aerosol particles at 441.6 nm and 632.8 nm, *Journal of Geophysical Research*, *106*(D15), 17,375–17,401, doi:10.1029/2001JD900068.
- Volz, F. E. (1972), Infrared Refractive Index of Atmospheric Aerosol Substances, *Applied Optics*, *11*(4), 755–759, doi:10.1364/ao.11.000755.
- Volz, F. E. (1973), Infrared Optical Constants of Ammonium Sulfate, Sahara Dust, Volcanic Pumice, and Flyash, *Applied Optics*, *12*(3), 564–568, doi:10.1364/ao.12.000564.
- Von der Weiden, S.-L., F. Drewnick, and S. Borrmann (2009), Particle Loss Calculator - a new software tool for the assessment of the performance of aerosol inlet systems, *Atmospheric Measurement Techniques*, *2*, 479–494, doi:10.5194/amt-2-479-2009.
- Webb, N. P., C. L. Strong, A. Chappell, S. K. Marx, and G. H. McTainsh (2013), Soil organic carbon enrichment of dust emissions: magnitude, mechanisms and its implications for the carbon cycle, *Earth Surface Processes and Landforms*, *38*(14), 1662–1671, doi:10.1002/esp.3404.
- Westbrook, C. D. (2008), The fall speeds of sub-100 μm ice crystals, *Quarterly Journal of the Royal Meteorological Society*, *134*(634), 1243–1251, doi:10.1002/qj.290.
- Whalley, W. B., B. J. Smith, J. J. McAlister, and A. J. Edwards (1987), Aeolian abrasion of quartz particles and the production of silt-size fragments: preliminary results, *Geological Society, London, Special Publications*, *35*(1), 129–138, doi:10.1144/GSL.SP.1987.035.01.09.
- Wiegner, M., J. Gasteiger, K. Kandler, B. Weinzierl, K. Rasp, M. Esselborn, V. Freudenthaler, B. Heese, C. Toledano, M. Tesche, and D. Althausen (2009), Numerical simulations of optical properties of Saharan dust aerosols with emphasis on lidar appli-

- cations, *Tellus, Series B: Chemical and Physical Meteorology*, *61*(1), 180–194, doi:10.1111/j.1600-0889.2008.00381.x.
- Winker, D. M., W. H. Hunt, and M. J. McGill (2007), Initial performance assessment of CALIOP, *Geophysical Research Letters*, *34*(19), 1–5, doi:10.1029/2007GL030135.
- Woodward, X., A. Kostinski, S. China, C. Mazzoleni, and W. Cantrell (2015), Characterization of dust particles' 3D shape and roughness with nanometer resolution, *Aerosol Science and Technology*, *49*(4), 229–238, doi:10.1080/02786826.2015.1017550.
- Wright, J. (2001), Making loess-sized quartz silt: data from laboratory simulations and implications for sediment transport pathways and the formation of 'desert' loess deposits associated with the Sahara, *Quaternary International*, *76-77*, 7–19, doi:10.1016/S1040-6182(00)00085-9.
- Wright, J., B. Smith, and B. Whalley (1998), Mechanisms of loess-sized quartz silt production and their relative effectiveness: Laboratory simulations, *Geomorphology*, *23*(1), 15–34, doi:10.1016/S0169-555X(97)00084-6.
- Wu, M., X. Liu, H. Yu, H. Wang, Y. Shi, K. Yang, A. Darmenov, C. Wu, Z. Wang, T. Luo, Y. Feng, and Z. Ke (2020), Understanding processes that control dust spatial distributions with global climate models and satellite observations, *Atmospheric Chemistry and Physics*, *20*(22), 13,835–13,855, doi:10.5194/acp-20-13835-2020.
- Yang, W., A. Marshak, A. B. Kostinski, and T. Várnai (2013), Shape-induced gravitational sorting of Saharan dust during transatlantic voyage: Evidence from CALIOP lidar depolarization measurements, *Geophysical Research Letters*, *40*(12), 3281–3286, doi:10.1002/grl.50603.
- Yi, B., C. N. Hsu, P. Yang, and S. C. Tsay (2011), Radiative transfer simulation of dust-like aerosols: Uncertainties from particle shape and refractive index, *Journal of Aerosol Science*, *42*(10), 631–644, doi:10.1016/j.jaerosci.2011.06.008.

- Yizhaq, H., Y. Ashkenazy, and H. Tsoar (2009), Sand dune dynamics and climate change: A modeling approach, *Journal of Geophysical Research: Earth Surface*, *114*(F1), F01,023, doi:10.1029/2008JF001138.
- Yu, H., M. Chin, T. Yuan, H. Bian, L. a. Remer, J. M. Prospero, A. Omar, D. Winker, Y. Yang, Y. Zhang, Z. Zhang, and C. Zhao (2015), The Fertilizing Role of African Dust in the Amazon Rainforest: A First Multiyear Assessment Based on CALIPSO Lidar Observations, *Geophysical Research Letters*, *42*(6), 1984–1991, doi:10.1002/2015GL063040.
- Yu, H., Q. Tan, M. Chin, L. A. Remer, R. A. Kahn, H. Bian, D. Kim, Z. Zhang, T. Yuan, A. H. Omar, D. M. Winker, R. C. Levy, O. Kalashnikova, L. Crepeau, V. Capelle, and A. Chédin (2019), Estimates of African Dust Deposition Along the Trans-Atlantic Transit Using the Decadelong Record of Aerosol Measurements from CALIOP, MODIS, MISR, and IASI, *Journal of Geophysical Research: Atmospheres*, *124*(14), 7975–7996, doi:10.1029/2019JD030574.
- Zender, C. S., H. Bian, and D. Newman (2003), Mineral Dust Entrainment and Deposition (DEAD) model: Description and 1990s dust climatology, *Journal of Geophysical Research*, *108*(D14), 4416, doi:10.1029/2002JD002775.
- Zhang, D. (2008), Effect of sea salt on dust settling to the ocean, *Tellus, Series B: Chemical and Physical Meteorology*, *60*(4), 641–646, doi:10.1111/j.1600-0889.2008.00358.x.